Institut für Chemie – Arbeitsgruppe Peter Saalfrank

Quantum dynamical study of Si(100) surface-mounted, STM-driven switches at the atomic and molecular scale

Dissertation

zur Erlangung des akademischen Grades
"doctor rerum naturalium"
(Dr. rer. nat.)
in der Wissenschaftsdisziplin Theoretische Chemie

eingereicht an der
Mathematisch-Naturwissenschaftlichen Fakultät
der Universität Potsdam

von
Karl Zenichowski
aus Meiningen

Potsdam, im Mai 2012

Published online at the
Institutional Repository of the University of Potsdam:
URL http://opus.kobv.de/ubp/volltexte/2012/6215/
URN urn:nbn:de:kobv:517-opus-62156
http://nbn-resolving.de/urn:nbn:de:kobv:517-opus-62156

"[...] ja (an unseren Hochschulen) [...] statt des Erstaunens vielmehr das Gegenteil gelehrt wird: das Zählen und Messen statt des Entzückens, die Nüchternheit statt der Bezauberung, das starre Festhalten am losgetrennten Einzelnen, statt das Angezogensein vom Ganzen und Einen. Diese Hochschulen sind ja nicht Schulen der Weisheit, sie sind Schulen des Wissens aber stillschweigend setzen sie das von ihnen nicht Lehrbare, das Erleben Können, das Ergriffensein Können, das Goethesche Erstaunen eben doch voraus. [...]"

Hermann Hesse: Mit dem Erstaunen fängt es an.

Suhrkamp Verlag, Frankfurt am Main (2000).

1. Gutachter:	Herr Prof. Dr. P. Saalfrank, Universität Potsdam
2. Gutachter:	Frau Prof. Dr. K. Franke, Freie Universität Berlin
3. Gutachter:	Herr Prof. Dr. P. Kratzer, Universität Duisburg-Essen

Publications

"Exciting flavins: Absorption spectra and spin–orbit coupling in light–oxygen–voltage (LOV) domains"
Karl Zenichowski, Marcel Gothe, Peter Saalfrank
J. Photochem. Photobiol. Chem. **190**, 290 (2007).

"Open–system density matrix description of an STM–driven atomic switch: H on Si(100)"
Karl Zenichowski, Tillmann Klamroth, Peter Saalfrank
Appl. Phys. A **93**, 319 (2008).

"Current–induced versus temperature–induced switching of single cyclo–octadiene molecules chemisorbed on a Si(001) surface"
Christophe Nacci, Stefan Fölsch, Karl Zenichowski, Jadranka Dokič, Tillmann Klamroth, Peter Saalfrank
Nano Lett. **9**, 2996 (2009).

"Characterization of Rhodamine 6G Release in Electrospray Ionization by Means of Spatially Resolved Fluorescence Spectroscopy"
Daniel Riebe, Martin Zühlke, Karl Zenichowski, Toralf Beitz, Carsten Dosche, Hans-Gerd Löhmannsröben
Z. Phys. Chem. **225**, 1055 (2011).

"Current versus temperature-induced switching of a single molecule: Open-system density matrix theory for 1,5-cyclooctadiene on Si(100)"
Karl Zenichowski, Jadranka Dokič, Tillmann Klamroth, Peter Saalfrank
J. Chem. Phys. **136**, 094705 (2012).

"STM-switching of organic molecules on semiconductor surfaces: an above threshold density matrix model for 1,5 cyclooctadiene on Si(100)"
Karl Zenichowski, Christophe Nacci, Stefan Fölsch, Jadranka Dokič, Tillmann Klamroth, Peter Saalfrank
J. Phys.: Condens. Matter **24** (2012) (accepted).

Contents

Abbreviations

AFM	atomic force microscope
CASSCF	complete active space self-consistent field (method)
COD	1,5 cyclooctadiene
DFT	density functional theory
DIET	desorption induced by electronic transitions
DIMET	desorption induced by multiple electronic transitions
EA	electron affinity
EOM	equations of motion
FGH	Fourier grid Hamiltonian
FGR	Fermi's golden rule
FTIR	Fourier-transform infrared spectroscopy
FWHM	full with at half maximum
HOMO	highest occupied molecular orbital
IET	inelastic electron tunneling
IETS	inelastic electron tunneling spectroscopy
LDOS	local density of states
LUMO	lowest unoccupied molecular orbital
MCSCF	multi-configuration self-consistent field (method)
MCTDH	multi-configuration time-dependent Hartree (method)
MCWP	Monte-Carlo wave packet (method)
SE	Schrödinger equation
STM	scanning tunneling microscope
TD-SCF	time-dependent self-consistent field (method)
TDH	time-dependent Hartree (method)
TDSE	time-dependent Schrödinger equation
U	STM bias voltage
UHV	ultra-high vacuum
VIP	vertical ionization potential
XPS	X-ray photoelectron spectroscopy
1D/ 2D	one-/ two-dimensional
1S/ 2S	one-/ two-surfaces
1S1D	one-dimensional one surface model
1S2D	two-dimensional one surface model
2S1D	one-dimensional two surfaces model
2S2D	two-dimensional two surfaces model

Chapter 1

Introduction

Addressable, surface mounted structures of molecular or even atomic scale are on their way in today's silicon-based information technology. The development is driven by the demand for smaller, cheaper and faster electronic devices in order to improve storage density and data processing speed [5]. The ultimate goal is to gain a fast, but stable and reversible switching device, formed by a single molecule or atom, which allows for the definite control over and distinction between, its switching status. The successful implementation in a memory device would be a major step towards the famous vision of Richard Feynman when he said in 1960 [6]:

> All of the information that man has carefully accumulated in all the books in the world, can be written [...] in a cube of material one two-hundredth of an inch wide.

Powerful techniques such as the scanning tunneling microscope (STM) and the atomic force microscope (AFM) have already opened the possibility for the examination and manipulation of two-dimensional atomic surface structures [7, 8]. While every experiment starts with the full range of complexity in terms of environmental influences and finds its challenge in reducing the complexity systematically, theory works in the opposite direction. Based on rather simple models, theory finds its challenge in systematically increasing complexity and including the environment. Thus fruitful interaction can be expected if both sides are able to meet at a similar level of complexity. Therefore, STM experiments of atomic or molecular scale and quantum theoretical investigations are naturally compatible and mutually demanding partners.

This thesis was prepared in the framework of the "Sonderforschungsbereich 658: Elementarprozesse in molekularen Schaltern an Oberflächen" (Collaborative research center 658: Elementary processes in molecular switches at surfaces). This thesis intends to make a contribution to the understanding of experimentally observed, STM-induced switching of adsorbates on a silicon(100) surface. The first part of the thesis covers the reversible, bistable lateral movement of single hydrogen atoms on Si(100) surface-dimers, while the second part studies the biconformational switching of cyclooctadiene, chemisorbed on

Si(100). For both systems experimental data are available, describing their STM-induced switching [9, 10].

1.1 The scanning tunneling microscope (STM)

In the last 25 years since the invention of the ultra-high vacuum (UHV) scanning tunneling microscope by Binning, Rohrer et al. [7], a large number of surface science STM experiments have been published. In order to understand the benefit of the STM technology in surface science, a brief summary is given about STM setup and functionality.

STM setup: The principle setup of the STM is made of an ultra sharp conducting tip, situated above a conducting surface sample [11]. If the intermediate vacuum gap is below 1 nm, the overlap of tip and sample wavefunctions allows for a net electron tunnel current I through the gap, driven by an applied bias voltage U. Electrons tunnel from occupied tip electronic states into unoccupied surface states at a sufficiently high positive STM sample bias. Vice versa, the electrons tunnel from the surface to the tip at a sufficiently negative sample bias. The tunnel current reflects the local density of states (LDOS) of occupied or unoccupied electronic surface levels, which decays exponentially towards the vacuum side.

The tip is movable along x-, y- and z-directions with an accuracy below 1 Å, by means of voltage sensitive piezoelectric transducers. Surface sample, tip and piezos are placed in an UHV chamber at pressures below 1.0×10^{-9} torr. The STM also may operate at low temperatures down to 4 K, to reduce thermal noise and the risk of impurities, or at variable temperatures up to several hundred Kelvin. The tip, typically made from a metal or metal alloy, can exhibit atomic protrusions at its outermost extremity. If the tunneling current is flowing through such a single 'apex' atom, its magnitude, in the order of nano-Ampere, is used to probe the surface LDOS with atomic resolution.

STM working modes: The tunneling current can be recorded as a function of the tip position or the bias voltage, which results in two principal kinds of measurements. In the so-called *constant-current mode* one uses the fact that the STM tunneling current decays exponentially for an increasing vacuum gap. Here, a feedback loop ensures a constant current, while the tip scanns parallel to the surface. The recorded changes in the tip height reveal surfaces of a constant LDOS [12]. Applications, based on the capability to perform high-resolution current measurements, are for example in the visualization of surface topologies [13, 14] and standing electronic waves, for instance in the case of so-called 'quantum corrals' [15, 16], conductivity measurements of organic ad-molecules [17] and charge transport experiments [18, 19].

In the *constant-height mode* the current-voltage relation is recorded at fixed tip height. The resulting I/U-spectra and the differential conductance of first (dI/dU) and second order

(d^2I/dU^2) give information about the LDOS and energetic positions of inelastic tunneling channels. Those appear as steps in the dI/dU curves at a certain bias voltage and indicate adsorbate vibrations, excited by the tunneling electrons. The effect is used to determine vibrational spectra of single, adsorbed atoms or molecules. The relevant experiment is called STM-IETS, where IETS stands for inelastic electron tunneling spectroscopy [20, 21, 22, 23].

IET - Inelastic electron tunneling: The STM current tunneling through an adsorbate-surface system can flow either elastically or inelastically and usually the elastic tunneling current dominates over the inelastic fraction by a few orders of magnitude. The maximum energy of tunneling electrons is set by the bias voltage, while the excitation rate is tunable via the tunnel current. There are two main contributions to the inelastic tunneling current, namely dipole and resonance scattering [24]. For the first, the electric field of tunneling electrons couples to transition dipole moments of adsorbate vibrations [25]. For the latter, incident electrons/holes are captured in empty/occupied adsorbate electronic states. Transient, charged adsorbate species are formed and induce nuclear motions, due to an altered potential surface of the resonance state, as compared to the ground state potential [26].

The influence of electronically excited states on the nuclear dynamics of surface-adsorbate systems was studied intensively for both, photo- and STM-induced processes (see e.g., review [27] and references therein). Fundamental theoretical concepts were developed which allow for a classification of the studied phenomena. Looking at the current dependence, for example of the STM-induced desorption yield Y, it is found, that Y scales either linearly ($Y \propto I$) or according to a power law ($Y \propto I^N, N > 1$) with tunnel current I [28]. A similar behavior is seen for laser-induced desorption from surfaces, where Y scales linearly or by a power law with the laser fluence F. These scenarios are referred to as *desorption-induced by electronic transitions* (DIET) or desorption-induced by *multiple* electronic transitions (DIMET) [27], for linear and superlinear dependencies, respectively. For STM-induced DIET, the single tunneling electron/hole provides enough energy to the adsorbate in order to overcome the desorption barrier. In the case of STM-induced DIMET, the electron/hole energy is below the threshold energy, allowing only for a gradual heating of the system via 'vibrational ladder climbing', driven by multiple excitations. Therefore, the DIMET yield is much more sensitive to the adsorbate vibrational lifetime [29], i.e., the relaxation time due to vibration-phonon or vibration-electron coupling. An example here is the IET (inelastic electron tunneling)-induced 'hopping' of Xe atoms between tip and sample [30]. Another example, now at a semiconductor surface, is the STM-induced desorption of single H/D atoms from a H/D passivated Si(100) surface. A negative ion resonance of σ^* character located at the Si-H bond was identified to be responsible for both DIET and DIMET phenomena, observed for bias voltages above [29] and below [31] a threshold of 7 V. One therefore also often speaks about an 'above-threshold' and 'below-threshold' regime, regarding the energy position of the resonance state concerned. However, it is cer-

tainly possible to obtain single-electron-induced processes in the 'below-threshold regime' as shown by several STM-experiments [28, 32]. The important point here is whether the incident electron or hole, first of all, provides enough energy to overcome a certain reaction barrier and secondly, whether it 'finds' a resonance state it may occupy.

Aside from desorption processes, all other kinds of IET-induced processes at surfaces can be classified with respect to their current dependence. The theoretical description of IET-driven adsorbate dynamics is given in more detail in another part of the introduction (Sec. 1.3), whereas the techniques employed are laid out in the theory chapter (Sec. 2.5.3).

Further tip-sample interactions: Besides the inelastic electron tunneling other interactions also exist which allow for the manipulation of an adsorbate. Forces of attraction and repulsion acting via the tip on the sample are caused by chemi- or physisorptive interactions like van der Waals forces or by the electric field between tip and sample. The latter may couple to the static dipole moment of the adsorbate. Also magnetic forces exist as a possible way of interacting with the adsorbate spin. All these additional mechanisms and IET allow for a more or less controlled manipulation of spatial, electric and magnetic properties of adsorbate surface systems on the nanometer scale [33, 34]. Some further examples are the controlled movement of atoms and molecules on the surface [35, 36, 37, 38, 39], single atom spin flip experiments via high-magnetic field STM [40] and STM-triggered chemical reactions [41, 42, 43].

For instance, the reversible repositioning of single C_{60} molecules on Cu [44], switching between four molecular conformations of chlorophyll on Au [45], bistable switching of hydroxyl groups on Cu [46], biphenyl on Si(100) [47] and Co atoms on Cu [48] were experimentally achieved. Further work concerned with the bistable rotation of an Si ad-dimer on Si(100) [49] and cis/trans-isomerization of azobenzene on Au and Cu [50] can be found. This list is not intended to be complete, but rather to acknowledge the general interest in STM-induced switching.

Challenge and outlook: The concepts for high-density, miniaturized memory and/or switching devices relying on the STM are under intense research. Further applications are for example in the field of nanolithography [51] and in the development of molecular mechanical or electronic devices [52, 53, 54]. But such STM-based attempts for switchable nanodevices are also facing a number of technical problems. Here, the speed of reading and writing processes, the signal-to-noise ratio, the accuracy of tip positioning and instabilities of the tip have to be mentioned [55]. Much effort is being spent to increase the speed and stability of the STM in order to make it useful for nanotechnological applications [56, 57].

For the moment, STM is a beautiful tool in the arena of fundamental research, suitable for finding promising systems and for understanding the switching mechanism. Up to now, the insights obtained still have to be transferred into different devices, suiting the needs of mass production, speed and scale. As possible alternatives, the AFM technique [58, 59] or opto-electronical devices [60] are under focus, for example.

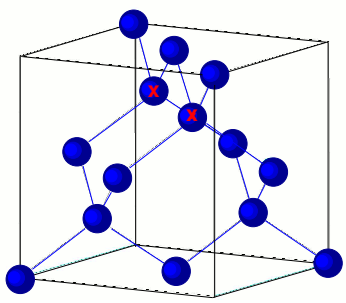

Figure 1.1: Cubic unit cell of crystalline silicon. Red crosses mark one possible Si-dimer formed under the (2×1) surface reconstruction, formed after the removal of the top layer.

1.2 The Si(100)-(2×1) surface

The silicon surface has the advantages of being able to chemisorb various adsorbates, to have a semiconductor band structure and to be widely utilized in commercially available microelectronics. A number of experiments regarding the STM functionalization of adsorbate silicon surface systems have already been mentioned.

Silicon belongs to the 4th main group of the periodic table of elements and crystallizes in a diamond lattice, where each Si-atom is bonded to a tetrahedral sphere of four Si-atom neighbors. A schematic picture of the resulting crystal structure and the cubic unit cell are shown in Fig. 1.1. Cutting the crystal along one of the cube planes, results in two single 'dangling-bond' electrons at each surface atom (see exemplary atom positions, marked with a red cross in Fig. 1.1). The Si-atoms at the surface carry two unbound 'dangling-bond' electrons, since they have two bonding partners less than Si-atoms in bulk. The resulting, unreconstructed (1×1) surface is energetically unfavorable. Therefore, the surface undergoes a (2×1) reconstruction, establishing rows of silicon surface-dimers. Each surface-dimer carries four dangling-bond electrons. A strong σ bond is established in each silicon-dimer, using two out of four dangling-bond electrons. Additionally, the silicon-dimer atoms are linked via a weak π bond of dangling-bond electrons [61]. The (2×1) reconstruction accounts for special surface properties, like its high reactivity towards adsorbate molecules and atoms. The high reactivity is due to the existence of those weak π bonds, since the formation of alternative bonds with an adsorbate molecule can be energetically favorable relative to the π bond [62]. The surface-dimers of the naked, reconstructed surface are also found to be buckled by $\approx 18°$ [63, 64], relative to the surface plane, below 200 K. Here, two neighboring Si-dimers, within a dimer row, are found to be buckled relative to each other [65] in a $c(4 \times 2)$ reconstruction. At room temperature, however, a symmetric appearance is observed in the STM, because of a thermally activated flip-flopping motion of the silicon-dimers [66]. The buckling is caused by a zwitterionic electronic configuration of the silicon-dimer, where the 'upper' silicon atom (S_u) carries both dangling-bond electrons. In fact, S_u is found to be electron-richer than its lower partner (S_d). A nucleophilic character in terms of chemical reactivity evolves at S_u and its electrophilic counterpart at S_d [67]. The occupied and unoccupied dangling-bond states of up and down buckled Si-atoms form electronic surface bands for the $c(4 \times 2)$ reconstruction [68]. The experimental range for the occupied dangling-bond state for Si(100) is

found between $-0.4\,\mathrm{eV}$ and $-0.8\,\mathrm{eV}$ [69].

Silicon is a semiconductor. The band gap between occupied valence and empty conduction bands depends on the surface reconstruction. It is found for example to be $1.12\,\mathrm{eV}$ at the Γ point of (2×1) reconstructed Si(100). Electron transport is possible via electron 'holes' in the valence band and/or electrons in the conduction band, which can be induced via electronic excitation or charge carrier injection by an STM. Insertion of additional 'holes' (electron vacancies) or surplus electrons via p- or n-doping increases the conductance by shifting the Fermi level towards the valence or conduction band, respectively [69].

1.3 Theory of STM-induced switching dynamics

Theoretical studies of IET-induced vibrational heating of adsorbates and vibrational relaxation on Si-surfaces have been performed in recent decades. As already mentioned, IET can occur in the 'above-threshold' and 'below-threshold' limits. The following examples are presented for theoretical concepts for the study of IET-induced nuclear adsorbate dynamics, including vibrational relaxation.

IET in the 'below-threshold limit': Here, the influence of resonance scattering events is treated via vibrational transition rates in the ground state. Therefore, no explicit treatment of the dynamics on the resonance potential energy surface is needed. Walkup et al. [70] studied IET-induced vibrational heating, solving a set of rate equations (Pauli master equations) for a *truncated harmonic oscillator model*. All population transfer rates scale linearly with the state number i and harmonic selection rules ($\Delta i = \pm 1$) are applied. Perturbation theory-based rate expressions cover inelastic dipole and resonance scattering [25, 26], vibrational relaxation and a finite surface temperature. Up- and downward rates drive the system towards a Boltzmann-like steady state, described by a 'characteristic temperature'. All rates are obtained via experimentally-established estimates [70] or via calculations of coupling matrix elements for a set of vibrational eigenstates [71], as in the case of Xe atoms transferred between STM tip and surface [30]. Here, the double-well potential is treated approximately as a set of two harmonic oscillators. Tunneling between both wells is approximated via rates. Another example for an application of the truncated harmonic oscillator model was published by Gao et al. [72], also focusing on the Xe atom transfer problem.

The present thesis utilizes and extends the model of Walkup et al. for the 'below-threshold regime', as will be discussed in theory Sec. 2.5.3.

IET in the 'above-threshold limit': The mentioned single-electron-induced desorption of H/D from Si(100) [29] was theoretically investigated by Boendgen et al. [73], using 'Gadzuk's jump and weighted average' scheme [74, 75] (see Sec. 2.6.2). The effects of finite surface temperature and a coordinate dependent electronic lifetime can be described, via

further extensions to the Gadzuk method [73]. Additionally, the results were compared to classical dynamics and results of open-system density matrix theory. Studying the same system, semi-classical propagation of a Gaussian wave packet on the resonance state potential was utilized by Avouris et al. [76, 77]. Here, complex potentials account for the electronic quenching process.

Finally, an example using *open-system density matrix theory* [78] in the context of resonant IET is mentioned. The hole-resonance driven lateral hydrogen-atom transfer on Si(100)-(2×1) surface-dimers was studied by Abe et al. [79]. Within open-system density matrix theory, a set of approximations[1] allows for a propagation of the system modes only, while treating the interaction with a bath of phonons or electronic states only approximately via perturbative population transfer rates. The system Hamiltonian, considered by Abe et al. consists of one switching mode on two potential energy surfaces. Dissipative operators of Lindblad type [80] were used to treat vibrational and electronic relaxation.

Vibrational adsorbate relaxation on Si(100): For adsorbates on silicon surfaces, coupling to the surface plays a crucial role in the switching process, since the adsorbate vibrations interact with the surface phonon-bath. The inelastic interactions with the surface are responsible for the transfer of vibrational energy from or to the surface. Furthermore the inelastic and elastic interactions destroy any initially existing or, for example, photo-induced phase information between the adsorbate vibrational levels via so-called 'dephasing'.

The vibration-phonon coupling is the dominating dissipative energy transfer mechanism for adsorbate vibrations on semiconductor surfaces, as long as the semiconductor band gap energy is larger than the vibrational energy quanta [81]. A strong coupling causes a fast system-bath equilibration. The higher the spectral density, i.e. the product of bath phonon-density and coupling strength, is in that particular energy region the easier a vibrational quantum of the system can be transferred to or from the bath. Here it is important to know the Debye frequency of the surface, i.e. the upper limit of the phonon energy band. The Debye frequency for silicon is between 500 to $580\,\mathrm{cm}^{-1}$ [82, 83, 84]. Therefore, vibrational quanta of a system within that range can perfectly couple to the bulk phonon-density, allowing for a 'rapid' decay on the order of picoseconds, which is the lower limit for vibrational lifetimes of adsorbates on silicon surfaces.

Taking the H-Si stretching and the H-Si-Si bending modes of H on Si(100)(2×1) as an example, two different strategies used to calculate the vibrational lifetimes are briefly mentioned in the following. Both modes are characterized by frequencies around $680\,\mathrm{cm}^{-1}$, and $2100\,\mathrm{cm}^{-1}$, respectively [85].

In the first approach discussed here, lifetimes were calculated by Andrianov et al. by means of *perturbation theory* [83]. The system-bath coupling strength and the phonon-density of states were calculated explicitly, performing normal mode analysis on hydrogen

[1] For a detailed explanation, please refer to Sec. 2.4.

saturated silicon clusters containing up to 320 silicon atoms. The potential energy function was modeled via a force field, whereas the two system modes, namely the H-Si stretching and bending modes, were described by an analytical model potential. Andrianov et al. calculated lifetimes in the order of 1 ps for the first excited state of the bending mode. The lifetime of the first excited state of the stretching mode was calculated as 1.53 ns at 300 K, which accords well to the experimental value of 1.2 ns [83]. Furthermore, a nearly linear scaling was found up to the 10th excited bending mode and to a somewhat lesser extent, also up to the 4th stretching mode. The frequency of the stretching mode ($\approx 2100\,\mathrm{cm}^{-1}$), lies outside the Si-bulk phonon-band and only allows for a decay via less likely multi-phonon processes. It was found that inter-mode coupling is the dominating relaxation pathway for this high-frequency adsorbate mode. Accordingly, a stretching vibrational quantum is transformed into two bending 'phonons' of lower frequency. The resulting excitation of the bending mode, subsequently decays into the silicon bulk via two-phonon processes. An ns lifetime of a high-frequency adsorbate mode on Si(100) was further established experimentally and theoretically for the CO@Si(100) stretching mode ($\omega \approx 2000\,\mathrm{cm}^{-1}$) [86, 81].

A second possible approach is the non-perturbative treatment via a high dimensional wave packet propagation, including system and bath degrees of freedom, and a system-bath coupling operator. Here, lifetimes are obtained by following the population evolution of a vibrationally excited state. For example, the *multi-configurational time-dependent Hartree* (MCTDH) method [87] allows for an explicit inclusion of H-Si bending and stretching modes as well as 50 bath oscillators of the silicon bulk into the Hamiltonian [88]. The perturbatively calculated ps lifetimes for the H-Si bending modes were confirmed by MCTDH.

Additionally, the *time-dependent self consistent field* (TD-SCF) method or *time-dependent Hartree* (TDH) method is mentioned [89]. Here a single Hartree product of one dimensional wavefunctions is used to represent multidimensional problems. The coupling between individual modes is treated via mean-field potential, representing the interaction with all other modes. TD-SCF allows for the inclusion of several hundreds of bath modes coupled to a few system modes. Actually, the TD-SCF calculated lifetimes for H-Si stretching and bending modes compare well with results obtained via perturbation theory [90]. The TD-SCF method fails, however, if interactions between specific states determine the dynamics and if correlated states are important. A solution to the problem is the flexibilization of the wave function by allowing for a sum of Hartree products as in MCTDH.

In this thesis, 'below-threshold' IET-induced switching of adsorbates and vibrational adsorbate relaxation via surface phonon coupling is treated in the framework of open-system density matrix theory. The propagation is performed using a set of localized vibrational states in the electronic ground state. All population transfer rates are derived via perturbation theory. In the 'above-threshold' regime a second electronic state is included in the propagation. The applied theory framework is explained in the following chapter.

Chapter 2

Theory

This chapter gives an overview about the theoretical concepts being utilized. Starting with the time-independent Schrödinger equation (SE), the Fourier Grid Hamiltonian (FGH) method is introduced. This method is used to solve the SE for a set of bound states in a double minimum (double-well) potential surface. A localization scheme is used to arrive at vibrational wave functions, which are localized to a single potential well. Subsequently, the time-dependent nuclear switching dynamics are simulated, in the localized basis, by means of the Lindblad dynamical semi-group approach [80]. The theory allows for energy transfer between system and bath degrees of freedom by means of population transfer rates. The rates are based on first order perturbation theory [91]. The presented rate expressions cover vibrational relaxation and excitation via coupling to the surface phonon-bath and due to interactions with inelastic tunneling electrons. At the end of the theory chapter density functional theory (DFT) and Koopmans' theorem are mentioned briefly, which are applied in order to approximate potential surfaces of ion resonance states.

2.1 Time-independent Schrödinger equation

The time-independent Schrödinger equation (SE), for a system with mass m moving along coordinates $q_1, \ldots, q_N$ is given as,

$$\hat{H}\psi_n = E_n\psi_n = (\hat{T} + V)\psi_n = \left(\frac{\hat{p}^2}{2m} + V(\underline{q})\right)\psi_n = \left(-\frac{\hbar^2}{2m}\Delta + V(\underline{q})\right)\psi_n. \tag{2.1}$$

The obtained eigenenergies E_n and eigenfunctions ψ_n further depend on the boundary conditions. The kinetic energy operator $\hat{T}$ is expressed via the momentum operator $\underline{\hat{p}} = -i\hbar\underline{\nabla}$, where $\underline{\nabla} = \frac{\partial}{\partial q_1}\cdot\underline{e}_1 + \cdots + \frac{\partial}{\partial q_N}\cdot\underline{e}_N$ is the Nabla operator and $\Delta = \underline{\nabla}^2$. $V(\underline{q})$ is the potential energy function, depending on N coordinates q_i with $\underline{q} = (q_1\cdot\underline{e}_1, \ldots, q_N\cdot\underline{e}_N)$ and unit vectors $\underline{e}_i$. The eigenfunctions or wavefunctions ψ_n, depend also on all coordinates. The statistical average of any measurable system quantity is defined via the expectation value $\langle\hat{A}\rangle$ of an operator $\hat{A}$, $\langle\hat{A}\rangle = \langle\psi|\hat{A}|\psi\rangle$.

2.2 Fourier Grid Hamiltonian Method (FGH)

The nuclear switching dynamics are simulated in the basis of vibrational eigenstates. Taking, for example, a one-dimensional potential $V(q)$ along coordinate q, the Fourier Grid Hamiltonian method is briefly introduced as a convenient way of solving the time-independent Schrödinger equation for bound states $\psi_n(q)$, represented on a spatial grid [92, 93]. For this purpose, a set of N spatial basis functions $\varphi_i(q)$, $(i = 1, \ldots, N)$ is introduced, namely Dirac delta functions [92], with

$$\varphi_i(q) = \delta(q - q_i) \qquad , \tag{2.2}$$

where the N grid points q_i are distributed equidistantly across the grid extension $L = (N-1) \cdot \Delta q$,

$$q_{i+1} = q_i + \Delta q \qquad . \tag{2.3}$$

Their orthogonality is proven by $\langle \varphi_i | \varphi_j \rangle = \int \delta(q - q_i)\delta(q - q_j)dq = \delta(q_j - q_i) = \delta_{ji}$, since $\int f(q) \cdot \delta(q - q_i)dq = f(q_i)$ is one feature of the Dirac delta function. The expansion of $\psi_n(q)$ as linear combinations of basis functions φ_i is simply achieved via the completeness condition,

$$|\psi_n\rangle = \hat{1}\,|\psi_n\rangle = \sum_i |\varphi_i\rangle\langle\varphi_i|\psi_n\rangle = \sum_i c_{i,n}|\varphi_i\rangle \qquad . \tag{2.4}$$

The representation of $\hat{H}$ in the basis of φ_i, with implicit periodic boundary conditions, results in a Hamilton matrix $\underline{\underline{H}}$ with individual elements $H_{ij} = \langle \varphi_i | \hat{H} | \varphi_j \rangle$. The potential energy function V is diagonal in the spatial grid basis,

$$V_{ij} = \langle \varphi_i | V | \varphi_j \rangle = V(q_j)\delta_{ij} \qquad . \tag{2.5}$$

The kinetic energy operator $\hat{T}$ only becomes diagonal in the corresponding momentum space, when expanded in the corresponding basis $\tilde{\varphi}_k(p)$ with $(k = 1, \ldots, N)$,

$$T_{kl} = \langle \tilde{\varphi}_k | \hat{T} | \tilde{\varphi}_l \rangle = \frac{p_l^2}{2m}\delta_{kl} \qquad . \tag{2.6}$$

To allow for a definition of T_{kl} in the spatial grid basis, a discrete Fourier transform is used to switch between spatial and momentum representation, as defined in Ref. [92]. One finally gains matrix elements for the kinetic energy operator $\hat{T}$, expressed in the spatial grid basis $T_{ij} = \langle \varphi_i | \hat{T} | \varphi_j \rangle$,

$$T_{ii} = \frac{\hbar^2\pi^2}{\mu L^2}\frac{N^2+2}{6} \qquad \text{and} \qquad T_{ij,i\neq j} = (-1)^{i-j}\frac{\pi^2\hbar^2}{\mu L^2}\frac{1}{sin^2[(i-j)\pi/N]} \qquad , \tag{2.7}$$

Furthermore, the accessible range of momentum and kinetic energy, represented by eigenfunction ψ_n, depends on the spatial grid extension L and grid spacing Δq. The maximal expressible momentum p_{max} is given by,

$$p_{max} = \frac{\pi\hbar}{\Delta q} \qquad . \tag{2.8}$$

Finally, the obtained Hamilton matrix $\underline{\underline{H}}$, including elements $H_{ij} = T_{ij} + V(q_i)\delta_{ij}$, has to be diagonalized in order to satisfy the resulting secular equations,

$$\sum_k [H_{ik} - E_n \delta_{ik}] c_{k,n} = 0 \tag{2.9}$$

and to obtain the vibrational eigenfunctions ψ_n and corresponding eigenenergies E_n.

2.3 Vibrational state localization

All examples of STM-induced conformational switching studied here, take place on symmetric double-well shaped potential energy surfaces. Each well represents an individual conformational state of the switch, separated by a barrier. The switching is considered as a transfer of population initially entirely localized to the left (L) or right (R) potential well to the opposite potential well. The vibrational state doublets for 1 D potential surfaces are obtained via the FGH method, using a symmetry-adapted grid basis (see Appendix A). The resulting eigenstates show equal distribution probabilities on both potential wells. Initial localization of the wave packet to the right or left potential well is achieved via a proper linear combination of two unlocalized, symmetry related states.

The one-dimensional (1 D) double-well potentials, of all examples studied in the following, show C_s symmetry and give rise to delocalized states which transform like A and A'. Here, A and A' refer to the corresponding irreducible representations. They are equivalently referred to as states of *odd* (-) and *even* (+) parity, transforming like $\psi_n^+(q) = \psi_n^+(-q)$ and $\psi_n^-(q) = -\psi_n^-(-q)$, respectively. Localized states ($\tilde{\psi}_n^{L,R}$) are simply obtained via linear combinations of corresponding odd and even eigenstates of doublet n,

$$\tilde{\psi}_n^{L,R}(q) = \frac{1}{\sqrt{2}} \left(\psi_n^+(q) \pm \psi_n^-(q) \right) \quad . \tag{2.10}$$

The corresponding localized state energies ($E_n^{L,R}$) are therefore defined via,

$$E_n^L = E_n^R = \frac{1}{2} \left(E_n^- + E_n^+ \right) \quad . \tag{2.11}$$

Degree of localization, Q_n:

The degree of localization Q_n^L of the 'left' ($q < 0$) localized state $\tilde{\psi}_n^L$ is defined via the integral over its spatial distribution probability between the potential center ($q = 0$) , i.e., the center of the switching barrier and the 'left' grid border, along the switching coordinate q,

$$Q_n^L = Q_n^R = \int_{-\infty}^{0} [\tilde{\psi}_n^L(q)]^* \tilde{\psi}_n^L(q) dq \quad . \tag{2.12}$$

The 'right' ($q > 0$) localized state $\tilde{\psi}_n^R$, shows the same degree of localization to the 'right' as the 'left' localized state to the 'left', since they originate from the same doublet n.

2.4 Open-system density matrix theory

The nuclear switching dynamics of adsorbates at silicon surfaces, as the central topic of the actual work, is simulated in the basis of vibrational eigenstates and their localized linear combinations. Further *open-system density matrix theory* [27, 94, 78] is used as the theoretical framework for all simulations. The corresponding equations of motion (EOM) have the advantage of allowing for the separation of a high dimensional, not accurately tractable problem, with many degrees of freedom, into a low dimensional, exactly tractable 'system' part and an approximately treated environment, called the 'bath'. Energy exchange between system and bath is driven by inelastic interactions between both entities, accompanied by changes of individual state populations in the system and the bath. The process of energy flow from the system into the bath is also called a 'dissipative process' or simply dissipation. Elastic interactions with the bath, on the other hand, do not alter the system energy but are responsible for a loss of information about phase relations between individual states. Such processes are subsumed as 'pure dephasing' and are neglected in the following. The coupling to an external perturbation such as a time-dependent electric field (e.g. laser pulse) is easily possible via the system Hamiltonian, as will be shown later. The open-system density matrix theory in its various forms is especially suited for dealing with nuclear dynamics in adsorbate-surface systems, as seen from a large number of corresponding publications [27]. Examples such as the infrared-laser excitation of NH_3 vibrations on Cu(111) [95], the surface scattering of noble gas atoms [96], and DIET of vibrationally hot adsorbates [97] are mentioned here. Now, a short outline of open-system density matrix theory is given.

2.4.1 The density operator $\hat{\rho}$

Starting to look at the entire problem, consisting of system and bath, the density matrix operator is defined as a sum over projector type products of system and bath states Ψ_j and their populations p_j,

$$\hat{\rho} = \sum_j p_j |\Psi_j\rangle\langle\Psi_j| \qquad , \tag{2.13}$$

where all p_j are real numbers between 0 and 1. Ψ_j and thus $\hat{\rho}$ can be represented in a complete basis of orthonormal ψ_m,

$$|\Psi_j\rangle = \sum_m c_{j,m}|\psi_m\rangle \qquad \text{and} \qquad \rho_{mn} = \langle\psi_m|\hat{\rho}|\psi_n\rangle = \sum_j p_j c_{j,m} c^*_{j,n} \qquad . \tag{2.14}$$

After normalization of the trace $\mathrm{Tr}\{\underline{\underline{\rho}}\}$, using a complete basis $\sum_n |\psi_n\rangle\langle\psi_n| = \hat{1}$,

$$\mathrm{Tr}\{\underline{\underline{\rho}}\} = \sum_n \rho_{nn} = \sum_j p_j \sum_n \langle\psi_n|\Psi_j\rangle\langle\Psi_j|\psi_n\rangle = \sum_j p_j = 1 \qquad , \tag{2.15}$$

diagonal elements ρ_{nn} are interpreted as populations of individual basis functions ψ_n. The off-diagonal elements ρ_{mn} $(m \neq n)$, named 'coherence elements are given by

$$\rho_{mn} = \sum_j p_j \langle\psi_m|\Psi_j\rangle\langle\Psi_j|\psi_n\rangle \qquad . \tag{2.16}$$

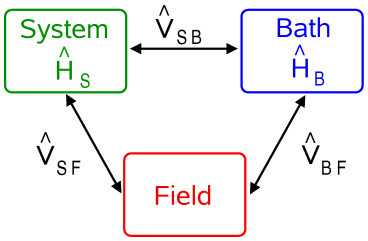

Figure 2.1: Schematic representation of system-bath separation and coupling to an external electric field. $\hat{H}$ and $\hat{V}$ denote system, bath and coupling Hamiltonians, respectively.

The expectation value $\langle \hat{A} \rangle$ of any operator $\hat{A}$ is given as,

$$\langle \hat{A} \rangle = \mathrm{Tr}\{\hat{\rho}\hat{A}\} = \sum_{j,n,m} p_j \langle \psi_n | \Psi_j \rangle \langle \Psi_j | \psi_m \rangle \langle \psi_m | \hat{A} | \psi_n \rangle \quad , \tag{2.17}$$

representing an average over measurable results $\langle \hat{A} \rangle$ for an ensemble of weighted Ψ_j.

2.4.2 The Liouville-von Neumann equation

Using the time-dependent Schrödinger equation (TDSE),

$$i\hbar \frac{\partial}{\partial t} \Psi = \hat{H} \Psi \tag{2.18}$$

and the definition of $\hat{\rho}$ in Eq. (2.13), the time derivative of $\hat{\rho}$ is expressed as,

$$i\hbar \frac{\partial}{\partial t} \hat{\rho} = \sum_j p_j \left(\hat{H} |\Psi_j\rangle\langle\Psi_j| - |\Psi_j\rangle\langle\Psi_j| \hat{H} \right) \quad , \tag{2.19}$$

resulting in the so-called Liouville-von Neumann (LvN) equation,

$$\frac{\partial}{\partial t} \hat{\rho} = -\frac{i}{\hbar} [\hat{H}, \hat{\rho}] = \mathfrak{L} \hat{\rho} \quad , \tag{2.20}$$

where $\mathfrak{L} = -\frac{i}{\hbar}[\hat{H}, \circ]$ is the Liouvillian superoperator acting on $\hat{\rho}$.

2.4.3 System-bath separation

The separation of system and bath entities, described by individual Hamiltonians $\hat{H}_S(\{q_s\})$ and $\hat{H}_B(\{q_b\})$, covering s system and b bath modes, is schematically shown in Fig. 2.1. Here, system and bath are coupled via the system-bath coupling operator $\hat{V}_{SB}(\{q_s, q_b\})$, using system and bath operators, $\hat{Q}_k$ and $\hat{F}_k$, respectively (e.g., position operators)[1]. System and bath parts are optionally coupled to an external electric field $\underline{E}(t)$ via coupling operators $\hat{V}_{SF}$ and $\hat{V}_{BF}$ [2]. In the field-free case, the entire Hamiltonian $\hat{H}$ for system and bath is written as, $\hat{H} = \hat{H}_S + \hat{H}_B + \hat{V}_{SB} = \hat{H}_0 + \hat{V}_{SB}$. Accordingly the LvN equation (2.20) can be written as

$$\frac{\partial}{\partial t} \hat{\rho} = -\frac{i}{\hbar} \left([\hat{H}_0, \hat{\rho}] + [\hat{V}_{SB}, \hat{\rho}] \right) \quad . \tag{2.21}$$

[1] Possible bilinear ansatz: $\hat{V}_{SB} = \sum_k \hat{Q}_k(q_1^s, \cdots, q_N^s) \cdot \hat{F}_k(q_1^b, \cdots, q_M^b)$

[2] Often the semi-classical dipole approximation is used: $\hat{V} = -\underline{\hat{\mu}}(\{q_i\}) \cdot \underline{E}(t)$; $\hat{\mu}$ - dipole operator.

After transformation from the 'Schrödinger picture' to the 'Interaction picture'[3]

$$\frac{\partial}{\partial t}\hat{\rho}^I = -\frac{i}{\hbar}[\hat{H}_0, \hat{\rho}^I] - \frac{i}{\hbar}[\hat{V}^I_{SB}, \hat{\rho}^I] = -\frac{i}{\hbar}[\hat{V}^I_{SB}, \hat{\rho}^I] \qquad , \tag{2.22}$$

the time derivative of $\hat{\rho}^I$ only depends on the system-bath coupling, while the inherent Hamiltonian part is contained in $\hat{\rho}^I$. Now, the equations of motion, solely for the system part ($\hat{\rho}^I_s$), are derived by tracing out the bath modes, $\mathrm{Tr_B}\{\hat{\rho}^I\}$, in Eq. (2.22). Prior to this, Eq. (2.22) is solved for $\hat{\rho}^I$ via integration over time and inserted in the same equation. The resulting LvN expression for the *reduced* density matrix,

$$\frac{\partial}{\partial t}\hat{\rho}^I_S(t) = \mathrm{Tr}_B\left\{-\frac{i}{\hbar}\left[\hat{V}^I_{SB}(t), \hat{\rho}^I(0)\right]\right\} - \frac{1}{\hbar^2}\int_0^t \mathrm{Tr}_B\left\{\left[\hat{V}^I_{SB}(t), \left[\hat{V}^I_{SB}(t'), \hat{\rho}^I(t')\right]\right]\right\} dt' \tag{2.23}$$

is not closed and non-local in time, which means that $\hat{\rho}^I$ depends on every previous time step for any propagation time $t > 0$. The second part of Eq. (2.23), integrating over time t is responsible for 'memory'. The equation is still exact, but has to undergo a number of approximations in order to arrive at a 'memory free' form. A *bath approximation* permits neglecting the correlation between system and bath, memory effects are switched off under the *Markov approximation*, leading to the *Redfield theory* with a time-dependent relaxation matrix (*Redfield tensor*). The *secular approximation* allows the use of a time-independent relaxation matrix instead [98].

2.4.4 The Lindblad 'dynamical semi-group' approach

Unfortunately the Redfield equations of motion (EOM), lacking the secular approximation, allow for negative state populations under certain initial conditions. Those are unphysical and not observable for non-Markovian theories [99]. Among others, the *Lindblad dynamical semi-group approach* [80], delivers EOM for $\hat{\rho}$ (used synonymously for $\hat{\rho}_S$ in the following) which include the Markov approximation and maintain both positive state populations and a conserved norm, $\sum_n \rho_{nn}$, for all times, by mathematical construction. The Lindblad form of the LvN equation for the reduced density matrix is,

$$\frac{\partial}{\partial t}\hat{\rho}(t) = \mathfrak{L}_S\hat{\rho} + \mathfrak{L}_D\hat{\rho} = -\frac{i}{\hbar}[\hat{H}_S, \hat{\rho}] + \mathfrak{L}_D\hat{\rho} \tag{2.24}$$

where $\mathfrak{L}_S$ and $\mathfrak{L}_D$ denote the system Hamiltonian and dissipative superoperators, respectively. The application of $\mathfrak{L}_D$ on $\hat{\rho}$ has to obey:

$$\mathfrak{L}_D\hat{\rho} = \sum_k \{\hat{C}_k\hat{\rho}\hat{C}_k^\dagger - \frac{1}{2}[\hat{C}_k^\dagger\hat{C}_k, \hat{\rho}]_+\} \qquad , \tag{2.25}$$

where the *Lindblad operators* $\hat{C}_k$ describe dissipative actions on the system via k possible channels. For population transfer processes between system levels due to vibrational dissipation or inelastic electron tunneling, for example, the following form of $\hat{C}_k$ is used [100]:

$$\hat{C}_k = \sqrt{W_{f\leftarrow i}}|\psi_f\rangle\langle\psi_i| \qquad . \tag{2.26}$$

[3] $\hat{A}^I(t) = e^{+i\hat{H}_0 t/\hbar}\hat{A}e^{-i\hat{H}_0 t/\hbar}$

Here, the $\hat{C}_k$ are projectors from an initial state $|\psi_i\rangle$ to a final state $|\psi_f\rangle$, weighted by the square root of W_{fi}, which is interpreted as a rate ($[W_{f\leftarrow i}] = 1/\text{time}$). Choosing, as an example, localized vibrational states as initial $|\tilde{\psi}_i\rangle$ or final state $|\tilde{\psi}_f\rangle$, the following EOM are found for diagonal elements ρ_{nn},

$$\frac{d}{dt}\tilde{\rho}_{nn}(t) = -\frac{i}{\hbar}\langle\tilde{\psi}_n|[\hat{H}_S,\hat{\rho}]|\tilde{\psi}_n\rangle + \sum_i W_{n\leftarrow i}\,\rho_{ii} - \sum_f W_{f\leftarrow n}\,\rho_{nn} \tag{2.27}$$

and off-diagonal elements ρ_{mn},

$$\frac{d}{dt}\tilde{\rho}_{mn}(t) = -\frac{i}{\hbar}\langle\tilde{\psi}_m|[\hat{H}_S,\hat{\rho}]|\tilde{\psi}_n\rangle - \frac{1}{2}\sum_f (W_{f\leftarrow m} + W_{f\leftarrow n})\rho_{mn} \quad , \tag{2.28}$$

applying expressions (2.24) to Eq. (2.26), respectively. For the moment, the dissipative superoperator $\mathfrak{L}_D = \mathfrak{L}_D^{vib}$ is therefore only accounting for changes in the vibrational state populations and connected dephasing, i.e., the loss of information about phase relations between individual states. Equations (2.27) and (2.28) are the further basis for the description of dissipation of vibrational energy using density matrix propagations.

2.4.5 Propagation in a localized state basis

As already stated, in order to follow the population transfer between two sets of localized states, the density matrix $\hat{\rho}$ and the Lindblad operators $\hat{C}_k$ are set up in a basis set of localized vibrational states, $\tilde{\rho}_{nm} = \langle\tilde{\psi}_n|\hat{\rho}|\tilde{\psi}_m\rangle$. This is necessary since the propagated density matrix becomes diagonal in the basis on to which the dissipative Lindblad operators $\hat{C}_k$ project on. The Hamilton matrix $\underline{\underline{\tilde{H}}}$, expanded in the localized state basis, is block-diagonal and the individual 2×2 blocks consist of energies $E_n^L = E_n^R$,

$$\begin{pmatrix} E_n^L & V_n \\ V_n & E_n^R \end{pmatrix} \quad , \tag{2.29}$$

and real coupling elements $V_n = \frac{1}{2}(E_n^+ - E_n^-)$, where $+$ and $-$ refer to the parity of the delocalized states. The Hamiltonian part $\mathfrak{L}_S\hat{\rho}$ is given as,

$$\langle\tilde{\psi}_m|\mathfrak{L}_S\hat{\rho}|\tilde{\psi}_n\rangle = -\frac{i}{\hbar}\langle\tilde{\psi}_m|[\hat{H}_S,\hat{\rho}]|\tilde{\psi}_n\rangle = -\frac{i}{\hbar}\sum_p \left[\tilde{H}_{mp}\tilde{\rho}_{pn} - \tilde{\rho}_{mp}\tilde{H}_{pn}\right] \quad , \tag{2.30}$$

introducing the completeness relation for the unlocalized basis, $\sum_p |\tilde{\psi}_p\rangle\langle\tilde{\psi}_p| = \hat{1}$. Tunneling or transfer between left and right localized states $\tilde{\psi}_n^{L,R}$ is driven via the off-diagonal elements V_n in the Hamiltonian part of the EOM and damped by the dissipative Liouvillian. The damping therefore depends on the transfer rates $W_{n\leftarrow m}$.

2.5 Population transfer rates based on Fermi's Golden Rule

2.5.1 Fermi's Golden Rule

As mentioned above, the system-bath separation of the open-system density matrix theory is used to represent both the dynamics of the system and all important system-bath

interactions. As stated in Sec. 2.4.4, population transfer rates $W_{f\leftarrow i}$ have to be specified in order to calculate the population dynamics under the influence of the system-bath coupling. According to Fermi's Golden Rule (FGR), the transition rate $W_{f\leftarrow i}$, between the two states Ψ_i and Ψ_f, can be calculated as,

$$W_{f\leftarrow i} = \frac{2\pi}{\hbar} \sum_i w_i(T) \sum_f [1 - w_f(T)] \cdot |\langle \Psi_f | \hat{V} | \Psi_i \rangle|^2 \cdot \delta(E_f - E_i) \quad . \tag{2.31}$$

Fermi's Golden Rule is based on first-order perturbation theory, applicable for a 'weak' coupling or a 'small' perturbation of the system. Equation (2.31) includes the averaging over initial states, and a summation over final states Ψ_f. Here, $w_i(T)$ and $w_f(T)$ are the statistical weights of initial and final state at temperature T, respectively. Further, $\hat{V}$ is the coupling operator, specifying the nature of the perturbation, while the delta function $\delta(E_f - E_i)$ ensures energy conservation. FGR is used to calculate the population transfer rates between individual system states, due to a perturbation of the system or coupling to a bath, for all density matrix propagations presented in the following. FGR is always applied on a set of left L or right R localized vibrational system states $\tilde{\psi}_i^{L,R}$ (see Sec. 2.3). For reasons of clarity the localized states are written as ψ without the tilde in the following until the end of the theory chapter.

One application of FGR below will be the vibrational relaxation of localized system states due to vibration-phonon coupling. This energy transfer due to vibration-phonon coupling is treated via two different models, namely via the *harmonic, bilinear coupling model* and the *Ohmic bath dissipative model*, respectively. For both, the lifetime of the first excited vibrational level τ_1^{vib} will appear as a parameter.

Another application is the calculation of rates due to inelastic electron tunneling (IET). Contributions arising from IET of electrons emitted or absorbed by an STM are treated for two different mechanisms. Either on the basis of a coupling between the electric field of the tunneling electron and the adsorbate dipole leading to $W_{f\leftarrow i}^{dip}$, and/or a transient population of its resonance electronic states leading to $W_{n\leftarrow m}^{res}$. IET-induced transfer rates are generally only included in single-surface (1S) models (see below). The total population transfer rate between localized states is a sum of the individual contributions,

$$W_{f\leftarrow i} = W_{f\leftarrow i}^{vib} + W_{f\leftarrow i}^{dip} + W_{f\leftarrow i}^{res} \quad . \tag{2.32}$$

2.5.2 Dissipative population transfer rates

(1) General expression for $W_{f\leftarrow i}^{vib}$:

Fermi's Golden Rule, Eq. (2.31), is used to calculate vibrational relaxation rates $W_{f\leftarrow i}^{vib}$ between initial and final states, $\Psi_i(q, Q_1, \ldots, Q_N)$ and $\Psi_f(q, Q_1, \ldots, Q_N)$, as a result of a vibrational coupling to a bath of oscillators. For now, only a one dimensional system is considered and both states are defined as products of system states $\psi_{i,f}(q)$ depending

on the spatial coordinate q and N 1 D bath oscillator states, $\chi_a^0(Q_a)$ and $\chi_a^1(Q_a)$, in their ground ($v = 0$) or first excited vibrational state ($v = 1$), respectively,

$$\Psi_i = \psi_i \cdot \prod_{a=1}^{N} \chi_a^0 \quad \text{and} \quad \Psi_f = \psi_f \cdot \chi_b^1 \cdot \prod_{c \neq b}^{N} \chi_c^0 \qquad . \tag{2.33}$$

Initially (Ψ_i), all bath oscillators are in their vibrational ground state χ^0, according to a bath temperature of 0 K. The STM experiments considered in the actual thesis were carried out around 4 K, justifying the choice of the initial bath state. The excited bath oscillator compensates, in terms of energy, for a vibrational relaxation ($i \rightarrow f$) in the system, meaning an excitation transfer from the system to the bath. There are several non-occupied final states ($w_f = 0$) considered.[4] Each final state Ψ_f, consist of a singly excited bath oscillator (χ_b^1) and the system state ψ_f. Using Eq. (2.31) and Eq. (2.33), the vibrational relaxation rate $W_{f \leftarrow i}^{vib}$ is expressed as,

$$W_{f \leftarrow i}^{vib} = \frac{2\pi}{\hbar} \sum_b |\langle \psi_f \cdot \chi_b^1 \cdot \prod_{c \neq b}^{N} \chi_c^0 | \hat{V}_{SB} | \psi_i \cdot \prod_{a=1}^{N} \chi_a^0 \rangle|^2 \cdot \delta(E_f - E_i) \qquad , \tag{2.34}$$

where $\hat{V}_{SB}$ is the dissipative, system-bath coupling operator, which is given in detail within the following subsection.

(2) Dissipation in the harmonic, bilinear limit:

In the harmonic, bilinear dissipative model, as will be introduced now, the coupling matrix elements in Eq. (2.34) can be calculated analytically. The model is based on two major assumptions. The first assumption is to consider system and bath vibrational states as harmonic. The second assumption is to specify the system-bath coupling as a bilinear operator, linear in system and bath coordinates [27],

$$\hat{V}_{SB} = \lambda_b \cdot q \cdot Q_b \qquad , \tag{2.35}$$

which describes the interaction between system mode q and a single bath oscillator b. Here, λ_b defines the vibration-phonon coupling strength between bath oscillator χ_b and the system. The product character of $\Psi_{i,f}$ and $\hat{V}_{SB}$ allows the separation of system and bath states, and Eq. (2.34) becomes,

$$W_{f \leftarrow i}^{vib} = \frac{2\pi}{\hbar} |\langle \psi_f | q | \psi_i \rangle|^2 \cdot \sum_{b=1}^{N} \lambda_b^2 |\langle \chi_b^1 | Q_b | \chi_b^0 \rangle \cdot \prod_{c \neq b}^{N} \underbrace{\langle \chi_c^0 | \chi_c^0 \rangle}_{=1}|^2 \cdot \delta(\hbar\omega_b - \hbar\omega_{if}) \qquad , \tag{2.36}$$

where ω_b and ω_{if} are the frequencies of system and bath phonons, respectively. Since system and bath states are harmonic, the respective coupling matrix elements are given analytically. The squared matrix elements containing system states in Eq. 2.36 scale linearly with system state number i,

$$|\langle \psi_f | q | \psi_i \rangle|^2 = i \cdot \frac{\hbar}{2m\omega_{if}} \cdot \delta_{i,f+1} \qquad , \tag{2.37}$$

[4] For a phonon-bath w_f and w_i are the Bose-Einstein coefficients $w_{i,f} = 1/(e^{E_{i,f}/(k_B \cdot T)} - 1)$.

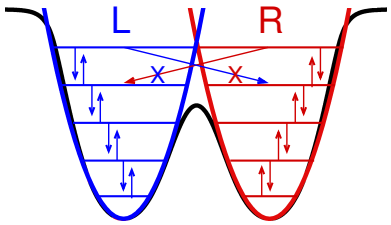

Figure 2.2: Dissipative vibrational transitions for the double-well potential treated as two independent harmonic oscillators. Harmonic selection rules ($\Delta v = \pm 1$) are obeyed and only transitions within the left (L) or right (R) well are possible.

where m is the system mass. The Kronecker delta $\delta_{i,f+1}$ preserves the harmonic selection rules ($\Delta v = \pm 1$) for all dissipative transitions ($f < i$). For the bath, the matrix elements are given in an analogous manner,

$$|\langle \chi_b^1 | Q_b | \chi_b^0 \rangle|^2 = \frac{\hbar}{2 M_b \, \omega_b} \quad , \tag{2.38}$$

with bath oscillator mass M_b. An additional replacement of λ_b by an overall coupling constant λ in Eq. (2.36) results in,

$$W_{f \leftarrow i}^{vib} = i \cdot \delta_{i,f+1} \cdot \frac{\pi}{m \omega_{if}} \cdot \lambda^2 \cdot \sum_{b=1}^{N} \frac{\hbar}{2 M_b \, \omega_b} \cdot \delta(\hbar\omega_b - \hbar\omega_{if}) = i \cdot \delta_{i,f+1} \cdot W_{0 \leftarrow 1}^{vib} \quad . \tag{2.39}$$

Here, $W_{0 \leftarrow 1}^{vib}$ subsumes the intra-bath-state matrix elements, multiplied by their respective delta-functions, as well as λ and other prefactors. Therefore, the lifetime of the first vibrational system state $\tau_1^{vib} = 1/W_{0 \leftarrow 1}^{vib}$ is the only adjustable parameter within the relaxation model. Finally, Eq. (2.39) provides a linear scaling law for dissipative, vibrational relaxation rates and/or lifetimes $\tau_i^{vib} = 1/W_{f \leftarrow i}^{vib}$ for all system states ψ_i.

Further, one can simply derive vibrational upward rates at finite temperatures via the condition of detailed balance, as shown in the following. Here, up- and downward population transfer rates ensure a Boltzmann distribution for all vibrational system states at a given temperature. Via the principle of detailed balance upward rates are calculated as,

$$W_{f \leftarrow i}^{vib}(T) = W_{i \leftarrow f}^{vib} \cdot e^{-(E_f - E_i)/k_B T} \quad . \tag{2.40}$$

The expressions given so far, apply to a single harmonic oscillator in the system part. The rate expressions, however, have to be adapted to a double-well potential, which resembles the bistable conformational switching dynamics. One could approximately see both wells as harmonic oscillator potential surfaces, which give rise to two independent sets of 'left' (L) or 'right' (R) localized harmonic eigenfunctions, $\tilde{\psi}_n^{L,R}$. For each of those sets the vibrational transition rates are calculated according to Eq. (2.39) and Eq. (2.40). This is schematically visualized in Fig. 2.2. Here, transitions due to dissipation or finite temperature are only possible within the 'left' or 'right' well of the double-well potential.

(3) Ohmic bath dissipative model:

The Ohmic bath dissipative model, as presented in the following, has several advantages compared to the simpler harmonic, bilinear scheme. First of all the Ohmic bath model

includes information about the phonon-bath, such as its cutoff energy, represented by $\tilde{\nu}_{cut}$, and its phonon-density. The latter is implicitly defined via $\tilde{\nu}_{cut}$, the number of bath oscillators N and a common energetic width γ, set for all bath oscillators. Further, the Ohmic bath approach includes anharmonicities of vibrational system states [101]a and the coupling matrix elements between all possible pairs of those system states $\psi_{i,f}$ are explicitly calculated. This is of special importance for the calculation of dissipative rates for more-dimensional potential surfaces. For the moment, only the 1 D formalism is presented, while the extension to two dimensions will be introduced in Sec. 4.4.3 as part of the COD@Si(100) chapter. Let us return to Eq. (2.36), slightly rewritten as

$$W^{vib}_{f\leftarrow i} = \frac{2\pi}{\hbar}\sum_{b=1}^{N} |\langle\psi_f|\lambda_b q|\psi_i\rangle|^2 \cdot |\langle\chi^1_b|Q_b|\chi^0_b\rangle|^2 \cdot \delta(\hbar\omega_b - \hbar\omega_{if}) \qquad . \tag{2.41}$$

For an Ohmic bath one chooses an equidistant frequency spacing,

$$\omega_b = b\cdot\Delta\omega_b = b\cdot\frac{\omega_{cut}}{N} = b\cdot\frac{2\pi c\tilde{\nu}_{cut}}{N} \qquad , \tag{2.42}$$

where c is the speed of light and defines the coupling constants λ_b as [102],

$$\lambda_b = b\left(\frac{2M_b\, m\,\gamma\,(\Delta\omega_b)^3}{\pi}\right)^{1/2} \qquad . \tag{2.43}$$

Using Eq. (2.43) and harmonic bath oscillators (Eq. (2.38)), Eq. (2.41) becomes,

$$W^{vib}_{f\leftarrow i} = 2\,|\langle\psi_f|\sqrt{m}q|\psi_i\rangle|^2 \cdot \gamma \cdot \sum_{b=1}^{N}\omega_b\,\delta(\hbar\omega_b - \hbar\omega_{if})\,\Delta\omega_b \qquad . \tag{2.44}$$

For an infinitely small frequency spacing (continuum limit, $\Delta\omega \rightarrow 0$, $\omega_b \rightarrow \omega$) and for ω_{if} centered in the bath phonon-band (wide-band limit, $0 \ll \omega_{if} \ll \omega_{cut}$), one can write,

$$W^{vib}_{f\leftarrow i} = 2|\langle\psi_f|\sqrt{m}q|\psi_i\rangle|^2\cdot\gamma\cdot\frac{1}{\hbar}\int\omega\,\delta(\omega-\omega_{if})\,d\omega = \frac{2}{\hbar}|\langle\psi_f|\sqrt{m}q|\psi_i\rangle|^2\cdot\gamma\cdot\omega_{if} \qquad . \tag{2.45}$$

If one finally assumes harmonic vibrational system states, Eq. (2.37) can be used,

$$W^{vib}_{f\leftarrow i} = i\cdot\delta_{i,f+1}\cdot\gamma = i\cdot\delta_{i,f+1}\cdot W^{vib}_{1\leftarrow 0} \tag{2.46}$$

Therefore, $\gamma = 1/\tau^{vib}_1$ turns out to be identical with the inverse vibrational lifetime of the first excited vibrational system state in this case.

For the actual calculations of dissipative rates via the Ohmic bath model below, anharmonic system states are used and all coupling matrix elements $\langle\psi_f|q|\psi_i\rangle$ are calculated explicitly. Also, neither the continuum limit nor the wide-band limit are applied. For the conclusive 1 D rate equation the delta function in Eq. 2.44 is replaced by a Lorentz function of width γ_L,

$$W^{vib}_{f\leftarrow i} = 2|\langle\psi_f|q|\psi_i\rangle|^2\cdot m\cdot\gamma\cdot\Delta\omega_b\cdot\sum_{b=1}^{N}\omega_b\cdot\frac{1}{\pi}\cdot\frac{\gamma_L}{\gamma_L^2+(\hbar\omega_b-\hbar\omega_{if})^2} \qquad . \tag{2.47}$$

Temperature-dependent vibrational upward rates are treated the same way as in the bilinear, harmonic case, namely via the condition of detailed balance, as written in Eq. (2.40). Temperature related corrections via Bose-Einstein coefficients (see page 17) led only to negligible effects, for COD@Si(100) studied in the following.[5] Those corrections are not included, as for the bilinear, harmonic model.

It should also be mentioned that the strict separation of left and right well, as shown in Fig. 2.2 is an approximation, which is only valid for perfectly L/R- localized states. The harmonic, bilinear model does not allow for $L \leftrightarrows R$ transitions by definition, the Ohmic bath approach does allow for $L \leftrightarrows R$ transitions, due to non-perfectly localized states.

2.5.3 Inelastic Electron Tunneling (IET)-induced excitations

As stated in the introduction regarding the STM-experiment, there are two major contributions to the inelastic tunneling current fraction $\eta = I_{in}/I$, namely inelastic dipole and resonance scattering. I_{in} represents the inelastic tunneling current fraction, while I is the measurable STM tunnel current. In the following an estimate for η and the resulting electron-phonon coupling, i.e., transition rates between individual vibrational adsorbate levels $W_{f\leftarrow i}$, are given. Dipole and below-threshold resonance excitations will be treated in a 'single-surface model', adopted from Walkup et al. [70, 71]. Their harmonic model is extended here. First, tunneling between two wells of a double minimum potential is treated in an exact quantum mechanical way, without any rate approximations. Secondly, IET-induced transitions between all vibrational levels are included and explicitly calculated, instead of using simple linear scaling laws only. Perturbative rate expressions, covering the dipole scattering and the 'below-threshold' regime of resonance scattering, as used by Walkup et al., are introduced in the following.

(1) Dipole scattering rates $W^{dip}_{f\leftarrow i}$:

Electrons tunneling between the STM tip and surface are accompanied by an electric field. The field can couple to the transition dipole moment μ_{fi} of an adsorbate-surface vibration,

$$\mu_{fi} = \langle \psi_f | \hat{\mu}_z | \psi_i \rangle \qquad , \tag{2.48}$$

and induce a transition between vibrational states ψ_i and ψ_f. The adsorbate dipole component μ_z, perpendicular to the surface, is of interest here since this direction corresponds to the dominant direction of the flowing electrons. The number of tunneling electrons causing vibrational transitions accounts for the inelastic, dipole-induced tunneling fraction $\eta^{dip} = I^{dip}_{in}/I$. The ratio between dipole-inelastic and elastic current fraction is typically in the order of 10^{-3} to 10^{-4} [34, 76]. The dipole-induced transition rates $W^{dip}_{f\leftarrow i}$ between levels ψ_i and ψ_f are calculated by a formula, based on the work of Persson et al. [25] and

[5] Relevant example: $\omega = 2\pi \cdot c \cdot 200\, cm^{-1} \Rightarrow w_1(150\,\mathrm{K}) = 1/(e^{24.8\,\mathrm{meV}/(k_B \cdot 150\,\mathrm{K})} - 1) \approx 0.06$

utilized by Walkup et al. [71]. The expression derived by Persson is,

$$W^{dip}_{f\leftarrow i} = \frac{I}{e}\cdot\eta^{dip}_{f\leftarrow i} = \frac{I}{\mathrm{e}}\cdot\left|\frac{\langle\psi_f|\hat{\mu}_z|\psi_i\rangle}{ea_0}\right|^2 \quad , \tag{2.49}$$

where a_0 is the Bohr radius, e the electron charge and I the STM tunnel current. Finally, $\eta^{dip}_{f\leftarrow i}$ is the inelastic current fraction generating the vibrational transition $f \leftarrow i$ due to dipole transitions. The formalism was derived under the following assumptions. First, the electrons are supposed to tunnel from or to an s-shaped orbital of a single metal atom in the STM tip. Also, the tip has to be positioned directly above the adsorbate. Further, the distance and orientation of contributing orbitals are taken as 'optimal' and the limits of perturbation theory, i.e. FGR have to be obeyed.

Persson and Walkup also considered the inelastically dipole-scattered fraction of the current in the harmonic limit, $\eta^{dip'}$. Here, functions $\psi'_{i,f}$ are assumed to be harmonic oscillator functions and the dipole moment is linearized, $\mu_z(q) \approx \mu_{z,0} + \mu'_{z,0}\cdot(q-q_0)$. Here, $\mu_{z,0}$ and $\mu'_{z,0}$ denote the dipole moment at the position of the potential minimum and the first derivative of $\mu_z(q)$ at this point, respectively.

In this double-harmonic approximation, the squared matrix elements $|\mu'_{z,0}\cdot\langle\psi'_{i+1}|q|\psi'_i\rangle|^2$ scale linearly with state number i and harmonic selection Rules $\Delta v = \pm 1$ apply for the transition rates,

$$W^{dip}_{i+1\leftarrow i} = (i+1)\cdot\eta^{dip'}\cdot\frac{I}{\mathrm{e}} = (i+1)\cdot\frac{|\mu'_{z,0}\langle\psi'_1|q|\psi'_0\rangle|^2}{(\mathrm{e}\,\mathrm{a}_0)^2}\cdot\frac{I}{\mathrm{e}} = (i+1)\cdot\frac{{\mu'_{z,0}}^2}{(\mathrm{e}\,\mathrm{a}_0)^2}\cdot\frac{\hbar}{2\,m\,\omega_0}\cdot\frac{I}{\mathrm{e}} \quad , \tag{2.50}$$

where m and ω_0 are the harmonic oscillator mass and frequency, respectively. Here,

$$\eta^{dip'} = \frac{{\mu'_{z,0}}^2}{(\mathrm{e}\,\mathrm{a}_0)^2}\cdot\frac{\hbar}{2\,m\,\omega_0} \tag{2.51}$$

is the inelastically dipole-scattered current fraction, for the $1 \leftarrow 0$ transition in the harmonic limit.

For the actual thesis, Eq. (2.49) is applied for the two sets of localized, anharmonic wavefunctions $\tilde{\psi}_{i,f}$. Here, the dipole transition rates between *all* state pairs $W^{dip}_{f\leftarrow i}$ are calculated explicitly. Further, for the perpendicular dipole component $\mu_z(q)$ the linear approximation is not made. The expression is more general and now applicable to anharmonic systems, which might not obey harmonic selection rules and a linear rate scaling. Two-, or more, dimensional systems can easily be treated via Eq. (2.49) as well.

(2) Resonance scattering rates $W^{res}_{f\leftarrow i}$ (Below-threshold regime):

Another important excitation channel for STM-induced adsorbate vibrations opens up if the energy of tunneling electrons (holes) is close to an adsorbate resonance. The traveling electron (hole) might be temporarily trapped in the resonance. Therefore, the nuclear potential is changed and a net force acts on the system atoms. During an inelastic relaxation a transfer of phonon-energy $\hbar\omega$, from the electron to the adsorbate, takes place. The

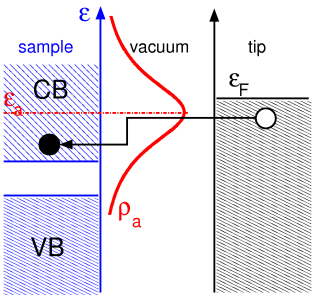

Figure 2.3: Schematic picture of resonance inelastic electron tunneling from an occupied electronic tip state (black) through the adsorbate resonance (red) to the conduction band (CB) of the semiconductor (SC) surface bulk. VB is the valence band of the SC. ϵ_a is the energy of the adsorbate resonance and ϵ_F the Fermi level of the STM tip and ρ_a represents the adsorbate resonance density of states, respectively.

physical picture of such resonance-mediated, inelastic electron-phonon scattering event is shown for the case of an anion resonance in Fig. 2.3. Here, the Fermi level of the tip ϵ_F overlaps with the resonance energy of an unoccupied state ϵ_a. The excitation probability is proportional to the resonance density of states ρ_a at the Fermi level [24]. The amount of vibrational energy transferred from the electron also depends on the resonance lifetime and on the difference between ground and resonance state potential surface. Several estimates for the inelastic, resonant tunneling fraction $\eta^{res} = I^{res}_{in}/I$ of the current can be found in the literature. For small molecules adsorbed on metal [26, 70, 103] or semiconductor surfaces [29, 32, 103], typically $\eta^{res} \approx 1 \times 10^{-3}$.

Taking into account the mentioned physical parameters we calculate the inelastic tunneling fraction η^{res} in the *below-threshold regime* as follows. Here, the Fermi level of the STM-tip is *below* the energy of the resonance center (anion resonance). The resonance-induced, vibrational excitation of the system is taken into account via electronic ground state vibrational transition rates $W^{res}_{f\leftarrow i}$. The utilized expression is again based on first order perturbation theory according to Persson et al. [26],

$$W^{res}_{fi} = \frac{I}{\mathrm{e}} \cdot \eta^{res}_{f\leftarrow i} = \frac{I}{\mathrm{e}} \cdot \frac{|\langle\psi_f|V_{es}(q) - V_{gs}(q)|\psi_i\rangle|^2}{(\Delta E_{res})^2 + (\gamma^{\downarrow}_{el}/2)^2} \quad . \tag{2.52}$$

The formula includes the difference between ground state potential $V_{gs}(q)$ and resonant state potential $V_{es}(q)$, if a one-dimensional system with coordinate q is assumed. Further, ΔE_{res} is the difference between resonance energy ϵ_a and the Fermi level of the STM tip ϵ_F,

$$\Delta E_{res} = \epsilon_\mathrm{a} - \epsilon_\mathrm{F} = \epsilon^0_\mathrm{a} - \epsilon^0_\mathrm{F} - \mathrm{e}\cdot U = \Delta E^0_{res} - \mathrm{e}\cdot U \quad . \tag{2.53}$$

Here, ϵ^0_a and ϵ^0_F are the energies of the adsorbate resonance and the Fermi level of the tip, respectively, if no bias voltage is applied ($U = 0\,\mathrm{V}$). ΔE^0_{res} is the corresponding energy gap and e is the elementary charge. Via proper adjustment of the STM bias voltage U, electrons or holes can tunnel from the STM tip and through the adsorbate resonance depending on the character of the resonance.

$\gamma^{\downarrow}_{el} = \hbar/\tau_{res}$ accounts for the resonance width as inverse of the resonance lifetime τ_{res}. Finally, $\eta^{res}_{f\leftarrow i}$ is the inelastic, resonant-induced tunneling current fraction causing the vibrational transition $i \rightarrow f$.

As for the dipole component, the harmonic limit is considered, where the transition rates scale linearly with the state number and obey harmonic selection rules. Accordingly, $\psi'_{i,f}$

above-threshold		below-threshold	
+	-	+	-
$\epsilon_F < \epsilon_a$	$\epsilon_F > \epsilon_a$	$\epsilon_F > \epsilon_a$	$\epsilon_F < \epsilon_a$

Table 2.1: Comparison of the Fermi energy of the STM-tip ϵ_F and the resonance energy ϵ_a for below- and above-threshold resonant switching regimes and anion (−) or cation (+) type of resonance.

are harmonic oscillator states and the difference potential is linearized,

$$V_{es}(q) - V_{gs}(q) = V_{es}(q_0) - V_{gs}(q_0) + V'_{es}(q_0) \cdot (q - q_0) \quad . \tag{2.54}$$

Here, q_0 is the minimum position of the harmonic oscillator and $V'_{es}(q_0)$ is the first derivative of the resonance state potential with respect to q. The resulting expression,

$$\begin{aligned} W^{res}_{i+1\leftarrow i} &= (i+1) \cdot \eta^{res'} \cdot \frac{I}{\mathrm{e}} = (i+1) \cdot \frac{|V'_{es}(q_0)\langle\psi'_1|q|\psi'_0\rangle|^2}{(\Delta E_{res})^2 + (\gamma^{\downarrow}_{el}/2)^2} \cdot \frac{I}{\mathrm{e}} \\ &= (i+1) \cdot \frac{(V'_{es}(q_0))^2}{(\Delta E_{res})^2 + (\Gamma^{\downarrow}_{el}/2)^2} \cdot \frac{\hbar}{2m\,\omega_0} \cdot \frac{I}{\mathrm{e}} \end{aligned} \tag{2.55}$$

,

provides the definition for the harmonic, inelastic, resonant tunneling current fraction,

$$\eta^{res'} = (V'_{es}(q_0))^2 \cdot \frac{\hbar}{2m\,\omega_0} \cdot \frac{1}{(\Delta E_{res})^2 + (\Gamma^{\downarrow}_{el}/2)^2} \quad , \tag{2.56}$$

where ω_0 and m are harmonic oscillator frequency and mass again, respectively.

The perturbation theory of first order (see also Sec. 2.5) only covers the 'weak' coupling limit. The limit is fulfilled only if nearly all the electronic ground state population remains in the vibrational ground state. Further the resonance center has to be far away, in terms of energy, from the Fermi level of the tip, which is the case in the 'below-threshold' regime considered here (see Tab. 2.1). All important dynamics should take place in the ground state, because the excited, resonance state is not explicitly included and enters only indirectly via transition rates on the ground state. Depending on the gradient of the excited state surface, the excited state lifetime has to be short enough to fulfill that condition. Further, it should be mentioned that the resonance width depends on the distance of the adsorbate to the surface. For both systems studied here that distance is rather constant during the switching process. The coordinate dependence of $\gamma^{\downarrow}_{el}$ is therefore neglected here. An extension to higher dimensional problems is also straightforward.

2.6 Resonance scattering in the above-threshold regime

In the above threshold regime of resonant switching, the weak coupling limit is left, since the resonance center is located in resonance to the Fermi energy of the tip (see Tab. 2.1). Therefore, resonance trapping of the tunneling electron becomes much more likely due to the experienced maximum of the resonance density of states. In the above threshold regime of resonance IET a 'two-surface model' is used, which allows for the study of

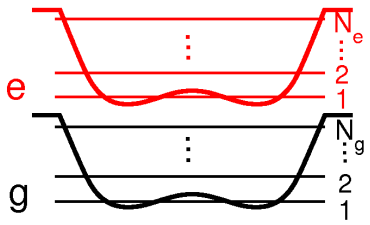

Figure 2.4: Schematic view of a two-surface system including electronic ground state (g) and resonant electronic state (e), which give rise to N_g and N_e vibrational levels.

the adsorbate dynamics in its resonance state. The resonance lifetime and the ratio of resonance tunneling current I_r with respect to the overall tunneling current I, enters as parameters in our model. The propagations are realized in the framework of density matrix theory, as explained in the following section.

2.6.1 Two-surface density matrix propagation

The transient population of ion resonances, via STM-induced injection or detachment of electrons into or from the adsorbate-surface system, can also be treated in the 'above threshold' limit (see Sec. 1.3). The two-surface model includes the electronic ground state $|g\rangle$, represented by N_g vibrational wavefunctions $\psi^g_{n,m}$ and the resonant, excited electronic state $|e\rangle$, represented by N_e vibrational wavefunctions $\psi^e_{\alpha,\beta}$, as illustrated in figure 2.4. The density operator $\hat{\rho}$ (see Sec. 2.4.1) is represented in the electronic state basis, consisting of a ground state $|g\rangle$ and an excited, resonant state $|e\rangle$,

$$\hat{\rho} = \hat{\rho}_{gg}|g\rangle\langle g| + \hat{\rho}_{ge}|g\rangle\langle e| + \hat{\rho}_{eg}|e\rangle\langle g| + \hat{\rho}_{ee}|e\rangle\langle e| \quad . \tag{2.57}$$

Here, the diagonal elements $\hat{\rho}_{gg}$ and $\hat{\rho}_{ee}$ represent populations of ground and excited state, while the off-diagonal elements $\hat{\rho}_{ge}$ and $\hat{\rho}_{eg}$, account for coherences between both electronic states. The latter one will not be considered in the two-state simulations of resonant excitations for the following reasons. The density matrix is always initialized as a 'pure' electronic state, with unit population in the excited state. Further, no coherent coupling term is considered for the Hamiltonian superoperator $\mathfrak{L}_S$. Therefore, equation (2.57) simplifies to

$$\hat{\rho} = \hat{\rho}_{gg}|g\rangle\langle g| + \hat{\rho}_{ee}|e\rangle\langle e| \quad . \tag{2.58}$$

The population loss in the resonance and the population gain in the electronic ground state are mediated via an dissipative electronic superoperator $\mathfrak{L}^{el}_D$, which is added to the LvN equation in Lindblad form (Eq. (2.24)),

$$\frac{\partial}{\partial t}\hat{\rho}(t) = \mathfrak{L}_S\hat{\rho} + \mathfrak{L}^{vib}_D\hat{\rho} + \mathfrak{L}^{el}_D\hat{\rho} \quad . \tag{2.59}$$

In accordance to equation (2.25), $\mathfrak{L}^{el}_D\hat{\rho}$ is chosen as,

$$\mathfrak{L}^{el}_D\hat{\rho} = \hat{C}_{el}\hat{\rho}\hat{C}^{\dagger}_{el} - \frac{1}{2}[\hat{C}^{\dagger}_{el}\hat{C}_{el}, \hat{\rho}]_+ \quad . \tag{2.60}$$

where $\hat{C}_{el}$ is the electronic Lindblad operator,

$$\hat{C}_{el} = \sqrt{\gamma^{\downarrow}_{el}}|g\rangle\langle e| \quad . \tag{2.61}$$

Here, $\gamma_{el}^{\downarrow} = \frac{1}{\tau_{res}}$ is the resonance decay rate ($\hbar\Gamma_{res}^{downarrow}$ is the resonance width) and τ_{res} the corresponding resonance lifetime. The combination of equation (2.60) and equation (2.61),

$$\mathfrak{L}_D^{el}\hat{\rho} = \gamma_{el}^{\downarrow}\left[|g\rangle\langle e|\hat{\rho}|e\rangle\langle g| - \frac{1}{2}\left(|e\rangle\langle e|\hat{\rho} + \hat{\rho}|e\rangle\langle e|\right)\right] \quad , \tag{2.62}$$

permits the calculation of the time derivatives of diagonal elements[6] of the density matrix in the electronic state basis under the influence of electronic dissipation, as represented by $\mathfrak{L}_D^{el}$:

$$\frac{d\hat{\rho}_{gg}}{dt} = \langle g|\mathfrak{L}_D^{el}\hat{\rho}|g\rangle = \gamma_{el}^{\downarrow}\hat{\rho}_{ee} \quad , \tag{2.63}$$

$$\frac{d\hat{\rho}_{ee}}{dt} = \langle e|\mathfrak{L}_D^{el}\hat{\rho}|e\rangle = -\gamma_{el}^{\downarrow}\hat{\rho}_{ee} \quad . \tag{2.64}$$

Finally, the density matrix is represented in the vibrational state basis $|\psi_{m,n}^{g}\rangle$ and $|\psi_{\alpha,\beta}^{e}\rangle$, for ground and excited electronic states, respectively.

$$\hat{\rho}_{gg} = \sum_{m,n}^{N_g}|\psi_m^g\rangle\langle\psi_m^g|\hat{\rho}_{gg}|\psi_n^g\rangle\langle\psi_n^g| = \sum_{m,n}^{N_g}|\psi_m^g\rangle\rho_{gg}^{mn}\langle\psi_n^g| \quad , \tag{2.65}$$

$$\hat{\rho}_{ee} = \sum_{\alpha,\beta}^{N_e}|\psi_\alpha^e\rangle\rho_{ee}^{\alpha\beta}\langle\psi_\beta^e| \quad , \tag{2.66}$$

Equations (2.63) and (2.64) show that a gain of ground state population and a loss of excited state population, after a resonant excitation, follows a mono-exponential decay according to first order kinetics. This permits an easy check for proper functioning of the two-surface propagation. Looking back at equations (2.63) and (2.64), access is gained to the time-evolution of individual density matrix elements in the full vibronic basis, using product basis functions of electronic and vibrational basis functions. Equations (2.67) and (2.68),

$$\left(\frac{d(\rho_{gg}^{mn})}{dt}\right)_D^{el} = \langle g\psi_g^m|\mathfrak{L}_D^{el}\hat{\rho}|g\psi_g^n\rangle = \gamma_{el}^{\downarrow}\sum_{\alpha,\beta}\langle\psi_g^m|\psi_e^\alpha\rangle\rho_{ee}^{\alpha\beta}\langle\psi_e^\beta|\psi_g^n\rangle \quad , \tag{2.67}$$

$$\left(\frac{d(\rho_{ee}^{\alpha\beta})}{dt}\right)_D^{el} = \langle e\psi_e^\alpha|\mathfrak{L}_D^{el}\hat{\rho}|e\psi_e^\beta\rangle = -\gamma_{el}^{\downarrow}\rho_{ee}^{\alpha\beta} \quad , \tag{2.68}$$

describe the time derivatives of electronic ground state and excited state vibrational populations, respectively. Here $\langle\psi_g^m|\psi_e^\alpha\rangle$ and $\langle\psi_e^\beta|\psi_g^n\rangle$ are overlap matrix elements factors between electronic ground state and excited state vibrational levels.

The vibrational, dissipative superoperator $\mathfrak{L}_D^{vib}$ in equation (2.59) is only acting on the ground state density operator $\hat{\rho}_{gg}$ in the following, since the typical resonance lifetime of a few fs excludes any influence of vibrational dissipation on a typical timescale of ps for the resonance. The corresponding equations of motion for $\hat{\rho}_{gg}$ in a localized vibrational state basis were already defined via Eq. (2.27) and Eq. (2.28).

[6] Populations of ground and excited electronic states

All two-surface density matrix propagations started with a fully localized vibrational ground state population, projected to the resonant surface. The propagation terminates when all population has been trapped into non-switching vibrational levels of the electronic ground state, due to electronic and vibrational relaxation.

2.6.2 Alternative two-surface models

(1) Gadzuk's 'jump and weighted average' procedure:

Gadzuk's 'jump and weighted average' procedure represents an alternative and efficient description of a single electronic excitation/relaxation cycle within a two level system. The algorithm consists of the following steps. First, the initial ground state wave packet $\theta(t=0)$ is projected to the excited state $|e\rangle$ and propagated for a specific residence time τ_R. Afterwards, the wave packet is back-projected to the electronic ground state $|g\rangle$ and propagated until the final time, t. In summary, the following equation of motion is used,

$$|\theta(t,\tau_R)\rangle = \exp\left\{-\frac{i\hat{H}_g(t-\tau_R)}{\hbar}\right\}|g\rangle\langle e|\exp\left\{-\frac{i\hat{H}_e\,\tau_R}{\hbar}\right\}|e\rangle\langle g|\theta(t=0)\rangle \quad . \tag{2.69}$$

utilizing the formal solution of the TDSE (Eq. (2.18)), Here $\hat{H}_g$ and $\hat{H}_e$ represent the nuclear Hamiltonians of ground and excited state electronic states, respectively. Considering the excited state lifetime to be independent from the nuclear coordinates, the excited state population decays exponentially with time. Therefore, any global expectation value $\langle\hat{A}\rangle(t)$ is derived via an incoherent averaging scheme,

$$\langle\hat{A}\rangle(t) = \frac{1}{\tau_{el}}\int_0^\infty \exp(-\tau_R/\tau_{el})A(t,\tau_R)d\tau_R = \int_0^\infty w(\tau_R)A(t,\tau_R)d\tau_R \quad , \tag{2.70}$$

of expectation values $A(t,\tau_R) = \langle\theta(t,\tau_R)|\hat{A}|\theta(t,\tau_R)\rangle$ for individual values of τ_R, using an exponential weight function $w(\tau_R)$. Here, τ_{el} is the average lifetime of the electronically excited state. In practice, only the sum over an appropriate set of different τ_R is taken.

(2) Monte Carlo wave packet (MCWP) method:

The Gadzuk algorithm was proven to be equivalent to an open-system density matrix approach [104], since it represents a special variant of the Monte Carlo wave packet method [105, 104, 27] which belongs to the class of stochastic wave packet methods. MCWP is particularly suitable for problems with a large number of eigenstates N, where the storage and/or propagation of a $N \times N$ density matrix is difficult, because only a single wave function rather than a statistical average, as in the full density matrix, is propagated for each trajectory. In the Lindblad form a non-Hermitean Hamiltonian acts on the propagated wave packet allowing for a loss of norm. Connected to a random number generator, the loss triggers jumps between electronic surfaces which is followed by a renormalization. The expectation values are averaged over all trajectories. A slow convergence with the number of trajectories might occur, depending on the actual system.

2.7 Calculation of switching rates

(1) Single-surface model:

The switching rate between both potential wells is calculated with respect to the propagation time or the number of tunneling electrons. First of all, the total population for the left or right well $P_{L,R}(t)$ has to be calculated at certain times during the propagation. The operator $\hat{P}_{L,1D}$, for example, is used to obtain the probability of the 1 D wave packet to be localized in the 'left half' of the grid ($-\infty < q \leq 0$) at any time,

$$\hat{P}_{L,1D} = \sum_{k=1}^{K/2} |\varphi_k\rangle\langle\varphi_k| \quad , \tag{2.71}$$

by projecting out the 'right half' ($0 < q < +\infty$), where φ_i are the basis functions used to represent the vibrational wavefunctions on the grid, using K sampling points (see Sec. 2.2). Applying Eq. (2.17) and (2.71) on $\underline{\underline{\rho}}$ results in the following expectation value of $\hat{P}_L$,

$$P_L = \left\langle \hat{P}_L(t) \right\rangle = \sum_{n,m} \rho_{nm}(t) \sum_{k=1}^{K/2} c_{km} c_{kn} \quad . \tag{2.72}$$

The probability to be localized to the 'right' is $P_R(t) = 1 - P_L(t)$ Starting with 100% population in the left well, for example, the switching rate, R_{sw}, can be defined as,

$$R^t_{sw} = -\frac{dP_L(t)}{dt} = \frac{dP_R(t)}{dt} \quad , \tag{2.73}$$

assuming a negligible back flow of population, or $P_L(t) \approx 1$ and $P_R(t) \approx 0$ when starting from the left. For a constant switching rate, as seen for those examples considered in this thesis, $R_{sw}(t)$ can be simply estimated as,

$$R_{sw}(t - 1/2\Delta t)\,[1/s] = \frac{\Delta P_R}{\Delta t} = \frac{P_R(t) - P_R(t - \Delta t)}{\Delta t} \quad . \tag{2.74}$$

The switching rate per tunneling electron R^e_{sw} [1/e] is simply obtained by dividing R^t_{sw} by the STM current I, $R^e_{sw} = R^t_{sw}/I$.

(2) Two-surface model:

In the two-surface model R^e_{sw} is calculated differently. At first, only the switching probability of a single, electronic excitation event is calculated. After an initial projection of an left or right well localized single state or wave packet to the resonance state surface and the exponential back-decay, the wave packet relaxes vibrationally in the ground state. When all population relaxes to states which are 'trapped' in either of the ground state potential wells, the final population of the initially empty well ($P(t \to \infty)$) is taken as switching probability per electronic excitation event $R^{e'}_{sw}$. For a comparison to observable

values of the total switching probability R^e_{sw}, the excitation probability W_{exc} has to be known and multiplied with $R^{e'}_{sw}$,

$$R^e_{sw} = W_{exc} \cdot R^{e'}_{sw} = (I^{res}/I) \cdot R^{e'}_{sw} \quad . \tag{2.75}$$

Here I^{res}/I accounts for the ratio between the resonant tunneling current fraction and and the overall, measurable tunneling current I. A quantitative comparison between theoretical and experimentally observed switching rates can only be as good as the estimate of W_{exc}. However, the qualitative description of the switching mechanism is *not* affected by this uncertainty.

2.8 Quantum chemical methods

Since quantum chemical calculations are not the main scope of this thesis, a detailed explanation of the foundations of the utilized methods, such as density functional theory (DFT) [106] and complete active space self-consistent field (CASSCF) [107], is not included here. For DFT, we use the B3LYP functional which is composed of Becke‘s three-parameter hybrid exchange functional and the Lee-Yang-Parr correlation functional [108, 109], both including gradient corrections. Besides B3LYP its spin-unrestricted variant (UB3LYP), was utilized in this work. The 6-31G(d) basis set [110] was further used as standard basis set for all calculations in this work. The (U)B3LYP functional was employed to calculate potential and dipole surfaces for the examined silicon adsorbate systems. Alternatively, the gradient corrected, non-hybrid (U)PW1 correlation and exchange functionals of Perdew and Wang et al. [111] were used for test calculations. CASSCF is applied for the calculation of the dipole function of H@Si(100). As a variant of the multi-configuration MC-SCF method, it allows for an optimization of both, coefficients of electronic configuration state functions and molecular orbitals, within a defined active space of occupied and unoccupied molecular orbitals. The method is especially useful to cover static correlation effects and to describe excited electronic states. All methods are used, as implemented in the Gaussian03 program package [112].

2.9 Resonant state potentials via Koopmans' theorem

Transient, electronically excited, anionic or cationic system states can be populated via resonance electrons tunneling between system and STM-tip. The excited system evolves within the lifetime of the resonance state. To simulate the resonance-induced system dynamics, the potential surface V_{es} of the excited state involved has to be known (see, e.g., Eq.(2.52)). Having already calculated the orbital energies along the neutral potential surface, it is straightforward to derive approximate anion and cation surfaces via the application of Koopmans' theorem [113]. According to Koopmans' theorem the energies of the highest occupied and lowest unoccupied molecular orbitals ϵ_{HOMO} and ϵ_{LUMO} are

approximative vertical ionization potentials (VIP) and electron affinities (EA), respectively: $VIP \approx -\epsilon_{HOMO}, \quad EA \approx -\epsilon_{LUMO}$. For Hartree-Fock (HF) and an adequate basis set, the error for Koopmans' VIP's is usually less than 10 %, while the EA values via Koopmans' are known to be less reliable and strongly basis set dependent. There are two major approximations made by Koopmans' theorem. The first is the so-called *frozen orbital approximation*, since orbital relaxation upon ionization is neglected. This causes an overestimation of VIPs and an underestimation of EAs, respectively. The error does not occur for the so-called 'ΔSCF method', taking the difference between two separate ground state energies of ionic and neutral state, respectively. The second error contribution comes from ignoring correlation effects, which results in an underestimation of VIPs and an overestimation of EAs. Therefore, the second error contribution has an opposite effect, as compared to the relaxation error, resulting in a partial error cancellation [114]. Density functional theory (DFT)-based ΔSCF calculations, using functionals which partly cover correlation energy, reduce that error [115]. In the actual work the resonance anion and cation surface energies $V^{-}_{es,n}$ and $V^{+}_{es,n}$ were approximated, using Koopmans' theorem and Kohn-Sham orbital energies calculated with the B3LYP functional [108, 109] and 6-31G(d) basis set [110] as,

$$\begin{aligned} V^{+}_{es,n}(q) &= V_{gs}(q) - V_{gs}(q_0) - \Phi_W - \epsilon_{HOMO-n}(q) \qquad \text{and} \\ V^{-}_{es,n}(q) &= V_{gs}(q) - V_{gs}(q_0) + \Phi_W + \epsilon_{LUMO+n}(q) \qquad . \end{aligned} \tag{2.76}$$

Here q denotes the spatial degree of freedom along which the 1 D potential is defined. $V_{gs}(q)$ is the neutral ground state potential, $V_{gs}(q_0)$ is its global minimum[7] and $\epsilon_{HOMO/L}(q)$ are the HOMO and LUMO energies along q, also for the neutral ground state. Φ_W denotes the work function[8] for the STM-tip and is set here to 4.5 eV for tungsten.

The use of the Kohn-Sham orbital energies to estimate VIPs is exact for the HOMO, if an exact functional would be used [116]. Energies of 'lower' occupied orbitals are interpreted as approximate 'orbital-relaxed' VIPs. The quality of that interpretation decreases parallel to the increase of inner shell character for the considered orbital. Unfortunately, the use of common, non-exact, exchange-correlation functionals, as for example B3LYP, can result in absolute errors of several eV, compared to experiment. But, in the case of B3LYP (and other functionals), a uniform shift of VIP's, predicted by Koopmans' theorem, and experimental values have been demonstrated by several authors [117, 115, 118]. The findings justify the assumption that the B3LYP-based cationic resonance state potentials have at least a 'correct' shape, but might be shifted in energy, with respect to the experimental values. Such shifts would not influence the switching dynamics, but do not allow predicting the absolute resonance energies. The energy gap to the tip Fermi level, ΔE_{res} in Eq. (2.52) therefore only enters as a parameter in the following calculations.

[7] Therefore, all ionic state energies are defined with respect to $V_{gs}(q_0)$.

[8] $-\Phi_W$ is the energy that has to be invested or is gained during the abstraction or addition of an electron from or to the metal bulk of the tip.

Chapter 3

Hydrogen on Si(100) [1]

3.1 Introduction

It has been previously mentioned in Sec. 1.1 that the hydrogen-covered on Si(100) surface was already a subject of intense studies by both theory and experiment. STM-driven DIET and DIMET processes of H and D were observed at positive bias voltages [29, 31], as well as STM-driven DIET at negative voltages [119]. Controlled desorption of hydrogen from H-passivated Si-surfaces on the nanoscale is of special interest for lithographic applications, and was achieved via STM [51] and optical excitation [120]. Subsequent theoretical models, mentioned in Sec. 1.3, studied the STM-induced, resonance-mediated desorption dynamics using wave packet techniques, open-system density matrix theory [73] and semi-classical Gaussian wave packet propagations [76, 77].

Another interesting feature of the H/D@Si(100) system is its ability to serve as a binary switch of atomic scale. More precisely, single dangling bond defects on dimers of a Si(100)(2 × 1) surface allow for the switching phenomenon. Dangling-bond sites are created via STM-induced desorption of single H-atoms from a fully H-covered surface (see below). The single H-atom remaining at the silicon-dimer can be laterally moved between two stable positions by further applying an STM current pulse, as first observed by Grey et al. [9]. Since the system was found to switch reversibly and stable at room temperature, it is a promising candidate for a memory device on a atomic scale [121].

Subsequently, detailed STM studies by Quaade et al. [122] and Stokbro et al. [32] revealed that switching only takes place at negative sample bias and has its maximum rate around $-2.7\,\mathrm{V}$ bias voltage. Furthermore, a linear dependence between tunneling current and switching rate became apparent, showing a switching yield per tunneling electron of $\approx 8 \times 10^{-8}$ at the resonance center. This finding was taken as evidence for a hole resonance-based switching mechanism. An isotope ratio of ≈ 7, between the switching yield of hydrogen and deuterium, was observed as well. A resonance lifetime $\tau_{res} \approx 2.5\,\mathrm{fs}$ was estimated via the full width at half maximum (FWHM) of a Lorentzian, fitted to the voltage dependency of the switching rate. The ratio I_r/I between the tunneling current I_r traveling through the resonance and the overall STM current I was estimated as about

1×10^{-3} in an analytical model. Further, switching was supposed to take place on the excited/resonance state surface.

As mentioned in Sec. 1.3, the 'above-threshold regime' of resonance-mediated switching, was already studied by Abe et al. [79] using open-system density matrix theory and a one-dimensional, two-surface model. While a model potential was used for the resonance surface, a plane-wave DFT-based ground state potential was used as determined by Stokbro et al. [32], both along a 1 D lateral switching coordinate. Details of the underlying switching Hamiltonian, also serving as basis for the actual dynamics simulation, are explained in the following Sec. 3.2.2. Contrary to the mechanism suggested by Stokbro et al., Abe et al. found the switching to be dominated by tunneling in the ground state. Setting the resonance lifetime to 2.53 fs, and the vibrational lifetime in the electronic ground state to $\tau^1_{vib} \approx 1\,\text{ns}$, a switching yield of 8×10^{-4} and an isotope ratio of 18 are observed, in reasonable agreement to the already mentioned experimental data. However, Abe et al. did consider the 'above-threshold', low current regime only.

In this thesis, the 'below-threshold' resonance switching regime for the H@Si system is studied instead. Here, the focus lies on the high current-regime, above 1 nA, which has not been studied experimentally so far. Here, a multiple electronic excitation mechanism might become the dominating contribution to the switching. STM-induced excitations of the hydrogen bending mode on a Si(100) surface and subsequent lateral, intra-dimer switching dynamics, are treated using a one-dimensional open-system density matrix approach. The extended 'single-surface' model of Walkup et al. [70, 71], as described in Sec. 1.3 and Sec. 2.5.3 is applied in order to simulate dipole- and below-threshold resonance switching of H on Si(100).

The chapter is organized as follows. In Sec. 3.2.2 the utilized 1 D switching Hamiltonian is introduced, followed by a discussion of the neutral ground state potential (Sec. 3.2.1) and corresponding eigenfunctions (Sec. 3.2.3). The resonance state potential, as obtained via Koopmans' theorem, is presented in Sec. 3.3.3. In Sec. 3.4 the switching rates are calculated and analyzed for thermal-, dipole- and resonance-mediated switching, including a discussion of switching mechanism and various parameter dependencies.

3.2 Ground state potential and vibrational states

Within the 'single-surface' model of IET-induced switching, the vibrational state population dynamics are simulated in the neutral ground state. Dipole and cation resonance-induced transition rates between vibrational levels of the ground state are calculated via perturbative rate equations (2.49) and (2.52). Therefore, the neutral ground state potential, its dipole function, and the cation resonance potential are needed. Additionally, some system specific parameters are of interest, i.e.m the lifetimes of vibrationally excited states as well as the lifetime of the electronically excited, resonance states.

Parameter	Value	Parameter	Value
A_0	-25.8505	C_6	2.742×10^{-1}
A_1	-2.0514	C_8	-2.726×10^{-2}
A_2	27.2304	C_{10}	1.647×10^{-3}
C_2	5.1279	C_{12}	-5.50×10^{-5}
C_4	-1.6500	C_{14}	7.5×10^{-7}

Table 3.1: Parameters for the neutral ground state potential surface for H@Si(100) according to Eq. (3.1) as published by Abe et al. [79]. All parameters are given in units of $\mathrm{E}_h \mathrm{a}_0^{-2k}$ ($k = 0,\ldots,9$).

3.2.1 Ground state potential

The ground state potential along switching coordinate x, was provided by periodic DFT calculations of Stokbro et al. [32]. An analytical fit to the ground state potential, as shown in Fig. 3.1 and provided by Abe et al. [79], has the following form:

$$V_g(x) = A_0 \ \mathrm{sech}^2\left(\frac{x}{A_1}\right) + A_2 \ \mathrm{sech}^4\left(\frac{x}{A_1}\right) + \sum_{k=1}^{7} C_{2k} \ x^{2k}; \qquad |x| \leq 6.6\mathrm{a}_0 \qquad . \tag{3.1}$$

The fit parameters as taken from Abe et al. are listed in Tab. 3.1. The minima are located at $x = \pm 3.3\,\mathrm{a}_0$ and the height of the switching barrier at $x = 0.0\,\mathrm{a}_0$ is 1.35 eV. The analytic fit of Abe et al. covers a range from $x = -6.6$ to $x = 6.6\,\mathrm{a}_0$. Here, a grid between $x = \pm 10\,\mathrm{a}_0$ is used, to calculate vibrational eigenstates via the Fourier grid Hamiltonian method (see Sec. 2.2), in order to ensure zero amplitudes at the grid boundaries, for all states up to an energy of 2.3 eV. A cutoff of 2.5 eV is chosen for the potential energy, since the experimental activation barrier of recombinative hydrogen desorption on H-saturated Si(100) surfaces is about 2.5 eV [123]. The value of 2.5 eV is taken as an asymptotic limit for our potential, extrapolating the fit of Abe et al. beyond $x = \pm 6.6\,\mathrm{a}_0$ via an exponential function,

$$V_g(x) = A_3(1 - e^{\pm A_4 \cdot x + A_5}) \qquad , \tag{3.2}$$

with the following parameters: $A_3 = 0.0918\,\mathrm{E}_h$, $A_4 = 2.475\,a_0^{-1}$, $A_5 = 14.2699$. During the extrapolation it is ensured that the potential values and their first derivatives are continuous at the connection points of both potential regions at $x = \pm 6.6\,\mathrm{a}_0$.

3.2.2 Switching Hamiltonian

The employed one-dimensional, field-free nuclear Hamiltonian $\hat{H}_0$,

$$\hat{H}_0 = -\frac{\hbar^2}{2m_H}\frac{d^2}{dx^2} + V(x) \qquad , \tag{3.3}$$

describes the lateral movement of a single hydrogen atom along the silicon-dimer axis x, as depicted on the left side of Fig. 3.1. The influence of a static electric field $\vec{E}$ is included

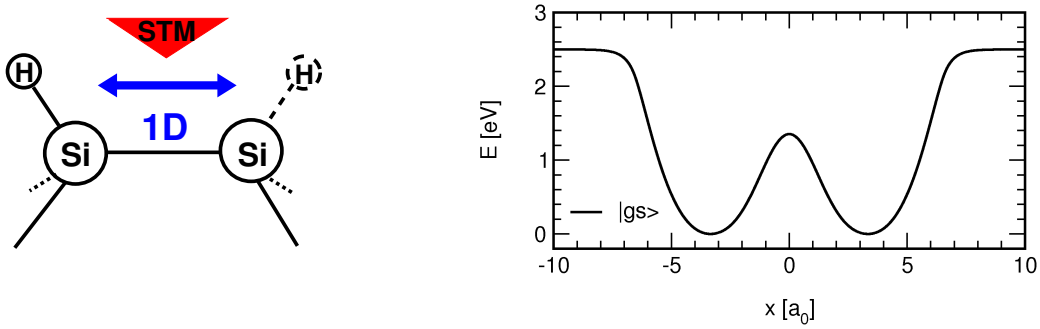

Figure 3.1: Left: Schematic depiction of a single H-atom, switchable between two lateral positions, on top of a Si(100)(2 × 1) surface-dimer. Right: The corresponding 1 D neutral ground state potential in eV, as taken from periodic DFT calculations of Stokbro et al. [32]. The underlying fit function is taken from Abe et al. [79] (see Eq. (3.1) and Tab. 3.1).

grid boundaries: x [a_0]	±10
grid points: N	1000
mass (H/D): m [m_e]	1837.36/ 3674.72
potential cutoff: [eV]	2.5

Table 3.2: FGH parameters, as used for the representation of 1 D vibrational eigenfunctions of H on Si(100) in its neutral state.

in semiclassical dipole approximation as,

$$\hat{H} = \hat{H}_0 - \mu_z E_z \quad . \tag{3.4}$$

Here, μ_z refers to the dipole component perpendicular to the surface plane, and E_z is the perpendicular field component.

3.2.3 Vibrational eigenstates of the ground state potential

The FGH method, a symmetry-adapted basis set[1] and the Hamiltonian of Eq. (3.3) are utilized in order to calculate eigenenergies $E_n^{\pm}$ and eigenfunctions $\psi_n^{\pm}$ of odd $(-)$ and even $(+)$ parity for the given potential $V(x)$ of C_s symmetry. The tunnel splitting for each doublet is calculated as,

$$\Delta E_n = E_n^- - E_n^+ \quad , \tag{3.5}$$

defining the tunneling time T_n needed for a wave packet consisting of states ψ_n^+ and ψ_n^- of a single doublet n, to tunnel through the potential barrier,

$$T_n \approx \frac{\pi\hbar}{\Delta E_n} \quad . \tag{3.6}$$

The parameters, listed in Tab. 3.2, are used to resolve 30 doublets or 60 unlocalized, bound states with energies up to 1.5 eV. Obtained energies E_n, tunnel splittings ΔE_n and tunneling times T_n are summarized in Tab. 3.3. Since the barrier height is 1.35 eV, the

[1] Details are given in theory Sec. 2.2 and Appendix A

Doublet (n)	E_n^+ (meV)	ΔE_n (meV)	T_n (ns)
0	34	$< 10^{-9}$	$> 10^6$
1	104	$< 10^{-9}$	$> 10^6$
2	176	$< 10^{-9}$	$> 10^6$
3	249	$< 10^{-9}$	$> 10^6$
3 - 7	$\cdots$	$< 10^{-9}$	$> 10^6$
8	626	8.03×10^{-9}	2.57×10^5
9	702	1.08×10^{-7}	1.91×10^4
10	778	1.32×10^{-6}	1.57×10^3
11	854	1.46×10^{-5}	141
12	930	1.48×10^{-4}	14.0
13	1004	1.38×10^{-3}	1.50
14	1078	1.17×10^{-2}	1.77×10^{-1}
15	1150	8.98×10^{-2}	2.30×10^{-2}
16	1220	6.16×10^{-1}	3.35×10^{-3}
17	1286	3.6	5.47×10^{-4}
18	1342	14.0	1.48×10^{-4}
19	1396	27.7	7.47×10^{-5}
20	1460	34.3	6.03×10^{-5}

Table 3.3: Selected eigenenergies E_n^+ for wave functions of even parity, tunnel splittings ΔE_n and tunneling times T_n for selected doublets n.

energy for the odd and even eigenstates of doublet $n = 18$ are found to be above and below the barrier, respectively. The tunneling times decrease from the μs- down to $T_n \approx 1\,\mathrm{ps}$ at the barrier top ($n \approx 18$) and decreases by another order of magnitude up to the highest doublet considered, $n = 30$.

All eigenfunctions for the symmetric double-well potential are delocalized over left (L) and right (R) wells. L/R-localized functions $\tilde{\psi}_n^{L,R}$ are needed instead for the rate expressions entering the dissipative Liouvillian in the density matrix propagation, as explained in Sec. 2.4.5. After localization, the degree of localization, as described in Sec. 2.3, is $> 99\,\%$ up to the barrier and decreases to about $82\,\%$ for doublet $n = 30$.

3.3 Vibrational transition rates $W_{f\leftarrow i}$

The switching dynamics are studied by means of open-system density matrix propagation with a dissipative super operator of Lindblad type, as explained in Sec. 2.4. System-bath couplings are subsumed in inter-state population transfer rates $W_{f\leftarrow i}$, covering interactions with the surface phonon-bath and IET-induced processes, as shown in Eq. (2.32). The corresponding rate expressions, discussed in Sec. 2.5, are applied for H@Si(100) in the following. It should be mentioned again, that for the actual problem of a symmetric double well potential all transition rates calculated for the manifold of vibrational states localized to the left potential well are identical to those calculated for states localized to the right well.

3.3.1 Vibrational relaxation and excitation rates $W_{f\leftarrow i}^{vib}$:

The lateral transfer coordinate x is a combination of Si-H stretching and H-Si-Si bending-modes. Experimental and theoretical work revealed vibrational lifetimes in the order of ns and ps for stretching- and bending-modes, respectively (see Sec. 1.3). Therefore the relaxation of the involved H-Si stretching mode is the 'bottleneck' for dissipative processes in H@Si. For the harmonic, bilinear model, as introduced in Sec. 2.5.2 used here, the vibrational lifetime parameter τ_1^{vib} is set to 1 ns throughout, if not stated otherwise. Within the bilinear harmonic relaxation model, left and right sets of localized vibrational states are treated as independent harmonic oscillator functions. Within each set, the lifetimes scale linearly and only $\Delta v = \pm 1$ transitions are allowed, as depicted in Fig. 2.2 on page 18. That is, for downward rates ($f < i$) we use for vibrational relaxation rates (see Eq. (2.39)),

$$W_{f\leftarrow i}^{vib} = i \cdot \delta_{i,f+1} \cdot (\tau_1^{vib})^{-1}, \tag{3.7}$$

as ingredient of Eq. (2.32), where τ_1^{vib} is the vibrational lifetime of the first vibrational excited state and f, i are localized states as defined earlier (see Sec. 2.5.2). Temperature-dependent 'upward'-rates are included via the condition of detailed balance, using Eq. (2.40).

3.3.2 Dipole transition rates $W^{dip}_{f\leftarrow i}$

In order to estimate the contribution of dipole-induced switching, the static dipole component $\mu_z(x)$, perpendicular to the Si-surface was calculated from a simple cluster model.

(1) Cluster model and dipole function $\mu_z(x)$:

The cluster used to calculate $\mu_z(x)$ is shown in Fig. 3.2. It consists of 9 Si-atoms and 13 H-atoms, needed to saturate the non-surface Si atoms and one Si-atom of the top silicon-dimer. The Si-dimer has a single hydrogen atom and a dangling bond, carrying a single

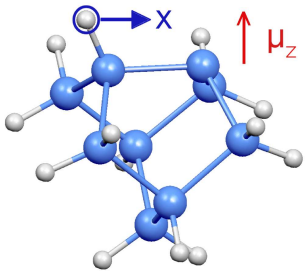

Figure 3.2: The Si_9H_{13} cluster in its neutral electronic ground state geometry. The cluster is optimized via UB3LYP/6-31G(d).

electron. Because of the resulting doublet multiplicity, the spin-unrestricted UB3LYP functional [108] is used in combination with the 6-31G(d) basis set [110] to fully optimize the cluster geometry. The minimum character is checked by the absence of imaginary frequencies. The agreement between the results of the periodic DFT calculations of Stokbro et al., in bond lengths and bond angles is better than $0.05\,a_0$ and 3°, respectively. Neutral ground state potential $V_{gs}(x)$ and dipole function $\mu_z(x)$ are calculated along the lateral H-atom switching coordinate x (see Fig. 3.2). The height of H above the Si-dimer is optimized at each point along x. The resulting position of the obtained potential minima is $0.09\,a_0$ outside the minima position, calculated by Stokbro et al. [32]. Unfortunately, the UB3LYP calculated dipole function was found to be not continuous at large Si-H bond lengths. This was addressed to difficulties of the UB3LYP functional in order to describe the Si-H bond breakage. Therefore, the CASSCF [107] method is used (see also Sec. 2.8) instead, which is more appropriate for the description of the H-Si bond breaking at 'large' values of x. The UB3LYP cluster geometry is taken for all values of x except the hydrogen z-coordinate which is re-optimized while using CASSCF(3,4)/6-31G(d). The active space consists of the two highest occupied and two lowest unoccupied Hartree-Fock orbitals [114], including three electrons for each CASSCF calculation. The calculated dipole function $\mu_z(x)$ and its analytical fit are shown in Fig. 3.3. The utilized fit function is of the following form,

$$\mu_z(x) = (D_2\cos(D_3x) + D_1x^2 + D_4x^4 + D_5x^{12})\cdot e^{D_6x^2} + D_7 \quad , \tag{3.8}$$

employing seven fit parameters, summarized in Tab. 3.4. The quality of the dipole moment was checked by DFT calculations using different basis sets, and density functionals

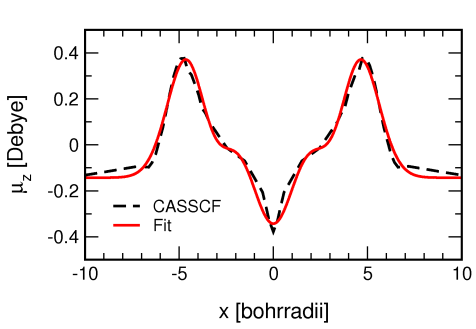

Figure 3.3: Static dipole function $\mu_z(x)$, perpendicular to the Si-surface-dimer of the Si_9H_{13}-cluster, as calculated along the switching coordinate x, using CASSCF(3,4)/6-31G(d) (red), and analytic fit (dashed, black). The height of hydrogen above the Si-surface-dimer is re-optimized at each point, while using the UB3LYP cluster geometries for all other atoms.

Parameter	Value
D_1	0.1
D_2	-0.2
D_3	0.6
D_4	-1.0×10^{-4}
D_5	1.9×10^{-6}
D_6	-0.275
D_7	-0.143

Table 3.4: Fit parameter used for the static dipole function $\mu_z(x)$ (see Fig. 3.3). D_1 is in units of Debye/$(a_0)^2$, D_2 and D_7 in Debye, D_3 $1/(a_0)$, D_4 in Debye/$(a_0)^4$, D_5 in Debye/$(a_0)^{12}$, D_6 $1/(a_0)^2$.

(PW91, [111]). Also, a larger cluster, $Si_{17}H_{21}$, with four silicon layers below the top silicon-dimer, was tested. It was found that method and basis set dependence of $\mu_z(x)$ is weak.

(2) Calculation of dipole transition rates:

Eq. (2.49) is used to estimate the inelastic tunneling current fraction of dipole-induced $1 \leftarrow 0$ vibrational transitions, $\eta^{dip}_{1\leftarrow 0}$, based on an expression derived by Persson et al. [25]. Using Eq. (2.49) a dipole-induced $1 \leftarrow 0$ transition rate $W^{dip}_{1\leftarrow 0} = 1.1 \times 10^{-10}\,(\hbar/\mathrm{E}_h)^{-1}$ was calculated, for a STM current I of 1 nA. The corresponding inelastic dipole-current fraction was $\eta_{dip} = 7.5 \times 10^{-4}$. This value fits very well to the range of 10^{-3} to 10^{-4}, published for similar surface-adsorbate systems [34, 76].

Now, Eq. (2.49) is used to calculate dipole-induced vibrational transition rates, $W^{dip}_{f\leftarrow i}$, within and between two sets of left- and right-well localized states $\tilde{\psi}_{i,f}$ for the H@Si(100) system. The resulting dipole-induced rates for i to $i+n$ ($n = 1, \ldots, 4$) transitions, within the left potential well, are plotted in Fig. 3.4. The $\Delta v = \pm 1$ rate curve dominates until $i \approx 25$ and shows a maximum in the barrier range around state $i = 18$. The decrease after the barrier is explained by the fact of a decreasing localization of the respective states. The existence of overtone transitions $\Delta v = \pm 2$, $\Delta v = \pm 3$, etc. and the non-linear behavior of the fundamental $\Delta v = \pm 1$ transition rates reflect the degree of anharmonicity of vibrational states and the non-linearity of the dipole function (see Eq. (2.50)), as already found by Walkup et al. for a similar problem [70].

Since the localization of vibrational states $\tilde{\psi}_{i,f}$ is not perfect around and above the energy level of the switching barrier, dipole-induced $L \leftrightarrow R$ transition rates are non-zero, in

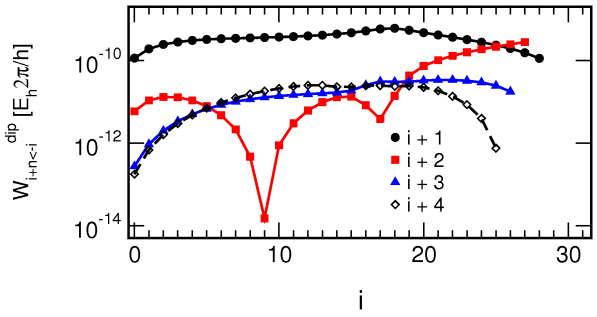

Figure 3.4: Dipole-induced transition rates $W^{dip}_{f\leftarrow i}$ between left-localized vibrational levels (i) of the H@Si(100) ground state potential. $I = 1\,\mathrm{nA}$.

principle[2]. It is found, that transitions between left- and right-localized states are not significant up to state 15, however. In the barrier region around state 18, on the other hand, the $L \leftrightarrow R$ rates are of the same order of magnitude as comparable intra-well transition rates. It is found, however, that the switching mainly results from tunneling of states which are below the region where $L \leftrightarrow R$ rate-induced switching becomes significant (see below).

3.3.3 Resonance transition rates $W^{res}_{f\leftarrow i}$

(1) Cation resonance potential surface:

The potential surface for the cation hole resonance is needed in order to derive IET-induced vibrational transition rates via Eq. (2.52). Stokbro et al. and Abe et al. utilized model potentials which were based on educated guesses [32, 79]. It is a challenging task, even for semiconductor surfaces, to calculate potential surfaces for electronically excited states. The aim of the following section is to obtain a qualitatively correct resonance surface, based on first principles and a reasonable numerical effort. Therefore, the combination of cluster calculations for the neutral state and Koopmans' theorem (see also Sec. 2.9), are applied for H@Si.

Application of Koopmans' theorem: Applying Koopmans' theorem [113] on the UB3LYP/6-31G(d) calculated energies $\epsilon^{\alpha,\beta}_{HOMO-n}(x)$ of occupied α- and β-spin orbitals, vertical ionization potentials (VIPs) are derived along x. Overall, n cation resonance state surfaces $V^{+,\alpha}_{es,n}(x)$ and $V^{+,\beta}_{es,n}(x)$, are generated applying Eq. (2.76),

$$V^{+/\alpha,\beta}_{es,n}(x) = V_{gs}(x) - V_{gs}(x_0) - \Phi_W - \epsilon^{\alpha,\beta}_{HOMO-n}(x) \quad , \tag{3.9}$$

where $V_{gs}(x)$ is the neutral ground state potential energy, normalized by the energy of its global minimum $V_{gs}(x_0)$ and $\Phi_W \approx 4.5\,\mathrm{eV}$ as the work function of the tungsten tip of the STM.

Fig. 3.5 summarizes potential surfaces obtained by Eq.(3.9), utilizing HOMO−N orbital energies of α- and β-spin orbitals. The so-called 'dangling bond state' is plotted as blue line

[2]IET related transition rates are generally calculated between all possible state combinations i, f except for $i = f$.

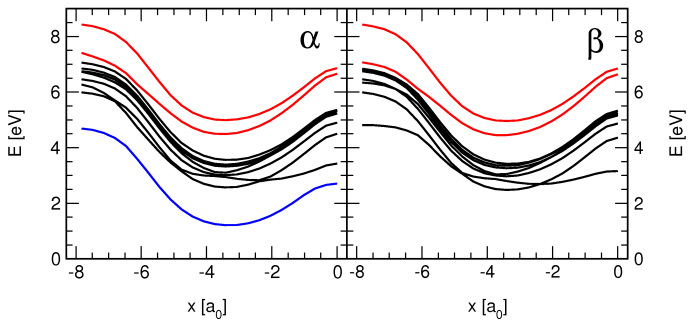

Figure 3.5: Two sets of potential surfaces $V_{es,n}^{+/\alpha,\beta}$ determined from Eq. (3.9), representing cation resonance states, as derived from occupied orbital energies of α- and β-spin and Koopmans' theorem. Orbital energies are calculated for the Si_9H_{13} cluster, at UB3LYP/6-31G(d) level of theory. The energy-zero is relative to the minimum of the neutral ground state potential.

$V_{es,0}(x)$ and shows a minimum energy of $\approx 1.2\,eV$. The dangling bond state is the lowest possible cation state of the system and results from an abstraction of the HOMO-electron, the dangling bond electron.

Periodic DFT calculations of Stokbro et al. [32], obtained the dangling bond state at 0.5 eV which is more consistent with the experimental data. Our shift of 0.7 eV is mostly related to the differences in the utilized density functional. Stokbro et al. utilized the PW91-functional of Perdew and Wang [111] instead of B3LYP used here. Also for the Si_9H_{13} cluster calculation, using UPW91/6-31G(d), a dangling bond minimum of 0.5 eV was observed (data not shown). Also, higher cation states are shifted downward by 0.7 eV for UPW91 test-calculations. However, due to convergence problems for the UPW91 functional, the UB3LYP-based surfaces had to be used.

The 'dangling bond state' is followed by a number of cation states, plotted in black and in red color, respectively, since they belong to different energy ranges (see below). The plots of the black and red set of states are approximately equal in shape for both, α- and β-spin. Further, avoided crossings are seen, connecting the lowest three black surfaces, via 'non-adiabatic couplings'. All curves show similar values for the switching barrier, except for the lowest α- and β-spin orbital derived surfaces in the black set of surfaces. Here, a smaller barrier of approximately only 0.5 eV is seen. This is of special interest, since the microscopic model of Stokbro et al. based on experimental findings, expects a lowered switching barrier in the excited state [32].

Test calculations have shown that all considered cation state surfaces are largely independent from cluster size, basis set and density functional. The applicability of Koopmans' theorem for the calculation of ionization energies from spin-unrestricted UB3LYP orbital energies was proven by Gritsenko and Baerends [124]. Furthermore, errors coming from orbital relaxation and correlation effects were found to be insignificant, as tested by Δ SCF calculations. Nuclear relaxation is neglected because of the short resonance lifetime.

Construction of the resonant surface: We will now use the obtained manifold of adiabatic Koopmans' type potential surfaces to generate an approximate, diabatic cation

resonant state potential. The composition of the final potential will be guided by three different criteria, namely energy, localization and lifetime of the resonance state as discussed in the following. The diabatic potential is needed, since the resonance will undergo multiple diabatic, electronic relaxation processes, driven by electron-phonon coupling, within the band of states on a timescale of several fs.

According to experiments the cation resonance is $\approx$ 2.7 eV above Fermi level of the tip [122]. The black colored curves in Fig. 3.5 are in a suitable energy range, whereas the red colored states are too high in energy. The 'dangling bond' state, shown in blue probably plays no role in the switching dynamics. It is certainly not the initial resonant state, due to its low energy. Further, it can not induce any vibrational excitation in the system, since its shape is too similar to the ground state potential. Also, for the pure Si(100) surface, the dangling bond state lies within the semiconductor band gap, resulting in a lifetime in the order of several ps, in contrast to the expected fs-range[3].

Periodic slab calculations of Stokbro et al. [32] gave evidence for a positive ion resonance state at 2.4 eV, localized around and below the top Si_2H layer, which is embedded in a band of other states. Fig. 3.6 shows several UB3LYP/6-31G(d) derived orbitals of the fully optimized Si_9H_{13} cluster, from the β-HOMO to the β-HOMO-6 (black colored curves in Fig. 3.5) and the α-HOMO (dangling bond state). Here, the assignment of the 'blue

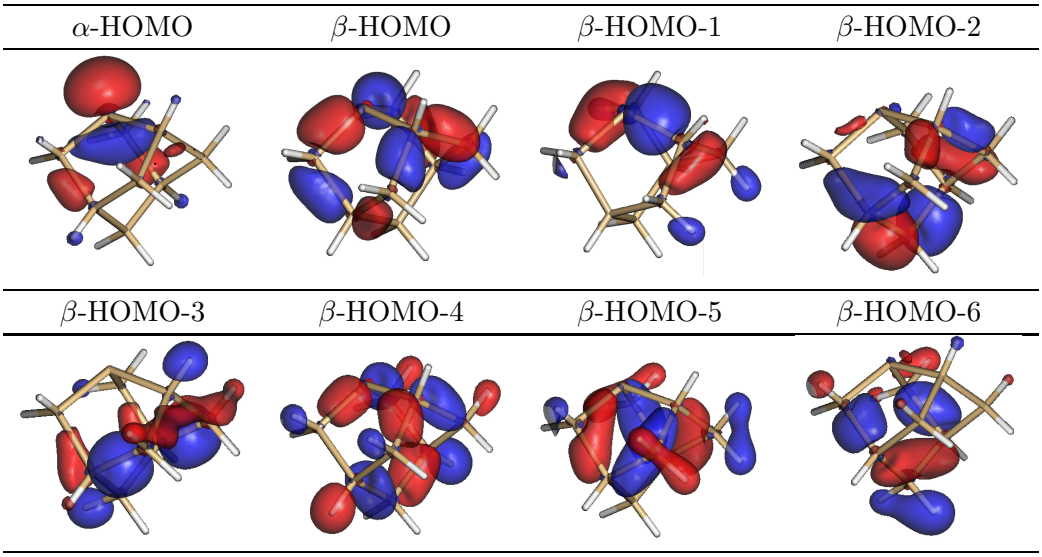

Figure 3.6: Occupied molecular orbitals of the fully optimized Si_9H_{13} silicon cluster, i.e with the H-atom in its 'right' minimum position. All calculations are done on UB3LYP/6-31G(d) level of theory.

curve' $V_{es,0}^{+/\alpha}(x)$ to the 'dangling bond state' is confirmed. It can be further seen that several of the 'black curves' show localization in the first two silicon layers, as worked out by Stokbro et al. [32].

Overall, it is found that the black set of states in Fig. 3.5 is suitable in terms of energy and orbital character for the construction of a diabatic resonance potential surface $V_{es}(x)$. For

[3]Personal communication: Prof. Martin Weinelt, Department of Physics, Freie Universität Berlin

that, we note that the adiabatic, 'black' cation states show avoided crossings, indicating a dominantly diabatic dynamic after excitation.

Because we only aim for a qualitative correct resonance surface, the accurate calculation of non-adiabatic coupling elements within the cation state manifold and a proper diabatization is not attempted here. Instead, we use a polynomial fit to interpolate between selected points and avoided crossings of the three lowest 'black', β-spin state surfaces,

$$V_{es}(x) = \sum_{i=0}^{9} a_i \cdot x^{2i} \quad , \tag{3.10}$$

in order to derive an approximate diabatic, resonance potential. This potential, as shown in Fig. 3.7, can be generated by the 10 fit parameters of Eq. (3.10) as shown in Tab. 3.5.

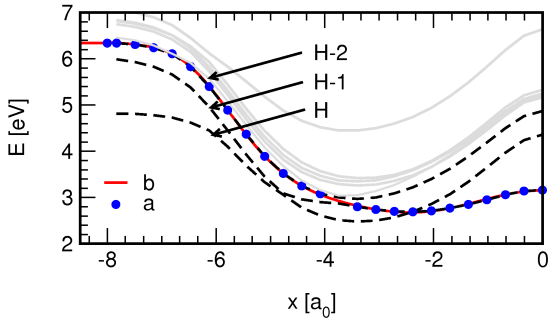

Figure 3.7: Adiabatic potential energies for $V_{es,0}^{+/\beta}$, $V_{es,1}^{+/\beta}$ and $V_{es,2}^{+/\beta}$ along the switching coordinate x (dashed lines), generated as described in the text. (b) Polynomial fit for the chosen set of points (a) of cation states, taken to generate a diabatic resonance potential. Adiabatic, cationic states at higher energies are plotted in gray.

The minimum of the diabatic state $V_{es}(x)$ is shifted by 1 Å towards the barrier, with respect

Parameter	Value	Parameter	Value
a_0	5.1297	a_5	-1.0382×10^{-4}
a_1	-0.7796	a_6	3.2018×10^{-6}
a_2	0.1737	a_7	-5.8954×10^{-8}
a_3	-0.0244	a_8	5.9464×10^{-10}
a_4	2.0537×10^{-3}	a_9	-2.5249×10^{-12}

Table 3.5: Fit parameters a_i for the diabatised excited cation state potential (Fig. 3.7), fitted via Eq. (3.10). All parameters a_i are given in E_h/a_0^{2i}.

to the neutral state $V_{gs}(x)$. A lowered barrier for the resonance surface, with respect to $V_{gs}(x)$, was expected by experiment and theory [122, 32, 79]. Since the β-HOMO-1 derived surface $V_{es,1}^{+/\beta}$ is the only one showing a substantially lowered switching barrier of 0.5 eV, it is chosen for the barrier region.

The inclusion of energetically higher cation states, like indicated in gray, or the use of another functional, basis set or cluster might result in altered cation surfaces and crossing points. Also, the usage of Koopmans' theorem itself comes with an error. Therefore, the following analysis of resonance-induced switching should be seen as a model study for the H@Si system.

(2) Calculation of resonance transition rates:

Difference potential $\mathbf{V_{es}(x) - V_{gs}(x)}$: The resulting difference potential $V_{es}(x) - V_{gs}(x)$, entering the generalized rate equation (2.52) for $W^{res}_{f\leftarrow i}$, is plotted in Fig. 3.8, along with the ground and excited state potentials $V_{gs}(x)$ and $V_{es}(x)$. Its derivative with

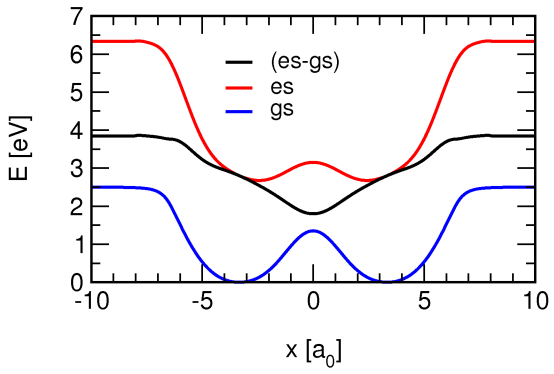

Figure 3.8: Potential curves for the lateral movement of an H-atom, along coordinate x, on top of a Si(100) surface-dimer. The ground state potential (gs) is taken from Stokbro et al. [32] and Abe et al. [79]. The cation, resonance state potential (es), is derived via Koopmans' theorem and Si_9H_{13} cluster calculations at the UB3LYP/6-31G(d) level of theory, as explained in Sec. 3.3.3. Also, the difference potential (es-gs) is plotted.

respect to x, represents an energy gradient acting on the wave packet in the resonance electronic state. In the region of the equilibrium geometries at $\pm x_0$, a nearly linear slope of $\approx 0.6\,\mathrm{eV/\AA}$, pointing towards the potential barrier is obtained for the difference potential.

Resonance rates: Now, the inelastic STM tunneling current fraction, related to resonance-induced $1 \leftarrow 0$ transitions, $\eta^{res}_{1\leftarrow 0}$, is estimated according to Eq. (2.52). The expression also depends on parameters, ΔE_{res}, the excitation energy, and $\Gamma^{\downarrow}_{el} = \hbar/\tau_{res}$, the resonance decay rate. A rate of $W^{res}_{1\leftarrow 0} = 2.7 \times 10^{-9}\,(\hbar/\mathrm{E}_h)^{-1}$, is calculated for $\Delta E_{res} = -0.5\,\mathrm{eV}$, $\tau_{res} = 2.5\,\mathrm{fs}$ and $I = 1\,\mathrm{nA}$. The corresponding value of $\eta^{res}_{1\leftarrow 0} = 1.8\times 10^{-2}$, is higher by a factor of ≈ 24 as compared to the inelastic dipole current fraction $\eta^{dip}_{1\leftarrow 0}$ and transition rate $W^{dip}_{1\leftarrow 0}$. A dominance of η^{res} over η^{dip} by approximately one order of magnitude, was also expected by Persson et al. for similar situations [26]. Fig. 3.9 depicts the dependence of the resonance-induced rate $W^{res}_{1\leftarrow 0}$, between localized vibrational states 0 and 1, calculated via Eq. (2.52), on parameters ΔE_{res} and τ_{res}. The influence of the res-

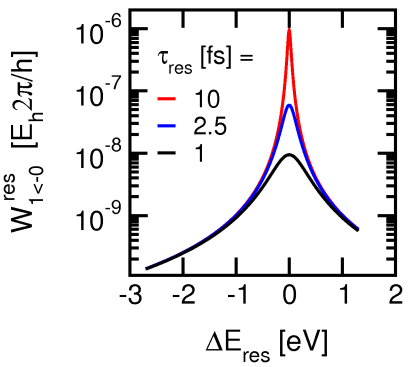

Figure 3.9: Resonance-induced transition rate $W^{res}_{1\leftarrow 0}$ between localized states 0 and 1, using Eq. (2.52), as a function of ΔE_{res} and τ_{res}, for a constant $I = 1\,\mathrm{nA}$.

onance lifetime parameter τ_{res} is most pronounced at $\Delta E_{res} = 0$ and levels off quickly as $|\Delta E_{res}|$ increases. The observed behavior results from the Lorentzian in rate Eq. (2.52),

depending on ΔE_{res} and τ_{res}. For energy differences ΔE_{res} below 1 eV, the resonance lifetime τ_{res} is not very significant at all. According to the estimate of Stokbro et al. [32], τ_{res} is fixed to 2.5 fs for all calculations.

The resonance-induced rates for transitions $i + n \leftarrow i$ $(n = 1, \ldots, 4)$, within localized states $\tilde{\psi}_n$, are shown in Fig. 3.10. The fundamental $\Delta v = \pm 1$ transition rates dominate over the whole range, by at least two orders of magnitude, as for the dipole rates. Again, the existence of overtone transitions and deviations of a linear dependence of $W_{i+1 \leftarrow i}$ with respect to i are caused by the anharmonicity of the localized vibrational states and the non-linearity of the difference potential. A comparison to the dipole-induced rates

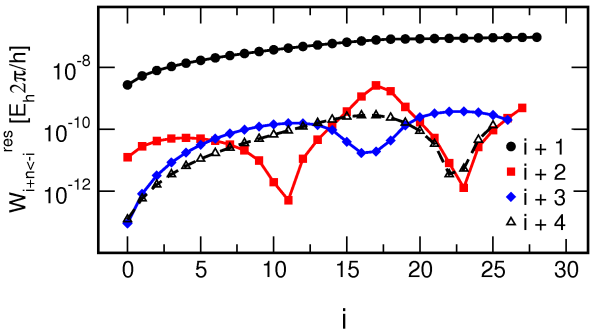

Figure 3.10: Resonance-induced transition rates, $W^{res}_{f \leftarrow i}$ between localized states $\tilde{\psi}_{i,f}$. $I = 1\,\text{nA}$, $|\Delta E_{res}| = 0.6\,\text{V}$, $\tau_{res} = 2.5\,\text{fs}$.

for transitions $i + 1 \leftarrow i$ of Fig. 3.4 shows, as expected, that the resonance rates are approximately two to three orders of magnitude larger. IET-driven vibrational excitation is therefore expected to be dominated by resonance contributions.

3.4 Density matrix propagation

In the following, the results of open-system density matrix propagations (see Sec. 2.4) for the H@Si(100) model system will be presented. The model is based on the ground state potential (Sec. 3.2.1), the harmonic, bilinear relaxation model (Sec. 3.3.1) and IET-based vibrational transition rates as introduced in Secs. 3.3.2 and 3.3.3, respectively. The section provides a systematic study of the switching mechanism based on IET-induced vibrational excitation as well as an examination of switching rate dependencies on vibrational lifetime, resonance energy, temperature, isotope mass, and electric field strength.

The equations of motion for the density matrix are solved via a Runge-Kutta integrator of fourth order (see Appendix B). The time step is set to $160\,\hbar/\text{E}_h$, the overall propagation time is $\approx 10 \times \tau_1^{vib}$ for each propagation and 60 vibrational states up to an energy of $\approx 1.5\,\text{eV}$ are included for each propagation. Each propagation starts, regardless of the actual bath-temperature, with 100 % population in the left-localized vibrational ground state.

3.4.1 Switching mechanism

The influence of IET-, thermal- and dissipative transition rates drives the system towards a quasi steady state, having a 'characteristic temperature' with regard to the population distribution. The left graph of Fig. 3.11 shows the development of selected populations of the left well, where all population was initially in the ground state. The tunnel current is set to 1 nA, the energetic difference between the resonance center and the Fermi level of the tip $|\Delta E_{res}|$ is 0.9 eV. It can be seen from the graph, that the system is approaching a quasi

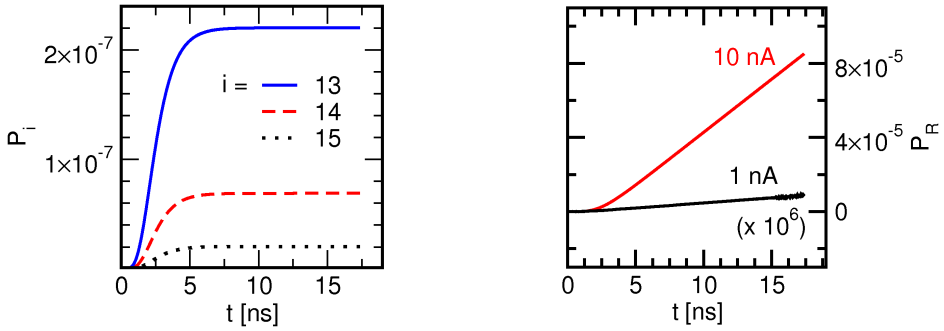

Figure 3.11: Propagation of the H@Si(100) system, starting in the left-localized vibrational ground state. $|\Delta E_{res}| = 0.9\,\text{eV}$, $\tau_1^{vib} = 1\,\text{ns}$, $I = 1\,\text{nA}$, $\tau_{res} = 2.5\,\text{fs}$. Left: P_i: Population of the left well localized states $i = 13, 14, 15$, as a function of propagation time t [ns]. Right: P_R: Population of the entire right well, as a function of propagation time t [ns].

steady state for the left well populations, shortly after the propagation has started. Such behavior was also expected by Walkup et al. [71], who studied the IET-induced transfer of Xe atoms between tip and surface using a 'characteristic temperature' model (see also Sec. 1.3). As a result, a population transfer, from the left to the right potential well sets in. The rate of population flow to the opposite well is constant, as long as the 'back-flow' to the original well is negligible. This is seen from the linear increase of the right well population P_R, plotted in the right-hand side of Fig. 3.11. In this case the switching rate R_{sw}^t is simply defined as the ratio $\Delta P_R/\Delta t$ (see also Sec. 2.7).

Current dependency: For $T = 0\,\text{K}$, the dependence of the switching rate on the tunneling current is examined in Fig. 3.12. Both dipole- and resonance-induced switching are at work. Two plots are shown, which include or exclude 'overtone-excitations', i.e. transitions other than $\Delta v = \pm 1$. If no overtone-excitations are included, all transition rates which do not obey the harmonic selection rule $\Delta v = \pm 1$ are set to zero during the propagation. The linear behavior of a double-logarithmic plot indicates a power law, $R_{sw}^t \sim I^N$. Values of $N = 7.8$ and 11.3 are obtained from the plots, including and excluding overtones, respectively. Both values point towards a multi-electron process for the switching mechanism, resembling a 'DIMET'-like switching regime (as discussed in Sec. 1.1). Here multiple excitations are necessary to arrive, via vibrational 'ladder climbing', at the barrier region of the potential. Since in order to tunnel through the

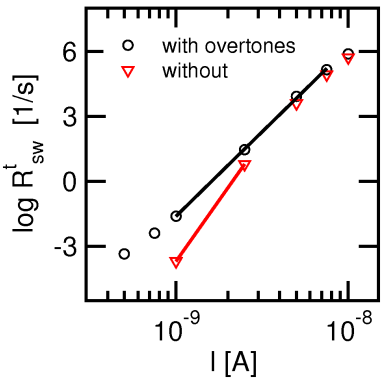

Figure 3.12: Logarithmic switching rates $logR^t_{sw}$ [1/s], for dipole- and resonance-induced switching, depending on the STM tunneling current I [A]. Switching rates are calculated under inclusion (with overtones) and exclusion (without) of transition rates $W_{f\leftarrow i}$, with $|f-i|>1$. Power law fits ($R^t_{sw}\sim I^N$) are indicated as solid lines. $|\Delta E_{res}|=0.6\,\mathrm{eV}$, $T=0\,\mathrm{K}$, $\tau_1^{vib}=1\,\mathrm{ns}$.

barrier, the population must 'reach' states with a suitable tunneling time. In order to not be suppressed by vibrational relaxation takes place on the ns-timescale, tunneling is only possible on the same or even shorter time-scales. The tunneling times T_n, given in Tab. 3.3, show that complete tunneling within a few ns is possible from state 13 onward.

First, we focus on the curve including overtones, plotted in Fig. 3.12. The slope indicates an ≈ 8 electron process for the switching. Overtone excitations must contribute, since 8 subsequent $\Delta v=+1$ transitions would end in a 'slow-tunneling' area (see Tab. 3.3). Therefore, if we neglect all transitions except $i{+}1\leftarrow i$ transitions, it can be seen in Fig. 3.12 that the slope increases to about 11.3. Therefore, the higher transitions $i+2,3,4\leftarrow i$ participate and decrease the slope of R^t_{sw} with respect to I, in the former case. The tunneling times for states 11 and 12 are about 140 ns and 14 ns, respectively, according to table 3.3. The experiment obtained a linear dependence between switching rate and tunneling current for voltages up to and above 1 V below the threshold [122, 32]. However, the actual model is studying the 'below-threshold limit' for an approximate excited state surface, dipole function and 1 D Hamiltonian. The presence of 'ladder-climbing' processes, under real conditions, can not generally be excluded. Especially at higher currents ($I>1\,\mathrm{nA}$), switching in a DIMET-like manner might become important. Currents above 1 nA are technically realizable, but it might be difficult to record the increased switching rates, since so far no experimental data are available for that current region. For the actual model, the switching rates in the regime below-1 nA-regime are too small to be numerically resolvable. Therefore, the actual model is for a 'high-current', below-threshold regime which has not been studied so far experimentally .

The role of dipole-induced switching: In order to check the influence of dipole-induced switching, compared to the purely resonance-induced one, Fig. 3.13 shows rates for pure resonance (R), pure dipole-induced switching (D) and also the combination of both (R+D). Further parameters are given in the caption. It can be seen that the dipole-induced switching rates are 3 to 6 orders of magnitude smaller than the purely resonance-induced ones. A qualitative dominance of resonance excitation was already expected from the estimates of η^{res} and η^{dip} in Sec. 3.3.3. Within the numerical accuracy of our calculation no dipole-induced switching could be observed for currents smaller than 5.0 nA. One

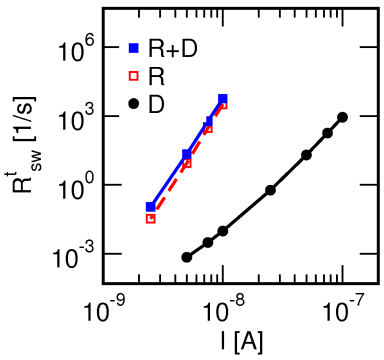

Figure 3.13: Switching rates R^t_{sw} [1/s], for pure dipole- (D), pure resonance-induced (R) switching and switching via both (R+D), in dependence on the current I [A]. $|\Delta E_{res}| = 0.9\,\text{eV}$, $\tau^{vib} = 1\,\text{ns}$, $T = 0\,\text{K}$.

could further argue that the dipole rates are negligible for the switching process. However, as both mechanisms act together (R+D), the switching rates are slightly increased with respect to pure resonance switching. The increase is much larger than expected for a simple addition of the dipole rates, pointing out a non-additive interaction between both contributions. Therefore, both excitation mechanisms are included in all following calculations.

3.4.2 Dependence on ΔE_{res}

According to the resonance rate formula (2.52), ΔE_{res} is the energy difference between the resonance energy ϵ_a and the Fermi level of the tip ϵ_F. In practice, ΔE_{res} can be tuned via the bias voltage U, as specified in Eq. (2.53). The resulting Lorentzian dependence of the fundamental transition rate $W^{res}_{f\leftarrow i}$ on ΔE_{res} was already discussed in Sec. 3.3.3. One would expect a similar behavior for the overall switching rate. The switching rates, plotted in Fig.3.14, indeed shows the expected pattern. The switching rates per electron

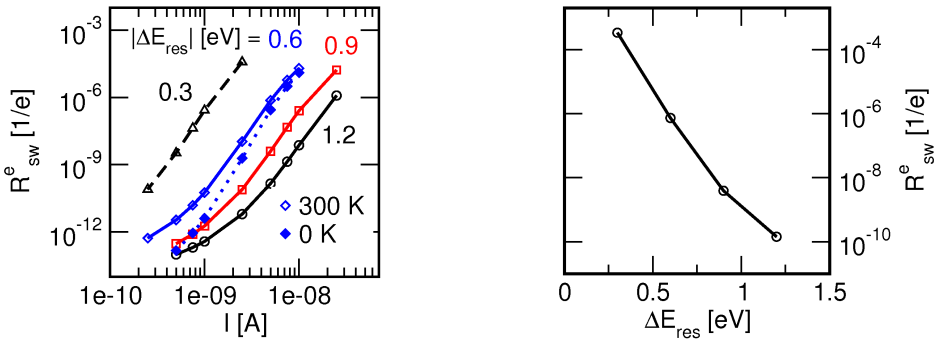

Figure 3.14: Switching rates per electron R^e_{sw} [1/e] for dipole- and resonance-induced switching of H@Si(100). $\tau^{vib} = 1\,\text{ns}$, $\tau_{res} = 2.5\,\text{fs}$, $T = 300\,\text{K}$ and $0\,\text{K}$. Left: Switching rates per electron in dependence on the STM tunneling current I A for different values of $|\Delta E_{res}|$ in eV. For $|\Delta E_{res}| = 0.6\,\text{eV}$, two rate curves are plotted for $0\,\text{K}$ (filled symbols) and $300\,\text{K}$ (empty diamonds), respectively. Right: Rates in dependence on the absolute energetic spacing between tip-Fermi level and resonance center $|\Delta E_{res}|$ eV. $I = 5\,\text{nA}$.

R^e_{sw} increase the closer the tip Fermi-level becomes to the resonance center at $-2.7\,\text{eV}$.

For $|\Delta E_{res}| > 0.6\,\text{eV}$, switching rates could not be calculated down to 0.1 nA, because of their very small values.

The higher the overtone-transition rates that are involved, the lower the power law exponent N for the current dependency ($R^t_{sw} \propto I^N$) becomes. Therefore, higher 'overtone' excitations might dominate at low currents, while lower 'overtones' or harmonic transitions dominate at higher currents. This is the reason for the lower slope in the lower current range of the plot around 0.1 nA, which is actually the upper limit of the experimental current range [122]. As stated previously, the switching rates in the low current and below-threshold region is lower by a few orders of magnitude, than the experimental value $\approx 5 \times 10^{-8}$ 1/e observed for the above-threshold limit [32].

The slope of the central section of each curve and therefore the multiple excitation character of the switching mechanism does not change, as can be seen from the plots. This finding is reasonable, since the Lorentzian only enters as multiplicative factor in the transition rate calculations, changing all calculated rates simultaneously.

Since a bath temperature of 300 K, as also used in some of the experiments, is included here, additional thermal upward rates are incorporated in the model (see Sec. 2.5.2) for $|\Delta E_{res}| = 0.6\,\text{eV}$. It is seen for the corresponding blue curves on the left side of in Fig. 3.14, that the switching rates are larger at 300 K and the slope with respect to I is decreased as compared to 0 K. The reason is that the thermally excited H-atoms don't have to 'climb' all the way 'up' via IET-induced transition rates in order to switch.

3.4.3 Vibrational lifetime dependence

In Fig. 3.15, the dependence of switching rates on the vibration lifetime parameter τ_1^{vib} is analyzed. As expected, the switching, depending on a 'ladder-climbing' process, strongly

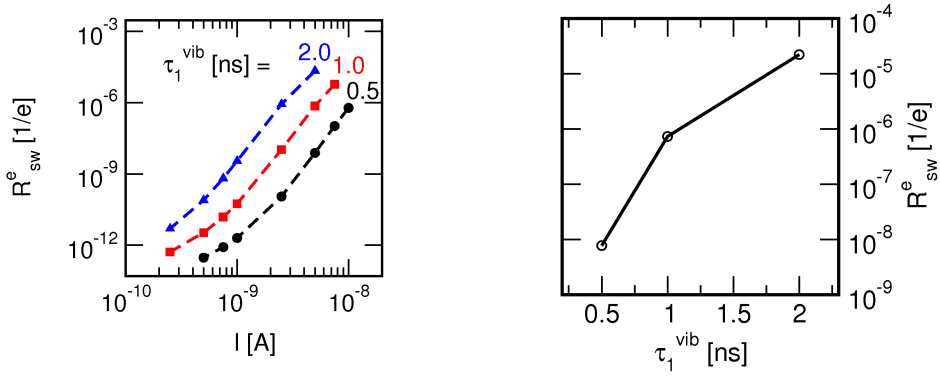

Figure 3.15: Switching rates per electron R^e_{sw} [1/e] for dipole- and resonance-induced switching of H@Si(100). $|\Delta E_{res}| = 0.6\,\text{eV}$, $\tau_{res} = 2.5\,\text{fs}$, $T = 300\,\text{K}$. Left: Rates in dependence of the STM tunneling current I for different values for the vibrational lifetime parameter τ_1^{vib} [ns]. Right: Rates in dependence of τ_1^{vib} [ns]. $I = 5\,\text{nA}$.

depends on the dissipative strength. Here, vibrational relaxation competes on every ladder

step with IET excitation processes. The slight change of τ^1_{vib} by a the factor of two alters the switching rates by two orders of magnitude. As justified in Sec. 3.3.1, a ns lifetime is chosen for the first excited vibrational state in the harmonic, bilinear limit. Since the utilized switching coordinate x is a combination of H@Si stretching- and bending-modes, the accurate lifetime is not known. For a ps lifetime, as found by Adrianov et al. for the H-Si-Si bending mode [83], the tunneling current necessary to obtain switching in the below-threshold regime and for the actual model would be on the order of μA. Therefore, DIMET-like switching processes only have to be expected for H@Si(100) if the vibrational lifetime is in the ns region and the STM current is above $\approx 1\,\mathrm{nA}$. This range clearly exceeds the range of existing STM experiments for this system. Still, a 2 D model, separately covering the dissipation for stretching and bending modes, would be desirable for the future.

3.4.4 Temperature dependence

Several studies about temperature effects on STM-driven processes in the H/D@Si(100)-system can be found in the literature. Regarding for example, the Si-H 5σ hole resonance driven H-desorption, an increase of temperature from 300 K to 610 K was found to reduce the desorption yield by several orders of magnitude. The effect was much less pronounced at bias voltages $\approx 2\,\mathrm{V}$ below the resonance center [125]. The reduction was attributed mainly to the decrease of the resonance lifetime, caused by an increased electron-phonon coupling at higher temperatures. Since the effect becomes weaker for off-resonance excitations, considered here, and an increase of switching rates at higher temperatures is seen for the H@Si(100) switch [32], such dependencies of τ_{res} on T are not included here.

Another reason for the reduced desorption yield at higher temperatures was the decrease of vibrational lifetimes for the H-Si system, also verified by theoretical studies of Andrianov et al. [83]. Here, the calculated lifetimes for H@Si bending- and stretching-modes are varied at maximum by a factor of two over a temperature range from 0 K and 600 K. According to the vibrational lifetime dependence of the actual H@Si switch, discussed in Sec. 3.4.3, a factor of two already largely affects the switching rates for the ladder climbing mechanism. However, the exact temperature dependence of the utilized lateral mode x is unknown and an inclusion of temperature effects is not possible, at that point.

An interesting aspect of the studied lateral switching of H@Si is that its switching states are stable up to temperatures of at least 400 K [32]. For the similar D@Si(100) system it was also found that the intra- and inter-dimer hopping of dangling bond defects on the surface is completely suppressed for temperatures below 500 K [126].

Starting initially from the localized vibrational ground state and setting all IET-transition rates to zero while increasing the temperature, purely temperature-induced switching is studied for H@Si within the actual model. At 400 K no switching is seen within the limits of numerical accuracy and propagation time in agreement with experiment.

Purely temperature-induced switching: At higher temperatures however, purely temperature-induced switching becomes possible, as can be seen in Fig. 3.16, where switching rates are plotted versus the lifetime parameter τ_1^{vib}. The plots show, that at 700 K and

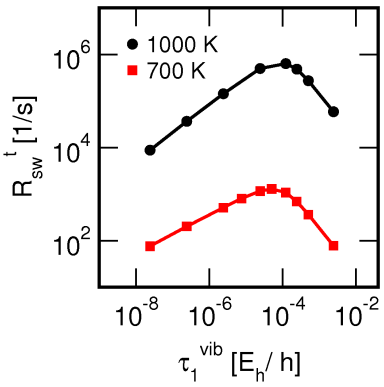

Figure 3.16: Switching rates R_{sw}^t [1/s] in dependence on vibrational lifetime of the first excited vibrational state τ_1^{vib} [$\hbar/E_h$]. Purely thermal switching was considered in this case.

1000 K thermally induced switching becomes possible. At 1000 K more population reaches the tunneling region than at 700 K. The switching rates are consequently smaller at 700 K than at 1000 K.

From the plots it is clearly seen that the calculated switching rates depend on the dissipative strength and that the rate curves show a turning point. The maximum is found for $\tau_1^{vib} = 5$ ps at 1000 K and for $\tau_1^{vib} = 2$ ps at 700 K. This effect, called 'Kramers turnover' is well known for kinetics in classical and quantum systems with friction [127]. For the limit of weak and strong dissipation, beside the maximum, the switching rates behave linearly with respect to τ_1^{vib} within our double logarithmic plot.

Also here all calculations start from an initially 100 % populated left well. For small couplings the curves in Fig. 3.16 can be rationalized as follows. The longer the vibrational lifetime τ_1^{vib}, the weaker becomes the coupling to the bath. The thermalization for the left well slows in direct relationship to the weakness of the coupling. For weak system-bath coupling, the tunneling wave packet coming from the left well is trapped at high energies, because the relaxation is slow. The population transfer from left to right well, and consequently the switching are slowed down for weak system-bath coupling.

For a system-bath coupling larger than obtained for the plot maximum, another effect hinders the switching process. The strong coupling destroys the off-diagonal elements of the density matrix, which mediate the tunneling. In a classical picture, for a hydrogen atom which gains enough energy to tunnel the barrier, the probability to be cooled down, before it is able to tunnel, becomes larger with increasing coupling strength.

Combined IET- and temperature driven switching: In Fig. 3.17 effects of increasing system temperature under inclusion of transition rates resulting from both, dipole and resonance mechanisms, are shown. $|\Delta E_{res}|$ and τ_1^{vib} are set to 0.6 eV and 1 ns, respectively. For the middle parts of all curves in the left graph a constant slope is seen, indicating a multiple-electron process. The slope is decreasing for an increasing temperature, which is

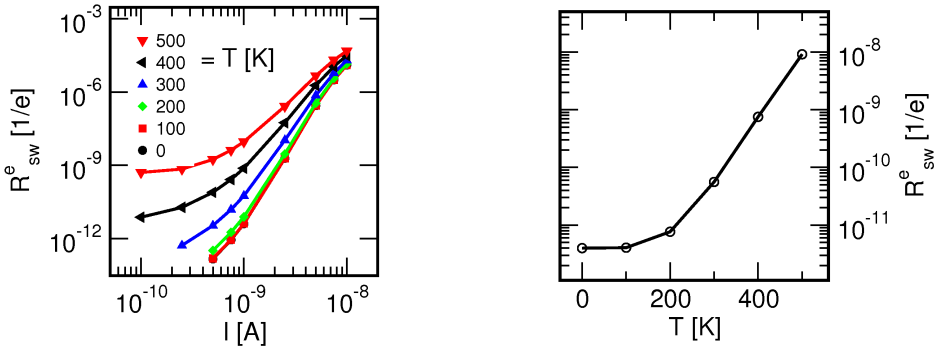

Figure 3.17: Switching rates R^e_{sw} [1/e] for dipole- and resonance-induced switching of H@Si(100). $|\Delta E_{res}| = 0.6\,\text{eV}$, $\tau_{res} = 2.5\,\text{fs}$, $\tau_1^{vib} = 1\,\text{ns}$. Left: Rates in dependence on the STM tunneling current I [A] at different temperatures T [K]. Right: Rates in dependence on temperature T [K]. $I = 1\,\text{nA}$.

explained as follows. The higher the temperature, the higher the initial state populations, and the less vibrational levels have to be passed on average by the action of tunneling electrons in order to reach a level with a sufficiently short tunneling time. Switching in the 'low current' regime, around 0.1 nA, mediated by 'overtone excitation' rates, becomes visible at higher temperatures. All curves approach the same switching rates at 10 nA, since here, the resonance rates dominate over the temperature-induced upward rates.

The right side of Fig. 3.17 depicts the temperature dependence of the switching rates per electron at a single current level of 1 nA. Below $\approx 100\,\text{K}$ a temperature independent switching regime is seen, while for temperatures above a constant slope is seen. Therefore, it is concluded that for the first part switching is purely tunneling-mediated, while for the second part thermally assisted switching takes place.

3.4.5 Isotope effect

An isotope effect for the switching on Si(100) was seen in the experiment [32]. The observed ratio of switching rates per tunneling electron, between hydrogen and deuterium (D), is about 7 around the resonance center. This value is characteristic for the single-electron process. However, here the isotope effect for a multi-electron process be will evaluated. To check for an isotope effect within our system, vibrational wave functions for D are calculated for the same ground state potential as used for H@Si previously. The higher atomic mass of D results in a higher density of vibrational states. The dimension of the density matrix is therefore increased to 90 states. $|\Delta E_{res}|$ and τ_1^{vib} are set to 0.3 eV and 1 ns, respectively, neglecting isotope effects for the vibrational lifetime. Fig. 3.18 shows the calculated switching rates per electron R^e_{sw} for H and D with respect to I. It is seen, that the atomic mass has a large influence on the rates, since tunneling through the barrier is dominating the switching process also for D. For the plotted rates, we find an increased slope for D compared to H. An increase was expected, since for D a larger number of vibrational states has to be passed, up to the tunneling region. The ratio between H and D is about 1×10^4 at $I = 0.5\,\text{nA}$ and decreases with increasing I. The decrease can be

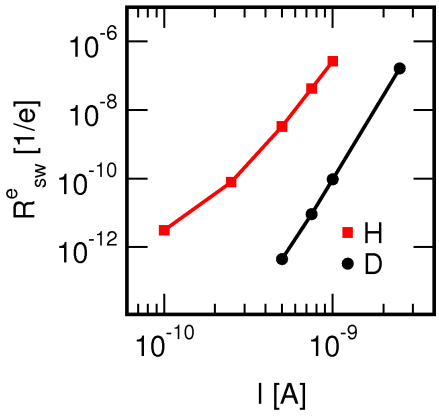

Figure 3.18: Switching rates per electron R^e_{sw} [1/e] in dependence on STM tunneling current I [A] for hydrogen (H) and deuterium (D) on Si(100). $\tau^{vib} = 1\,\text{ns}$, $|\Delta E_{res}| = 0.3\,\text{eV}$, $T = 300\,\text{K}$.

explained on the basis of a higher slope for D, with respect to I, than that observed for H.

3.4.6 Influence of a static electric field

The static electric field under the tip can influence the switching behavior, beyond dipole-induced IET. An estimate is given for the field strength E_z influencing the H-Si-adsorbate system. A common set of parameters for an STM-experiment are for example a bias voltage of $\pm 2\,\text{V}$ and tip-surface distances around 10 Å. Further, one can assume a linear decay for the electrostatic potential across a semiconductor-metal tunnel junction [19]. Therefore, the estimated field strength E_z is on the order of $0.2\,\text{V/Å}$ ($= 2\,\text{GV/m}$).

Such strong electric fields are often found to have an effect in STM experiments. Such as, field-induced diffusion of single atoms [128], bond-breaking [36], or the localization of adsorbate vibrational energies [129]. The influence of an electric field for the system under investigation is analyzed using the Hamiltonian including the field, according to Eq. (3.4), as introduced on page 34. In the right graph of Fig. 3.19, switching rates are plotted versus the current I. Since it is of interest if and how the electric field would influence the measured switching rates, T is set to 300 K, and the transition rates for dipole and resonance mechanism are included. The values of ΔE_{res} and τ_1^{vib} are unchanged.

At first sight, the rate plots look similar to those obtained for the temperature dependence in Fig. 3.17. At very large field strengths of -0.6 and $-1.0\,\text{V/Å}$, the switching process is strongly enhanced. Similar to the effect of temperature, the slope in the rate plots is slightly lowered. In contrast to the behavior for an increased temperature, the rate plots for different field strengths do not converge. This is not because the population distribution is changed, such as for an increased temperature, but rather because the tunnel splittings and tunneling times are altered. The dipole function, plotted in Fig. 3.3, shows a pronounced minimum around the region of the switching barrier. An electric field with a negative sign lowers the barrier, according to Eq. (3.4). It therefore reduces the number of vibrational levels between vibrational ground state and tunneling region, and finally enhances the switching. Since no considerable changes are seen at typical

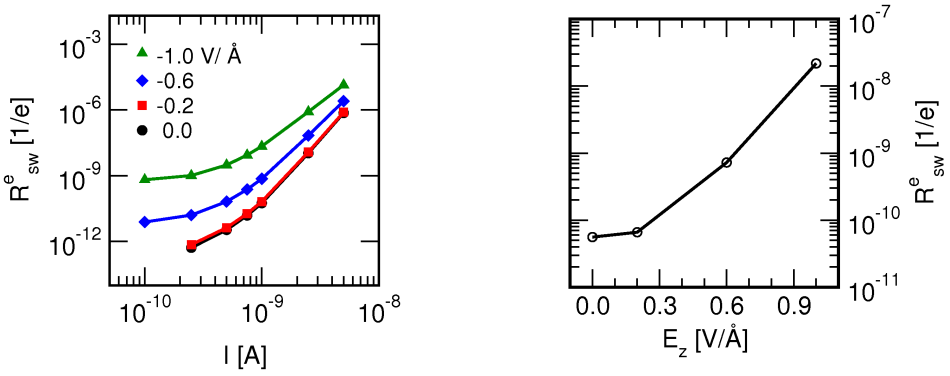

Figure 3.19: Switching rates per electron R^e_{sw} [1/e] for dipole- and resonance-induced switching of H@Si(100). $|\Delta E_{res} = 0.6|$ eV, $\tau_{res} = 2.5$ fs, $\tau_1^{vib} = 1$ ns. Left: Rates in dependence on the STM tunneling current I [A] at different absolute field strengths E_z [V/Å]. Right: Rates in dependence on the absolute field strength E_z [V/Å]. $I = 1$ nA, $T = 300$ K.

field strengths around -0.2 V/Å, field enhanced switching plays no role for the multiple-electron switching of the actual system. Purely field-induced switching was ruled out by experimentalists [32] and is not observed here, within the range of tested field strengths.

3.5 Summary

A theoretical study of the STM-induced lateral switching dynamics of single H-atoms on top of a Si(100) surface-dimer, as experimentally observed by Grey et al. and Quaade et al. [9, 122], was the purpose of this chapter. Provided that one can distinguish clearly between the two states of the switch, the system allows for the storage of binary data in atomic dimensions. Furthermore, the information is stable at room temperature [121].

A 1 D Hamiltonian was set up and vibrational eigenstates were calculated for the ground state potential, adopted from slab calculations of Stokbro et al. [32]. The hole resonance state surface, for which only model potentials were published so far, was approximated via Koopmans' theorem and cluster calculations using a Si_9H_{13} model cluster. A diabatic resonance potential surface was constructed from a set of adiabatic, cationic states, following 'avoided crossings' within the set. The vibrational dynamics was modeled within the framework of open-system density matrix theory. Transition rate expressions, treating the coupling to the surface phonon-bath and inelastic scattering events with incident STM electrons, were applied to two sets of vibrational states, localized either on the left or right side of the double-well potential. All rate expressions are based on first order perturbation theory and vibrational dissipation was treated within a 'harmonic, bilinear' coupling limit. The one-dimensional switching coordinate is a mixture of H@Si stretching and bending mode. Therefore, its exact vibrational lifetime is unclear. Thus, it is an interesting task for the future to establish a 2 D model, separately treating the H-Si stretching- and bending-modes. Further, the dissipative relaxation model could be extended towards a treatment of two-phonon relaxation processes, as found to be important for the H@Si

system [83].

A 'multi-electron' switching mechanism, based on a 'ladder climbing' and subsequent tunneling through the barrier was identified for the H@Si(100) system in the actual model. In contrast, a single-electron mechanism for switching was proposed by experiment, however, for a low-current regime. A 'ladder-climbing' mechanism might naturally dominate over 'single-electron' processes at higher currents, which was studied here. At this stage, a detailed comparison between theory and experiment is not useful. It must also be said that the resonance state as used here, is based on ab initio information, but still of model character. Also, the resonance lifetime has experimental uncertainties.

Resonance-surface independent features, such as field- and temperature-effects, were studied as well. Here, the findings were in agreement with experiment regarding the temperature stability up to 400 K and the negligible contribution of purely field-induced switching [32].

A theoretical model for IET-induced switching in a double well potential surface was established. The localization and vibrational relaxation scheme for the ground state can easily be extended to a second electronic surface. A similar model will be used for a related problem, namely the STM-induced bi-conformational switching of cyclooctadiene (COD) on Si(100), in the following chapter.

Chapter 4

Cycloocatdiene on Si(100) [2, 3, 4]

4.1 Introduction

Ultrathin organic layers on silicon surfaces have been investigated for possible applications in the fields of sensor- and display-techniques, molecular electronics and nanolithography [130]. Adsorption on silicon layers is of special interest, since it would allow for a rapid integration into the existing silicon-based technology of microelectronics. A quote from a review article covering organic adsorbates on silicon states [131]:

Although no one can foretell where successful applications will be found, it seems likely that organic molecules with their myriad and tunable properties, including size, shape, absorption spectrum, flexibility, chemical affinity, and conductivity, will create new functional possibilities.

As a consequence, in addition to the large number of STM experiments on Si(100), utilizing inorganic adsorbates (see Chap. 1), another focus is on organic admolecules. For example experiments regarding conductance of styrene and cyclopentene molecules [17], STM-induced rotation of bi-phenyl molecules [132, 47], conformational changes of stilbene [133] and the desorption of benzene [134], all on the Si(100) surface, can be found in the literature. For the last example, a comprehensive dynamical study was presented by Alavi et al. [135, 136].

A further class of organic molecules on Si(100), examined via STM, are unsaturated cyclic hydrocarbons like cyclopentene, 1,5-cyclooctadiene and 1,5-cyclohexadiene [137, 138]. The dangling-bond electrons at Si(100) surface-dimers allow a coupling to π-bonds of unsaturated hydrocarbons. Depending on the existence of either an isolated or conjugated π-system in the admolecules, the coupling reaction can be formally classified as $[2+2]$ or $[2+4]$ cycloaddition. 1,5-cyclooctadiene (see Fig. 4.1) contains two isolated double bonds. They are expected to bind to the Si(100)(2×1) surface via $[2+2]$ cycloaddition. According to the Woodward-Hoffmann rules [139], such a reaction is symmetry forbidden for the electronic ground state. In contrast, the COD adsorption reaction on Si(100) is found to be very rapid, without the need for any photo-excitation. This can be explained by an ionic

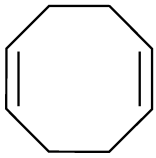

Figure 4.1: 1,5-cyclooctadiene (COD)

electronic configuration of Si(100) dangling-bond electrons (see Sec. 1.2). They allow for a nucleophilic attack, rather than a concerted $[2+2]$ cycloaddition [140, 67]. The actual adsorbate geometry of COD on Si(100) was an issue of controversial discussion. Based on STM images, Fourier-transform infrared- (FTIR) and X-ray photoelectron-spectroscopy (XPS), Hovis et al. [141] proposed an adsorption geometry in which only one of the two COD double bonds reacted with the surface. COD was thought to stand *upright* on the surface. XPS and FTIR measurements of Jolly et al. [142] further supported this interpretation. Here, the surface π states were found to be quenched. Further, the existence of unreacted COD double bonds was proven. In contrast, the STM images of Hovis et al. were interpreted as a *bridge-like* structure by Wolkow et al. [131]. For the bridge structure, both double bonds couple to two adjacent silicon-dimers. A picture of such a bridged COD-silicon cluster model is shown in Fig. 4.2 [143]. Periodic DFT results of Cho

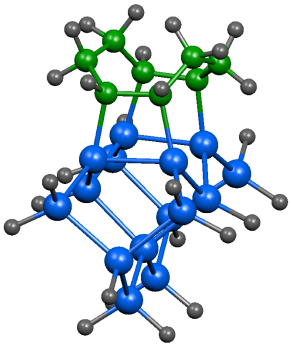

Figure 4.2: COD on a $Si_{15}H_{16}$ cluster in its global minimum. All atom positions are fully optimized, except the lowest two silicon atoms which were kept frozen in the position of the optimized cluster without COD. All calculations were done at B3LYP/6-31G(d) level of theory, by Dokić et al. [143].

et al. [144] supported Wolkow's interpretation, predicting a stabilization of 0.88 eV for the bridge relative to the upright structure. Their simulated STM images were in agreement to the original pictures [137]. Further the STM images, taken by Nacci et al. [10], showed that both bridge and upright structures existed at the surface simultaneously when $\approx 3\,\%$ of the surface-dimers were covered by COD. The bridge structure was found to be prevalent and located between two adjacent silicon-dimers in agreement with the DFT study of Cho et al. [144].

The most recent STM-based experiments for COD on Si(100) were published by Nacci et al. [10, 145]. The experiments were carried out at 7 K on n-type, As-doped silicon. Time-resolved recording of the STM tunnel current revealed random telegraph noise for a fixed tip position above chemisorbed COD admolecules. The finding was interpreted as a result of a reversible, bistable conformational switching process of COD, without any bond breaking or re-bonding events. A high-to-low current level ratio of 1.2 : 1 is found by

experiment, indicating two comparably stable switch positions [10]. The statistical analysis showed basically equal mean residence times for both states of the switch. This was interpreted as the switching between two degenerated conformational molecular positions. Furthermore the linear current dependence showed that the switching was triggered by an inelastic single-electron process (IET). A power law fit, for the current dependence of the observed switching rates, $R_{sw}^{t} \sim I^{N}$, resulted in an exponent N of 1.07 ± 0.03. The quantum yield per tunneling electron was measured as 1×10^{-9} 1/e [10, 145]. Further, no voltage dependence of the switching rate is seen for COD@Si(100) in the range between -2.5 and $+2.5$ V [10]. The upright structure also showed telegraph noise under the STM tip and an increased switching yield of 5×10^{-8} compared to the bridge structure. The upright structure has in general a more complex switching behavior because of its more flexible degrees of freedom at the surface and its dynamics are not part of the actual thesis. Instead we will focus on the bridge-structure of COD@Si only.

4.2 Potential- and dipole surfaces

4.2.1 Neutral ground state potential

The potential surface for the bi-conformational switching of COD@Si(100) in its bridge-structure was calculated by Dokić et al. [143]. The neutral ground state potential, shown in Fig. 4.3 (a) was calculated at the B3LYP/6-31G(d) level of theory, as implemented in the Gaussian03 program suite [112]. The two lowest silicon layers, out of four, were kept frozen during the calculation of the potential surface, while all other atom positions were fully optimized during the potential energy surface (PES) calculation. The torsional movement of both COD-$(CH_2)_2$ groups was represented via dihedral angels, ϕ_l and ϕ_r, between carbon atoms (a,b,c,d) on the left and right side of the COD@Si scheme in Fig. 4.5. The potential surface was determined at 19×19 points, using a step size of $10\,^\circ$ between $\phi_l = \pm 90\,^\circ$ and $\phi_r = 0 \pm 90\,^\circ$. The resulting surface is further processed as explained in the following.

Intermediate data points are obtained by cubic spline interpolation [146]. At the grid boundaries, the potential is extrapolated quadratically. The extrapolated value at grid point $i+1$ builds on the first and second derivatives of the potential surface at the last known grid point i,

$$V(\phi_{i+1}) = V(\phi_i) + V'(\phi_i) \cdot \Delta\phi + 0.5 \cdot V'(\phi_i) \cdot (\Delta\phi)^2 \qquad , \tag{4.1}$$

where $\Delta\phi = \phi_{i+1} - \phi_i$ is the distance between adjacent grid points. Since C_{2v} symmetry is expected for the final surface, the calculated data set V is symmetrized,

$$\begin{aligned} V^{sym}(\phi_l, \phi_r) = [&V(\phi_l, \phi_r) + V(-\phi_l, \phi_r) \\ &+ V(\phi_l, -\phi_r) + V(-\phi_l, -\phi_r)]/4 \qquad . \end{aligned} \tag{4.2}$$

Therefore, the resulting potential surface, shown in Fig. 4.3 (a), perfectly reflects C_{2v} symmetry. The surface consists of two symmetry equivalent minima positions (Mi) and

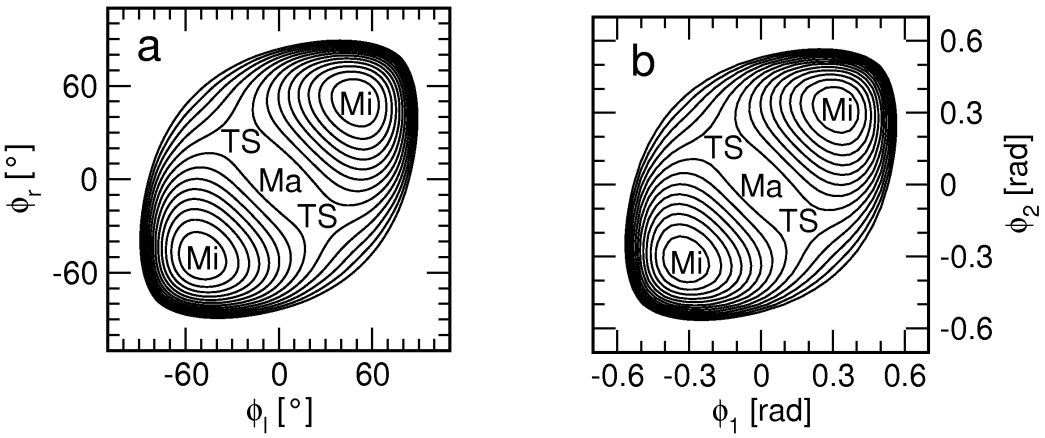

Figure 4.3: (a): Symmetrized neutral ground state potential, calculated for COD@$Si_{15}H_{16}$, along dihedral angles ϕ_l and ϕ_r. The surface was calculated by Dokić et al. at the B3LYP/6-31G(d) level of theory [143]. The utilized $Si_{15}H_{16}$ cluster is shown in Fig. 4.2. (b): Transformed surface, using angles ϕ_1 and ϕ_2 instead. (Further details are given in the text). (a/b): The maximum ($\phi_{l/r} = \phi_{1/2} = 0$) is set to 0 eV. Isolines are separated by 20 meV, starting from the potential minima. For a clear presentation, the energy cutoff is set to 0.26 eV. Mi - minimum, TS - transition state, Ma - 2nd order maximum.

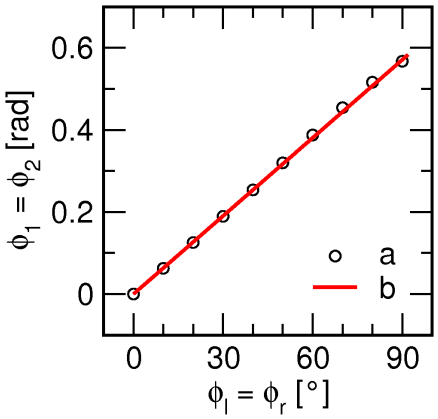

Figure 4.4: Two different definitions of angles for $(CH_2)_2$ group torsion of COD on Si(100). ϕ_l, ϕ_r: Dihedral angles between COD atoms a, b, c and d on both sides (see Fig. 4.5). ϕ_1, ϕ_2: Angles between vectors connecting atoms pairs a,d and b,c on both sides. (a) Relation between ϕ_l, ϕ_r [°] and ϕ_1, ϕ_2 [rad]. (b) Linear relation: $\phi_1 = (\pi \cdot \phi_l/180°)/2.75$.

transition states (TS). A maximum (Ma) of second order is located in the potential center. TS- and Ma-character were proven by normal mode analysis for the corresponding TS- or Ma-geometry by Dokić et al. [143]. One and two imaginary frequencies were obtained for TS- and Ma-geometry, respectively, beside the imaginary frequencies caused by the fixation of the two lower Si-layers. The minima are located at $(50°, 50°)$ and $(-50°, -50°)$, respectively. The barriers are rather shallow with 0.170 eV for the TS at $(\pm 30°, \pm 30°)$ and 0.179 eV for the Maximum $(0°, 0°)$. It is shown in Fig. 4.4 that a simple linear relationship is sufficient to map the calculated surface along the dihedrals ϕ_l and ϕ_r into the new surface defined via two angles ϕ_1 and ϕ_2 which are shown in Fig. 4.5. Using the linear equations,

$$\phi_1 = \frac{\pi \cdot \phi_l}{180°} \cdot \frac{1}{2.75} \qquad \text{and} \qquad \phi_2 = \frac{\pi \cdot \phi_r}{180°} \cdot \frac{1}{2.75} \quad , \tag{4.3}$$

the transformation from the angles ϕ_l and ϕ_r to angles ϕ_1 and ϕ_2 is achieved. The resulting, transformed potential surface, along ϕ_1 and ϕ_2, is shown in Fig. 4.3 (b). The surface extends between ± 0.57 rad for both angles.

4.2.2 Switching Hamiltonian

To simulate the switching dynamics observed by experiment, a two-dimensional Hamiltonian is set up, as will be explained in the following. Our Hamiltonian $\hat{H}$ describes the

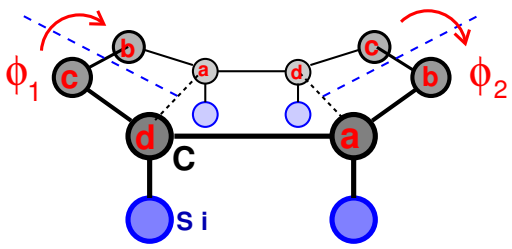

Figure 4.5: Schematic representation of the COD C-skeleton (black) on two Si(100) surface-dimers (blue). H-atoms are not shown for clarity. ϕ_1 and ϕ_2 denote the rotational angles of both CH_2 groups (b,c), rotating along the blue dashed axis, which pass the midpoints between atom pairs (ad) and (bc) on each side of the adsorbed COD.

rotational motion for the two $(CH_2)_2$ groups of the adsorbed COD molecule, which are not bound to the silicon surface (see Fig. 4.5). Also the corresponding rotation angles ϕ_1 and ϕ_2 are depicted in this schematic representation of COD@Si in Fig. 4.5. Both rotational axes are defined via the midpoints between two pairs of carbon atoms, as shown in the figure. The moment of inertia for the rotation of each respective $(CH_2)_2$ unit is,

$$I = 2m_{CH_2}(\frac{d_{CH_2-CH_2}}{2})^2 = 109476.09\,\mathrm{m_e a_0^2} \quad . \tag{4.4}$$

Mass m_{CH_2} and distance $d_{CH_2-CH_2}$ are set to 25520.439 m_e and 2.93 a_0, respectively, where m_e is the electron mass and a_0 the Bohr radius. Alternatively, collective coordinates ϕ_s, ϕ_u will be used in the following. ϕ_s is the 'center of mass coordinate', describing the C_2 symmetry preserving, opposite motion of both CH_2 groups. It is defined as,

$$\phi_s = \frac{\phi_1 + \phi_2}{2} \quad . \tag{4.5}$$

ϕ_u represents the relative motion between both rotors via,

$$\phi_u = \phi_1 - \phi_2 \quad . \tag{4.6}$$

The use of collective coordinates, as introduced for the switching Hamiltonian in Sec. 4.2.2, allows for a separate, one- or two-dimensional representation of the COD switching dynamics. The final, two-dimensional potential surface in collective coordinates is shown in Fig. 4.6. Minima positions and barrier heights are summarized in Tab. 4.1. For the sake of clarity, the potential is only plotted up to an energy of ≈ 0.3 eV. The borders for the calculated potential are ± 0.57 rad for ϕ_s and ± 1.14 rad along ϕ_u. A cutoff energy of 1.27 eV and grid boundaries of ± 0.8 rad for ϕ_s and ± 1.6 rad for ϕ_u are chosen for the calculation of vibrational eigenstates.

The corresponding moments of inertia in our collective coordinate system can be derived as $I_u = 0.5I$ and $I_s = 2I$ [143]. Using the quantum operator for the angular momentum,

$$\hat{l} = \frac{\hbar}{i}\frac{d}{d\phi}, \tag{4.7}$$

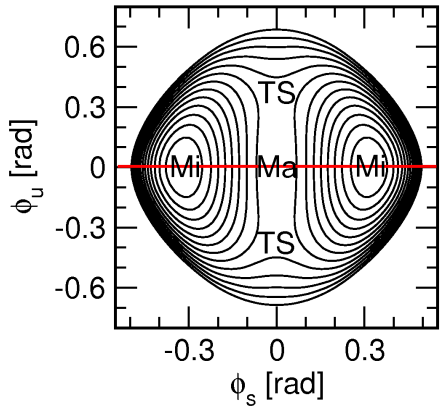

Figure 4.6: Potential surface for COD on Si(100) in its neutral ground state, along collective switching coordinates ϕ_s [rad] and ϕ_u [rad]. Original data are taken from B3LYP/6-31G(d) cluster calculations by Dokić et al. [143]. The maximum ($\phi_{s/u} = 0$) is set to 0 eV. The isolines are separated by 20 meV, starting from the potential minima. For a clear presentation, the energy cutoff is set to 0.26 eV. Mi - minimum, TS - transition state, Ma - 2nd order maximum. **Red line**: 1 D switching coordinate along ϕ_s.

the Hamilton operator is derived from the classical Hamilton function as

$$\hat{H} = -\frac{\hbar^2}{2I_u}\frac{\partial^2}{\partial\phi_u^2} - \frac{\hbar^2}{2I_s}\frac{\partial^2}{\partial\phi_s^2} + V(\phi_u, \phi_s) \quad . \tag{4.8}$$

The two modes, ϕ_s and ϕ_u, are coupled by the potential but not by the kinetic energy operator. As mentioned before, this two-dimensional problem can easily be divided into two one-dimensional parts using collective coordinates. ϕ_u in Eq. (4.6) stays at zero if the changes in ϕ_1 and ϕ_2 are equal in amount and sign. This describes a symmetric, collective rotation of the two (CH_2)-dimers. The motion is symmetric, i.e the C_2 rotational axis, perpendicular to the cluster surface and pointing through the cluster-center, is preserved. The second dimension, namely the coordinate ϕ_u allows the system to break the C_2 symmetry. The one-dimensional field-free Hamiltonian for the symmetric motion is written as,

$$\hat{H} = -\frac{\hbar^2}{2I_s}\frac{d^2}{d\phi_s^2} + V(\phi_u = 0, \phi_s) \quad . \tag{4.9}$$

4.2.3 Resonant state potential surfaces

In order to describe the dynamics induced by inelastic electronic excitations, the relevant resonance state potential surfaces are required. In the following, an anion and a cation resonance potential surface are introduced for the COD@Si system. Anion and cation surfaces were calculated on the basis of orbital energies of HOMO and LUMO, respectively, applying Koopmans' theorem on the B3LYP/6-31G(d) level. [143] (see Sec. 4.2.1).

Within the single-surface rate model (see Sec. 2.5.3), the potential energy differences between excited state and ground state are needed for the calculation of resonant IET rates. Fig. 4.7 shows contour plots of anion and cation resonance states. The isolines are separated by 20 meV. The grid borders are the same as for the neutral surface.

Minima positions and barrier heights for the resulting resonance and neutral surfaces are summarized in Tab. 4.1. It can be seen from the different minima positions and barrier heights that the anion state geometry differs more from the neutral ground state, in comparison to the cation. Still, the overall differences are rather small and a shallow switching barrier of ≈ 0.2 eV is found for both resonance surfaces.

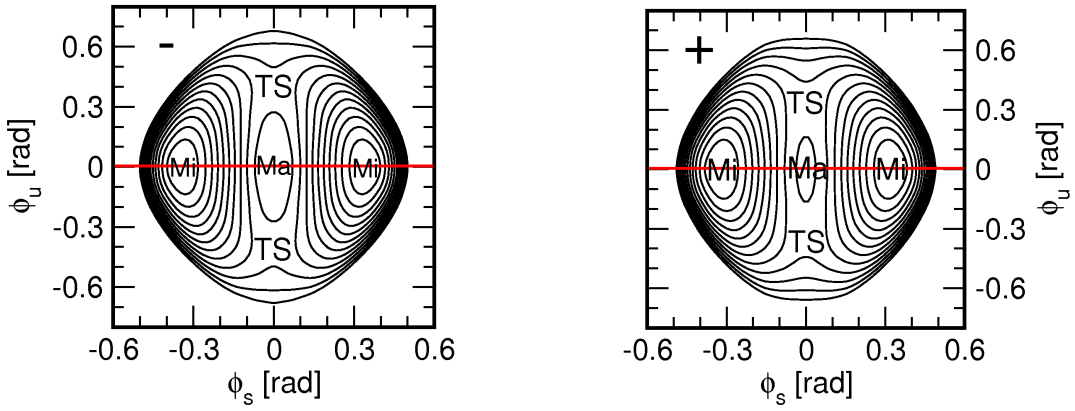

Figure 4.7: Anion (-) and cation (+) potential surface of COD on Si(100), along collective switching coordinates ϕ_s [rad] and ϕ_u [rad], as derived via Koopmans' theorem (Eq. (2.76)) and LUMO/HOMO energies, based on B3LYP/6-31G(d) cluster calculations by Dokić et al. [143]. The isolines are separated by 20 meV, starting from the potential minima. For a clear presentation, the energy cutoff is set to 2.4 eV. Mi - minimum, TS - transition state, Ma - 2nd order maximum. **Red line**: 1 D switching coordinate along ϕ_s. Details of the potential calculation are given in the text.

ΔE [meV]			
	Neutral	Anion	Cation
Ma	179	220	185
TS	170	195	173
$\phi_{s/u}$ [rad]			
Mi	$\pm$0.321	$\pm$0.348	$\pm$0.324
TS	$\pm$0.309	$\pm$0.392	$\pm$0.325
$\Delta V^{\pm,0}$ [eV]			
	0.0	3.22	1.59

Table 4.1: Energies and coordinates of stationary points on the potential surfaces of neutral, anion and cation electronic states of COD@Si(100) (see Fig. 4.6 and 4.7). ΔE: Barrier heights of transition states (TS) and 2nd order maxima (Ma) in meV. $\phi_{s/u}$: coordinates of minima (Mi), TS and Ma in rad. $\Delta V^{\pm,0}$: Vertical energy gap between resonant and neutral surface at the global minimum of the neutral potential in eV (see Eq. (4.10)).

All three 2 D potential surfaces were analyzed via normal mode analysis (see Appendix C). It was shown that the transformed and interpolated surfaces still share the characteristics of the surfaces originally calculated by Dokić et al. [143]. Furthermore, the normal mode vectors were found to be perfectly parallel to the collective coordinate system axes, confirming their separability, as assumed for the Hamiltonian utilized in Eq. (4.8).

The energetic positions of HOMO and LUMO, relative to the Fermi level of the STM tip, are unfortunately not directly accessible via Koopmans' theorem and B3LYP/6-31G(d) orbital energies of the COD@$Si_{15}H_{16}$ cluster.

The vertical energy gaps at the position of the neutral ground state minimum $\Delta V^{\pm,0} = \Delta V^{\pm}(\phi_s = 0.321\,\text{rad}, \phi_u = 0\,\text{rad})$ between anion $(-)$ and cation $(+)$ resonant surfaces $V_{es}^{\pm,0}$ and neutral surface V_{gs}^{0} are defined via Eq. (2.76) as,

$$\begin{aligned} \Delta V^{+,0} &= V_{es}^{+,0} - V_{gs}^{0} = -\Phi_w - \epsilon_H^0 - V_{gs}^0 \qquad \text{and} \\ \Delta V^{-,0} &= V_{es}^{-,0} - V_{gs}^{0} = +\Phi_w + \epsilon_L^0 - V_{gs}^0 \qquad , \end{aligned} \tag{4.10}$$

where V_{gs}^0, $V_{es}^{\pm,0}$ and $\epsilon_{L/H}^0$ are the ground state energy, the excited state energy and the HOMO/LUMO orbital energies at the minimum position $(\phi_s = 0.321\,\text{rad}, \phi_u = 0\,\text{rad})$, respectively. Φ_w is the work function the tungsten STM tip and is set to 4.5 eV. The resulting values[1] for $\Delta V^{\pm,0}$ are given in Tab. 4.1.

In the following, the below-threshold model of resonant switching of COD@Si is called single-surface (1 S) model. As for the H@Si, the energetic spacing between Fermi level of the STM tip and the resonance center enters as adjustable parameter, ΔE_{res}. In contrast to H@Si, a two-surface (2 S) approach is also used which allows for a detailed propagation of the electronically excited wave packet on the resonant surface. For the latter, perfect resonance conditions are assumed ($\Delta E_{res} \approx 0$).

4.2.4 Dipole surface

The dipole component μ_z, perpendicular to the surface, is used for a calculation of dipole-induced vibrational excitation rates, as discussed in Sec. 2.5.3. The dipole surface is calculated at the same set of points along ϕ_l and ϕ_r as the potential surfaces, except that only 17×17 points between $-80°$ and $80°$ are used here. An interpolation via cubic splines is done for the final set of calculated points. Beyond, the surface is extrapolated using the outermost calculated dipole value as a constant, since such a constant element does not influence the dipole coupling matrix elements. The direct quantum chemical calculation of μ_z in the extrapolated area leads to unphysical dipole functions and is therefore avoided. The resulting discontinuity at the junction between interpolated and extrapolated values is circumvented by using an analytical, two-dimensional fit in collective coordinates for the entire surface. Symmetrization and transformation into collective coordinates, as described for the ground state potential in Sec. 4.2, are performed beforehand. Fit function and parameters are listed in Appendix D. Fig. 4.8 shows the fitted dipole function for the

[1] $\epsilon_H^0 \approx -6.09\,\text{eV}$, $\epsilon_L^0 \approx -1.28\,\text{eV}$ as calculated by Dokić et al. [143], $V_{gs}^0 = 0\,\text{eV}$ (by choice).

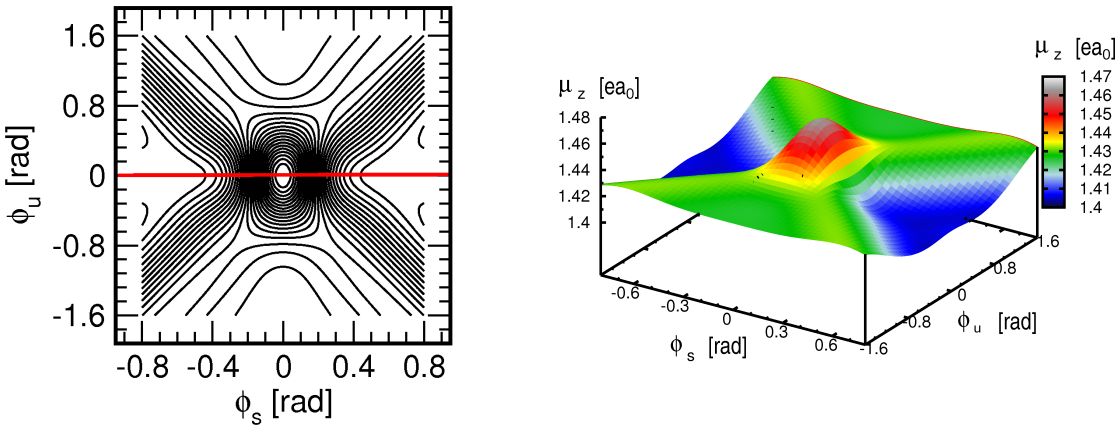

Figure 4.8: Contour and perspective plot, of the z-component of the static dipole function μ_z in ea_0, perpendicular to the Si-surface, calculated for the COD@$Si_{15}H_{16}$ cluster by Dokić et al. [143]. All calculations were done at a B3LYP/6-31G(d) level of theory for the neutral ground state. ϕ_s, ϕ_u: collective coordinates. The isolines are separated by 2×10^{-3} ea_0 per isoline. **Red line**: 1 D switching coordinate.

neutral ground state in collective coordinates ϕ_s and ϕ_u. The dipole moment is given in ea_0 and isolines in the contour plot are separated by 2×10^{-3} ea_0.

The red line again symbolizes the 1 D reaction path. Minimal and maximal dipole values are found to be 1.41 ea_0 and 1.46 ea_0, respectively. The maximum is situated in the plot center, while the smallest dipole values are located at $\phi_s \sim \pm 0.63$ rad and $\phi_u \sim 0$ rad. Thus the maximal difference is about 0.06 ea_0 or 0.15 Debye. As for the potential, the slope is steeper along ϕ_s compared to ϕ_u. The triangular pattern at the borders of both plots represent extrapolated parts of the surface which are set to a constant dipole value.

4.3 One-dimensional density matrix propagation

Here, the switching proceeds only along the ϕ_s coordinate, taking the maximum in the two-dimensional (2 D) potential center as the switching barrier. The C_2 symmetry is preserved during the 1 D switching process. First the eigenstates obtained via the FGH method for 1 D potential surface cuts are discussed. There are three different surfaces, namely for the neutral ground state and for anion and cation resonances, as obtained via Koopmans' theorem (see Eq. (2.9)).

Results obtained for exclusive propagation in the neutral one-dimensional ground state (1S1D) are shown first (see Sec. 4.3.4 - 4.3.6). As mentioned before, those refer to the *below-threshold regime*, where the energy of tunneling electrons is lower than the energy gap between ground state and the resonance state. The resonance state surfaces enter via the rate formula, used to describe the process of resonance-induced vibrational excitation. Further, dipole-induced switching and the influence of temperature will be discussed.

Later in this section (Sec. 4.3.7) we present results for the *above-threshold regime* of resonance excitation for comparison. The reader is reminded that in this case the second

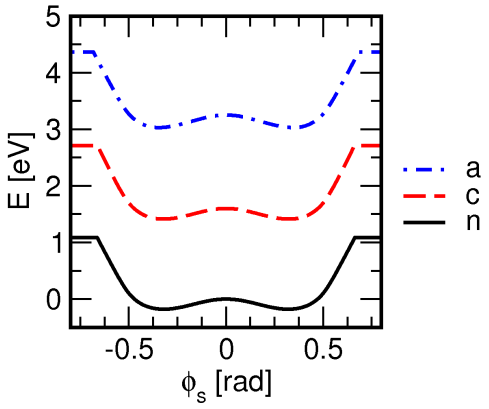

Figure 4.9: 1 D potential surfaces for the neutral (n), cation (c) and anion (a) electronic states of COD@Si(100), as obtained from 1 D cuts along ϕ_s of 2 D potential surfaces based on B3LYP/6-31G(d) COD@$Si_{15}H_{16}$ cluster calculations by Dokić et al. [143] (Sec. 4.2). All surfaces are shifted downward by 0.179 eV in order to set the neutral state maximum as zero point in energy ($V(\phi_s = \phi_u = 0) = 0$ eV).

grid boundaries, ϕ_s [rad]	± 0.8
number of grid points	1000
moment of inertia, I_s [m_e]	218952.18
potential cutoff [eV]	≈ 1.3

Table 4.2: Fourier Grid Hamiltonian (FGH) parameters, used for the calculation of 1 D vibrational eigenstates of COD@Si(100), based on potentials presented in Fig. 4.9 for the neutral, anion and cation states. The cut-off energy is defined with respect to the global potential minima of each potential.

resonance surface is explicitly included in the density matrix propagations (2S1D). The neutral ground state population is projected instantaneously to the anion or cation surface at the beginning of each propagation. Subsequently, the population is evolving and decays back to the ground state, where the final vibrational relaxation takes place. A comparison of results obtained for both single-surface (1S1D) and two-surface (2S1D) approaches completes the section.

4.3.1 Vibrational eigenstates

The 1 D reaction path was already indicated as a red line in the 2 D potential surface plots for neutral (Fig. 4.6) and resonance surfaces (Fig. 4.7) as presented in Sec. 4.2. The resulting 1 D potential cuts for neutral, anion and cation surfaces are shown in Fig. 4.9. For the neutral surface the barrier maximum is set as the zero point in energy and the resonance surfaces are shifted accordingly. Using the 1 D Hamiltonian in Eq. (4.9), the Fourier Grid Hamiltonian (FGH) method permits obtaining the vibrational eigenstates. Parameters used for the 1 D FGH input are shown in Tab. 4.2. Potential cutoff, grid length and number of points are sufficient to resolve at least 50 eigenstates or 25 doublets n for all three surfaces. As for the 1 D double well potential of hydrogen on Si(100), the eigenfunctions appear as doublet pairs $\psi_n^{\pm}$ of odd (+) and even (−) parity. Eigenenergies of even eigenfunctions E_n^+, tunnel splittings ΔE_n and tunneling times T_n for the first 20 doublets ($n = 0 \ldots 19$) of the neutral ground state are summarized in Tab. 4.3. Negative eigenvalues of the first 5 ground state doublets show their energetic location below the switching barrier. For the 6th doublet ($n = 5$) the energies of the even and odd eigenstates are found to be slightly below and above the barrier, respectively. The 20 doublets cover

Doublet (n)	E_n^+ (meV)	ΔE_n (meV)	T_n (ps)
0	-161	8.0×10^{-8}	2.6×10^{7}
1	-125	1.1×10^{-5}	1.9×10^{5}
2	-92	7.2×10^{-4}	2.9×10^{3}
3	-58	2.8×10^{-2}	74
4	-27	0.63	3.3
5	-4	5.8	0.36
6	19	14	0.15
7	49	17	0.12
8	85	19	0.11
9	124	21	9.9×10^{-2}
10	166	22	9.3×10^{-2}
$\vdots$	$\vdots$	$\vdots$	$\vdots$
19	644	30	6.9×10^{-2}

Table 4.3: Eigenenergies E_n^+ for wave function of even parity ψ_n^+ and doublet n, corresponding tunnel splittings ΔE_n and tunneling times T_n, as obtained by the FGH method for the 1 D neutral ground state potential of COD@Si(100) (Fig. 4.9) as calculated by Dokić et al. [143].

an energy range of 0.81 eV, where the potential energy cutoff is set to 1.27 eV. Tunnel splittings ΔE_n and tunneling times T_n are calculated via Eq. (3.5) and Eq. (3.6).

The values obtained for T_n start at 26 μs for doublet 0, reach the ns-regime at the barrier top and approach the regime of a tenth of a ps for doublets $n > 7$. Approximate harmonicity is seen for doublets below the barrier, with a repeating energy spacing of ≈ 34 meV. Later the energetic spacing decreases to about 23 meV around the barrier top and slightly increases again afterwards. The calculated eigenstates $\psi_n^{\pm}$ and $n = 0 \cdots 6$ are plotted along ϕ_s within the neutral state potential surface at the right hand side of Fig. 4.10.

Eigenenergies, tunnel splittings and tunneling times for the anion and cation surfaces are given in Appendix E. All three sets of eigenvalues are very similar, as expected, because of rather similar potential shapes. The energetic spacing between delocalized eigenfunctions ψ_0^+ and ψ_1^+ of cation and anion surfaces are 36 meV and 38 meV, respectively. It can be seen from Tab. 4.1, that the anion minimum is slightly shifted outward by ≈ 0.03 rad, with respect to the positions of the neutral and cation minima. The anion barrier is slightly broader and ≈ 40 meV higher, compared to cation and neutral surfaces. Tunnel splittings for the anion are therefore two orders of magnitude smaller for the lowest 4 doublets. After doublet 6 the splittings are comparable to those obtained for cation and neutral surfaces.

The localization quality of right well localized functions Q_n^R, where $Q_n^R = Q_n^L$, of the neutral ground state is obtained via Eq. (2.12) and plotted on the left-hand side of Fig. 4.10 for the ground state. All states below the barrier, up to doublet $n = 4$ are perfectly localizable ($Q_n^R > 99\,\%$). Above the barrier, the degree of localization decreases to about $\approx 82\,\%$, for doublets $n \approx 10 \ldots 25$. As mentioned in Sec. 2.3, all IET-induced population transfer

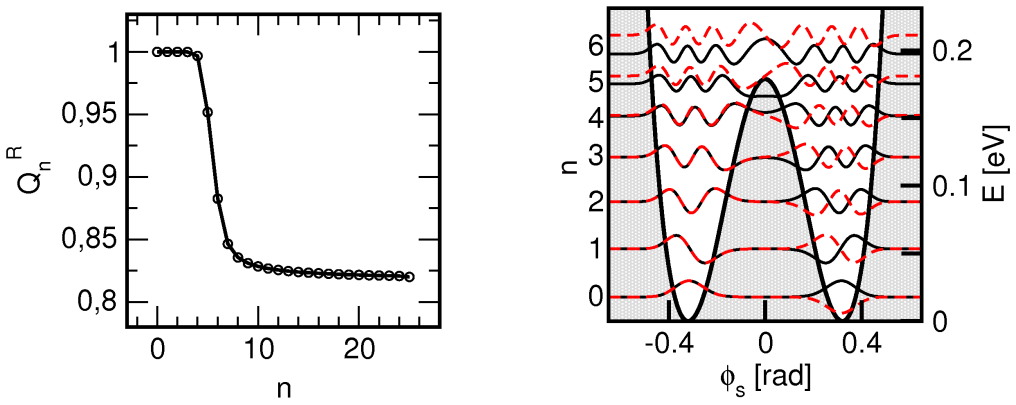

Figure 4.10: Left: Localization quality Q_n^R (Eq. (2.12)) of states $\tilde{\psi}_n^R$ which are localized within the 1 D, neutral electronic ground state potential, as plotted in Fig. 4.9 and calculated by Dokić et al. [143]. Right: Double-minimum potential along ϕ_s and delocalized doublets $n = 0 \cdots 6$ obtained via the FGH method.

rates $W_{f\leftarrow i}$ are defined between all possible combinations of L- and R-localized states $\tilde{\psi}_n^{L,R}$. Therefore rate-based $L \leftrightarrows R$ transitions are possible.

4.3.2 Propagation details

The Liouville-von Neumann equation of motion for the density matrix is solved via a Runge-Kutta integrator of fourth order (see Appendix B). The time step is fixed to 30 $\hbar/\mathrm{E}_h$ and 25 $\hbar/\mathrm{E}_h$ for single-surface and two-surface calculations, respectively. For resonance lifetimes below 1 fs and vibrational lifetimes below 0.1 ps the time step is further reduced by a factor of 10. The overall length of each propagation is set to $\approx 10 \times \tau_1^{vib}$, where τ_{vib}^1 is the vibrational lifetime of the first (localized) vibrational state as defined in Sec. 2.5.2.

The tunnel splitting for the lowest doublet ΔE_n is set to zero for all propagations. This is done to avoid tunneling on the μs-timescale of the localized wave packet created from ψ_0^+ and ψ_0^- eigenfunctions of the ideal symmetric double-minimum potential. In reality, however, this would not happen because surface imperfections and the presence of the tip will lead to localized initial wave functions and tunneling is suppressed. For H@Si the phenomenon was not observed, since the tunnel splitting ΔE_0 is much smaller than for COD@Si (Tab. 3.3 and Tab. 4.3).

4.3.3 Harmonic, bilinear dissipative model: $W_{f\leftarrow i}^{rel}$

Vibrational quanta can be exchanged between vibrational system degrees of freedom and the surface phonon-bath. As in the case of H@Si(100), vibrational upward and downward transition rates $W_{f\leftarrow i}^{vib}$ are calculated for two sets of functions $\tilde{\psi}_i^{L,R}$, localized in the left (L) or right (R) ground state potential well. Transition rates between vibrational levels are evaluated on the basis of a harmonic, bilinear dissipative model with vibrational transition rates $W_{f\leftarrow i}^{vib}$ scaling linearly with state number i (see Eq. (2.39)).

parameter	value
A_0	0.0574993
σ	0.222262
A_1	1.40562

Table 4.4: Fit function parameters for the 1 D dipole surface cut $\mu_z(\phi_s)$ of COD@Si(100), as plotted in Fig. 4.8.

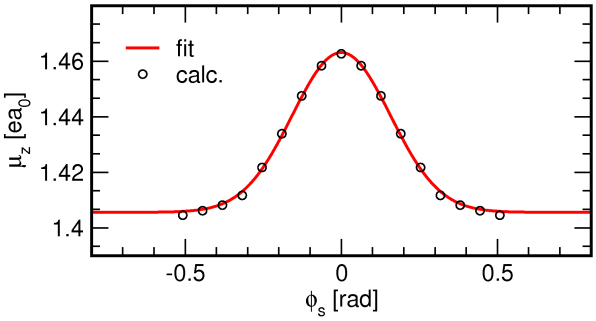

Figure 4.11: B3LYP/6-31G(d) calculated (calc.) and Gaussian fitted (fit) dipole values μ_z along ϕ_s for the COD@Si(100) dipole surface as presented in Sec. 4.2.4, based on B3LYP/6-31G(d) calculations of Dokić et al [143]. Further details of the fit are discussed in the text.

All dissipative rates obey the selection rule of $\Delta v = \pm 1$ and $\tau_1^{vib} = 1/W_{0\leftarrow 1}^{vib}$ enters as the only parameter defining the dissipative strength. As before, upward rates are given by the detailed balance condition in Eq. (2.40) and permit the testing of the influence of temperature on the switching rate. No experimental or theoretical data are available for τ_1^{vib}, which is set to 1.0 ps in the following, if not stated otherwise. This choice is motivated by the following considerations. Due to the selection rule ($\Delta v = \pm 1$), any phonons absorbed or emitted by the system are below 400 cm^{-1} in energy. Therefore they are well below the Debye frequency of the silicon surface, which allows for an efficient decay of vibrational quanta into the silicon bulk via 'fast' single-phonon processes.

4.3.4 Dipole-induced switching: $W_{f\leftarrow i}^{dip}$

(1) One-dimensional dipole function:

The dipole component of STM-induced transition rates $W_{f\leftarrow i}^{dip}$ is calculated between localized states $\tilde{\psi}_i$ and $\tilde{\psi}_f$, via first order perturbation theory, using Eq. (2.49). Here, the dipole component perpendicular to the surface $\mu_z(\phi_s)$ is used along the 1 D switching coordinate ϕ_s. A corresponding cut of the 2 D dipole surface is fitted to a single Gaussian,

$$\mu_z(\phi_s) = A_0 \cdot e^{-(\phi_s/\sigma)^2} + A_1 \quad . \tag{4.11}$$

The fit parameters (A_0, A_1, σ) are shown in Tab. 4.4. The cut includes 17, B3LYP/6-31G(d)-calculated, dipole values for μ_z between $\phi_s = \pm 0.508$ rad, as calculated by Dokić et al. [143]. Two calculated dipole values at the surface border are omitted, as already discussed in Sec. 4.2.4. Both the fit and the calculated values are plotted in Fig. 4.11, showing good agreement. The fit of the entire 2 D dipole function (Eq. (D.1)) is much more complicated and was not available from the beginning. Therefore, Eq. (4.11) was used for the 1 D case instead of a cut $\phi_u = 0$ through the 2 D dipole surface. For comparison, the dipole function for the 1 D and 2 D case are plotted as black and red line in Fig. 4.12, respectively. Both functions are identical except for minor oscillations introduced by the

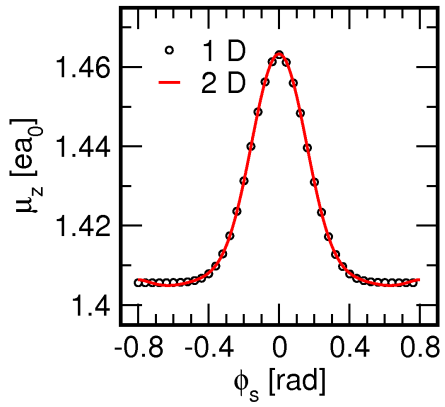

Figure 4.12: Permanent dipole component $\mu_z(\phi_s, \phi_u = 0)$ for COD@Si(100) as calculated via one- (1 D) and two-dimensional (2 D) analytical fit functions, Eq. (4.11) and Eq. (D.1), respectively.

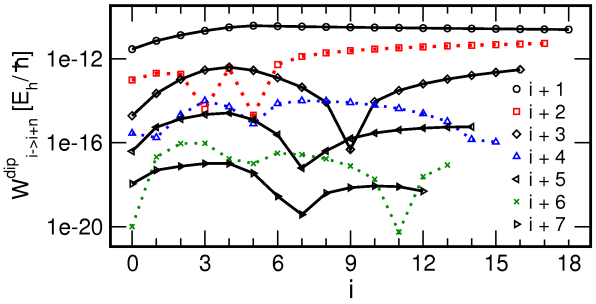

Figure 4.13: Dipole-induced transition rates $W^{dip}_{i+n\leftarrow i}$ between (left-) localized states of the COD@Si(100) 1 D model. $I = 1\,\mathrm{nA}$.

2 D fit, at the outer regions of the 2 D fit, resulting in slightly increased switching rate for the 2 D surface, while preserving the linear switching rate dependence on the STM current.

(2) Discussion of calculated dipole rates:

Before starting to discuss the calculated dipole rates $W^{dip}_{f\leftarrow i}$ for the system, the inelastic STM tunneling current fraction $\eta^{dip}_{1\leftarrow 0}$ is estimated for the COD@Si(100) system and a current of 1 nA, as already done for H@Si on page 38. Using Eq. (2.49) a rate $W^{dip}_{1\leftarrow 0}$ of about $2.9 \times 10^{-12}\,(\hbar/\mathrm{E}_h)^{-1}$ or $1.2 \times 10^5\,\mathrm{s}^{-1}$ is found for the $1 \leftarrow 0$ transition between ground and first excited vibrational states localized in the left potential well. The resulting value for $\eta^{dip}_{1\leftarrow 0}$ is 1.9×10^{-5}, which is smaller than the value of 7.5×10^{-4}, calculated for the H@Si(100) system (see Sec. 3.3.2) and other cases [34, 76, 71]. Nevertheless, because of the shallow barrier, even weak dipole coupling is sufficient to achieve switching yields, which are comparable to experimental values, as presented in the following.

The dipole transition rates $W^{dip}_{f\leftarrow i}$ between non-harmonic, left-localized, vibrational levels $\tilde{\psi}_i$ and $\tilde{\psi}_{i+n}$ are plotted in Fig. 4.13. The $i+1 \leftarrow i$ rates are smooth and dominate over the whole range of states i. Higher transitions, like the $i+2 \leftarrow i$ overtone transition and so forth, do not show the same smoothness as the $i+1 \leftarrow i$ transition rates. The $i+n \leftarrow i$ transition rates decay with increasing n. The existence of 'overtone' transitions for such systems is not surprising as was already shown for H@Si in the preliminary chapter (see Sec. 3.3.2). They reflect both the anharmonicity of the ground state potential and the non-linearity of the dipole function.

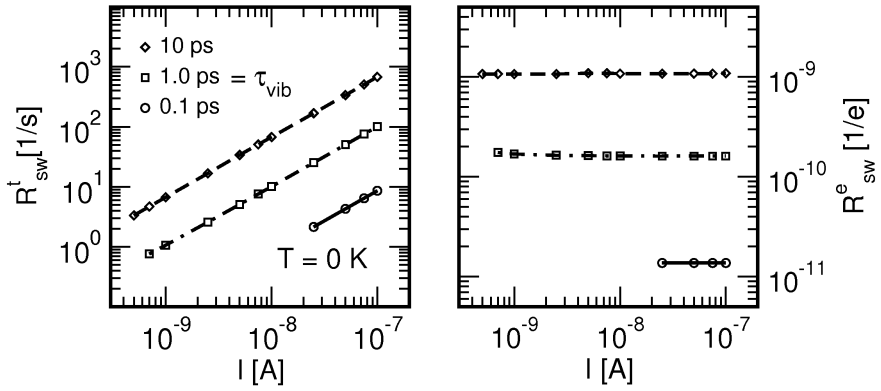

Figure 4.14: Dipole-induced switching rates R^t_{sw} [Hz] and rates per electron R^e_{sw} [Hz] [1/e] with respect to the STM current and depending on different vibrational lifetimes τ_1^{vib}. $T = 0\,\mathrm{K}$.

(3) Switching mechanism:

In the following we want to explore if and how dipole-induced vibrational transitions switch the COD molecule at the silicon surface. Therefore we extract the switching rate, as explained in Sec. 2.7 on page 27 for a set of 1S1D propagations. Here, two parameters are tested. First, the parameter I, representing the STM current, is varied between 1 to 10 nA. Secondly, the vibrational lifetime τ_1^{vib} is set to 0.1, 1 and 10 ps, respectively. An interesting behavior can be seen in Fig. 4.14, where the switching rate and the rate per electron are plotted versus the current. Obviously the switching rate R^t_{sw} increases linearly with current, therefore the switching rate per electron R^e_{sw} stays constant, which is in accordance with experimental findings [145]. Therefore, the conformational switching of COD on Si(100) can be explained by a dipole-induced *single* electron process. The experimentally observed quantum yield is about 1.0×10^{-9} per electron [10], which can be approximately reproduced for a vibrational lifetime $\tau_1^{vib} = 10\,\mathrm{ps}$, as plotted in Fig. 4.14. By lowering the lifetime to 1 ps and 0.1 ps, the quantum yield decreases approximately by one or two orders of magnitude, respectively. In order to further understand the influence of τ_1^{vib} on the switching rate, the underlying mechanism has to be analyzed.

In Fig. 4.15 the role of dipole-induced overtone excitation is investigated by showing the switching rate per electron as a function of the maximal 'inter-state distance' $n_{\max}$ of dipole- and relaxation-rate driven population transfer. The parameter sets the maximal number of states between any vibrational levels i and $i + n_{\max}$, connected by a rate $W_{i+n_{\max}\leftarrow i}$. Two vibrational lifetimes τ_1^{vib} of 1 ps and 10 ps are tested for a current of 100 nA. The switching rate per electron increases strongly up to a value of $\Delta i \approx 5$. Afterwards a constant switching rate is seen. The following interpretation is provided for the observed behavior. It is already known that the switching process is driven by a single, dipole-induced transition. At the temperature of 0 K, all population is located in the vibrational ground state initially. According to Fig. 4.15, direct transfers to states 4 and 5 are sufficient for the switching, since according to Tab. 4.3 tunneling times are 3.3 ps and 0.36 ps for states 4 and 5, respectively. State 4 is still below and state 5 already right

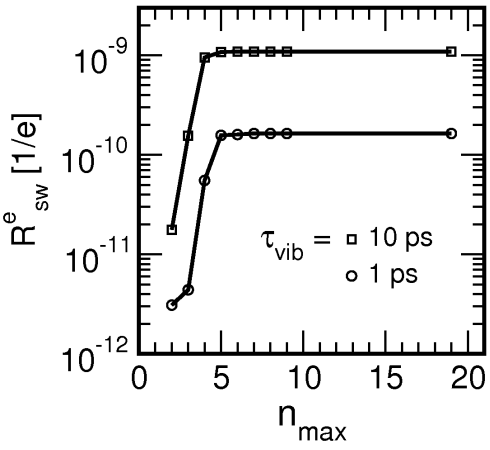

Figure 4.15: Switching rate per electron R^e_{sw} for dipole-induced switching, depending on $n_{\max}$, where $n_{\max}$ is the maximal quantum number up to which dipole and dissipative transitions: $W_{f\leftarrow i} = W^{vib}_{f\leftarrow i} + W^{dip}_{f\leftarrow i}$ have been included. $T = 0\,\mathrm{K}$, $I = 100\,\mathrm{nA}$.

at the top of the barrier. Therefore, the switching is based on tunneling at the barrier top, after excitation by a single-electron process. A reduced vibrational lifetime hinders the tunneling process and the switching rate is lowered, as seen in figures 4.14 and 4.15. For the same reason, the maximal switching rate is reached at $n_{\max} = 4$ for a vibrational lifetime of 10 ps but at $n_{\max} = 5$ for the a lifetime of 1 ps in Fig. 4.15.

In summary, switching is driven by dipole-induced overtone excitations and subsequent tunneling. A dominance of overtone excitations over 'traditional ladder climbing' is observed. Such effect was already expected by Walkup et al. in the limiting case of low STM currents [70], as considered here.

(4) Influence of vibrational lifetime and L↔R-rate driven switching:

Within the harmonic, bilinear dissipative model for vibrational relaxation (see Sec. 2.5.2), only transitions within the left or right well are allowed for. The dipole rates, instead, are calculated between all possible combinations of localized states. Since the localizability is reduced to $\approx 82\,\%$ for states above the barrier transition rates between left and right well localized states are possible. The influence of those inter-well transitions on the switching rates is studied for the dipole-induced switching in the following. In Fig. 4.16 the switching rate per electron is plotted versus the vibrational lifetime τ_1^{vib}. Curve (a) includes the complete set of dissipative and dipole-induced rates. In curve (b) only dipole transitions between either left or right well localized functions are allowed. That means all inter-well transition rates are set to zero. It can be seen that the contribution of dipole-rate-induced switching is not dominating over the whole range of τ_1^{vib} and that the major contribution for the switching process comes from tunneling. A brief explanation of the strong switching rate dependence on τ_1^{vib}, as observed in Fig.4.16, was already given previously. In the range between 0.1 ps and 1.0 ns, the switching rate increases by roughly four orders of magnitude, since tunneling becomes more efficient for weaker dissipation.

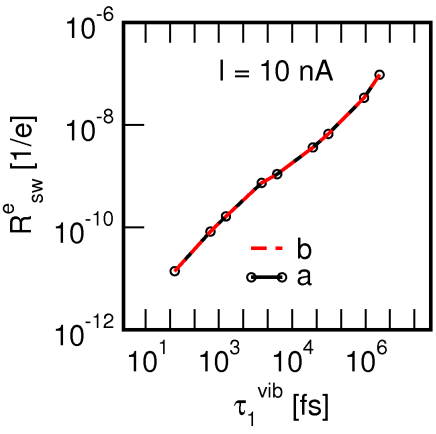

Figure 4.16: Dipole-induced switching rates R_{sw} [1/e] in dependence on the vibrational lifetime of the first vibrationally excited state τ_1^{vib}. (a) Dipole transitions between all states allowed. (b) Only dipole transitions exclusively within left or right well are included. $T = 0\,\mathrm{K}$, $I = 10\,\mathrm{nA}$.

4.3.5 Temperature-assisted switching

(1) Arrhenius expression:

The coupling between vibrational system modes and surface phonons allows for a thermal equilibration between both heat reservoirs of system and bath. The heat flow out of and into the system is described via downward and upward population transfer rates, as governed via the detailed balance condition Eq. (2.40). The condition ensures that the system population resembles a Boltzmann distribution in case of being in a thermal equilibrium state. It is expected that an temperature-induced increase of excited vibrational state population results in an increased rate for the conformational switching of COD.

For an analysis of the temperature dependence the Arrhenius rate law is used. The Arrhenius rate law provides a simple quantitative connection between temperature T and the temperature-dependent reaction rate $R^t_{sw}(T)$,

$$R^t_{sw}(T) = A \cdot e^{-E_A/(k_B T)} \quad , \tag{4.12}$$

depending further on prefactor A, activation energy E_A and Boltzmann constant k_B. In general, the Arrhenius law is based on the assumption of a one-dimensional reaction path. Furthermore, there is no possibility of a 'return' once the barrier is passed and a classical behavior can be assumed, i.e., tunneling is negligible. The Arrhenius law is widely used for the analysis of thermal activated processes at surfaces [147, 148, 149, 150]. For a unimolecular reaction, like the switching of COD considered here, the prefactor A can be interpreted as the frequency of 'collisions' between reactant and reaction barrier. E_A, as activation energy, refers to the 'height' of the reaction barrier. $R(T)$ data are usually pictured in so-called *Arrhenius plots*, as

$$\ln R(T) = \ln A - \frac{E_A}{k_B} \cdot \frac{1}{T} \quad , \tag{4.13}$$

which easily gives access to the values of E_A and A via simple linear regression. Here it is assumed that both values remain constant over the entire temperature range of interest. Any deviation from such linear behavior is classified as being 'non-Arrhenius'.

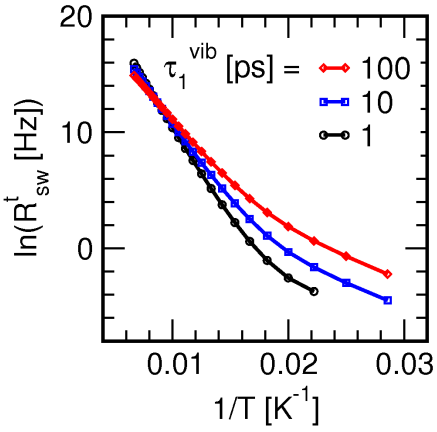

Figure 4.17: Arrhenius plots of purely temperature-induced switching. Results for three different vibrational lifetimes τ_1^{vib} are plotted. Corresponding Arrhenius rate law parameters are listed in Tab. 4.5.

In the following section, several Arrhenius plots are used in order to investigate the temperature dependence of switching rates using the harmonic, bilinear dissipative model (Sec. 2.5.2). After discussing the purely temperature-induced switching process, the combined excitation via both thermal and dipole mechanism will be considered and a comparison to experimental results will be made.

(2) Purely temperature-induced switching:

The Arrhenius plot for purely thermally-induced switching is shown in Fig. 4.17. The rates were calculated from density matrix propagations using only dissipative rate equations (2.36) and (2.40), starting with all population in the left-localized vibrational ground state. Three different lifetimes τ_1^{vib} of 1, 10 and 100 ps are tested for bath temperatures between 5 and 150 K. When looking at the plot from the right (low temperatures) to the left, three different regimes can be identified in the Arrhenius plot for each lifetime. First, coming from the right, up to $\sim 46\,\mathrm{K}$ ($\sim 0.022\,\mathrm{K}^{-1}$), a region of an approximately constant slope is seen. (Since switching rates become too small at lower temperatures, no further data points are available.) Secondly, the slope increases between $\sim 46\,\mathrm{K}$ ($\sim 0.022\,\mathrm{K}^{-1}$) and $\sim 66\,\mathrm{K}$ ($\sim 0.015\,\mathrm{K}^{-1}$). The third part, above $\sim 66\,\mathrm{K}$ (below $\sim 0.015\,\mathrm{K}^{-1}$), shows a constant slope which is higher than in the first part.

This can be explained as follows. Initially all population is in the left-localized vibrational ground state. Tunneling is not allowed here, as discussed in Sec. 4.3.2. Therefore, population has to be transferred to the next doublet ($n = 1$) which is 36 meV higher in energy, where tunneling on a 100 ns scale is possible. Thus, the slope of the first curve resembles an activation energy of 39 meV and the first doublet is the dominant switching channel. With increasing temperature, faster tunneling at energetically higher doublets becomes possible. Therefore, the slope of all three curves increases, as seen in the second part between $\sim 46\,\mathrm{K}$ and $\sim 66\,\mathrm{K}$. After the 6th doublet ($n = 5$), however, tunnel splittings and tunneling times stay rather constant (see also Tab. 4.3). Therefore, a constant slope is seen for the temperature range above 66 K, as would be expected for a classical *"over the barrier"* process. Here, only the population, in doublets above $n = 6$, given by bath temperature and energy level, dominates the switching rate. E_A and A, as found along

τ_1^{vib}[ps]	1	10	100
A [Hz]	4.098×10^{11}	4.722×10^{10}	5.185×10^{9}
E_A [meV]	140.3	118.8	96.8

Table 4.5: Activation energies E_A and frequency factors A according to the Arrhenius rate law applied on three data sets of temperature-dependent switching rates, as shown in Fig. 4.17, for the regime $T \geq 66\,\mathrm{K}$.

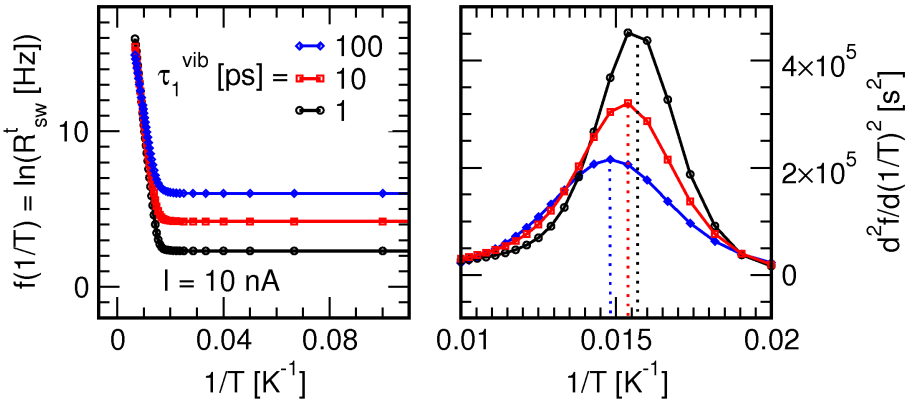

Figure 4.18: Left: Arrhenius plots of temperature and dipole-induced switching of COD@Si(100). Right: Second derivatives of all plots shown in the left, with respect to T^{-1}. The underlying switching rates R_{sw} [Hz] were calculated for three different vibrational COD lifetimes τ_1^{vib}. The STM tunneling current I is set to 10 nA. The Arrhenius rate law parameters for the steep descending curve parts in the left and the maxima positions of the 2nd derivatives ($\approx$ crossover temperature T_c) are listed in Tab. 4.6.

the linear increasing rates above 66 K, are shown in Tab. 4.5 for all three lifetimes. Two major trends are seen here, namely a decrease of E_A and A for an increasing vibrational lifetime τ_1^{vib}.

(3) Combined dipole- and temperature-induced switching:

This section treats the temperature dependence of the switching of COD@Si, including the dipole mechanism in addition to purely thermal transitions.

The influence of the vibrational lifetime: The Arrhenius plots of switching rates and their second derivatives with respect to $(1/T)$, are shown on the left and right hand sides of Fig. 4.18, respectively. All rates are calculated for a constant tunnel current of 10 nA and three different lifetimes ($\tau_1^{vib} = 1$, 10 and 100 ps). An 'elbow' shape is seen as the main feature of all three plots. First, a temperature independent region with a constant switching rate is seen for temperatures below $\approx$ 60 K. It is followed by a part with a linear increase of rates on the logarithmic scale caused by classical thermally-activated Arrhenius-like behavior. The corresponding rate law parameters are shown in Tab. 4.6. They are almost identical to those observed for the purely thermal switching as plotted in Tab. 4.5. It is concluded that the switching is nearly entirely driven by thermal processes above $\approx$ 60 K.

τ_1^{vib}[ps]	1	10	100
$1/T_c\,[\mathrm{K}^{-1}]$	0.016	0.0155	0.0145
$T_c\,[\mathrm{K}]$	63	65	69
A [Hz]	4.356×10^{11}	4.793×10^{10}	4.387×10^{9}
E_A [meV]	141.0	119.0	94.8

Table 4.6: Cross-over temperatures $T_c\,[\mathrm{K}]$, $1/T_c\,[\mathrm{K}^{-1}]$ and Arrhenius rate law parameters A [Hz] and E_A [meV] for Arrhenius plots of dipole- and temperature-induced switching rates of COD@Si(100), depending on the vibrational lifetime τ_1^{vib} and temperature T as plotted in Fig. 4.18.

The lifetime dependence has already been discussed in Sec. 4.3.5. The temperature-independent part is due to switching via the dipole mechanism and the rate increases for longer lifetimes, as expected. Some population in states with energies below the barrier is allowed to switch via tunneling. The 'crossover temperature' T_c, as midpoint between both regimes, is found via the maximum of the second derivative of the switching rate with respect to the temperature: $d^2R^t_{sw}(T^{-1})/d(T^{-1})^2$. This estimation of T_c is only approximate with an estimated error below 5 K. The values for T_c are listed in Tab. 4.6. The differences are smaller than the mentioned error of 5 K but it can be seen that T_c depends on the vibrational lifetime and increases with τ_1^{vib}. As already discussed for the purely dipole-induced switching, a weaker dissipation leads to higher switching rates. The higher the base level of dipole-induced switching, the higher are the temperatures needed for the temperature-induced switching in order to dominate the process. This results in a rise of T_c, which explains the observed trend.

Several further examples of a crossover between classical (thermal) and quantum (tunneling-dominated) behavior for surface-adsorbate systems can be found in the literature. Sn adatoms, for example, form specific 3×3 super-structures on Ge(111), where they appear in two possible vertical ('up' and 'down') positions. In an STM analysis of time- and temperature-dependent position inversion of individual Sn atoms, a crossover temperature of 15 K between classical and quantum regimes was found [149]. As another example, two combined experimental and theoretical studies of H-atom diffusion on nickel and copper surfaces found crossover temperatures of 63 K and 60 K, respectively [148, 150].

The influence of the STM current: The influence of the tunnel current on the value of T_c is examined, as shown in Fig. 4.19. The 'elbow' shaped Arrhenius plots can be seen on the left side. The dipole-induced, temperature-independent part increases with the current. The higher the base level of dipole-induced switching, the higher are the temperatures needed in order to allow thermal excitation to dominate the switching and T_c is shifted to higher temperatures as seen from Tab. 4.19. Therefore an external parameter, namely the STM tunnel current, influences the position of T_c. This finding is a new aspect, not reported for similar experiments mentioned above [148, 149, 150]. There, T_c was only determined by the internal characteristics of the system, like barrier height and width.

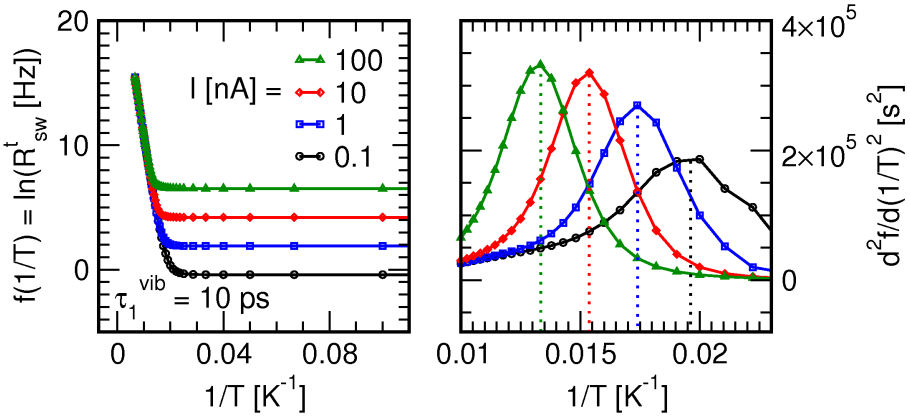

Figure 4.19: Left: Arrhenius plots of temperature- and dipole-induced switching of COD@Si(100). Right: Second derivatives of all plots shown in the left, with respect to T^{-1}. The underlying switching rates R^t_{sw} [Hz] were calculated for four different STM tunneling currents I [nA]. The vibrational lifetime τ_1^{vib} is set to 10 ps. Corresponding Arrhenius rate law parameters are listed in Tab. 4.7.

I [nA]	0.1	1	10	100
$1/T_c$ [K^{-1}]	≈ 0.019	0.0175	0.015	0.013
T_c [K]	≈ 53	57	67	77
A [Hz]	3.714×10^{10}	3.928×10^{10}	4.793×10^{10}	5.602×10^{10}
E_A [meV]	116.6	117.1	119.0	120.4

Table 4.7: Cross-over temperatures T_c [K], $1/T_c$ [K^{-1}], Arrhenius rate law parameters A [Hz] and E_A [meV] for plots of dipole- and temperature-induced switching rates of COD@Si(100) depending on temperature T and tunnel current I as plotted in Fig. 4.19.

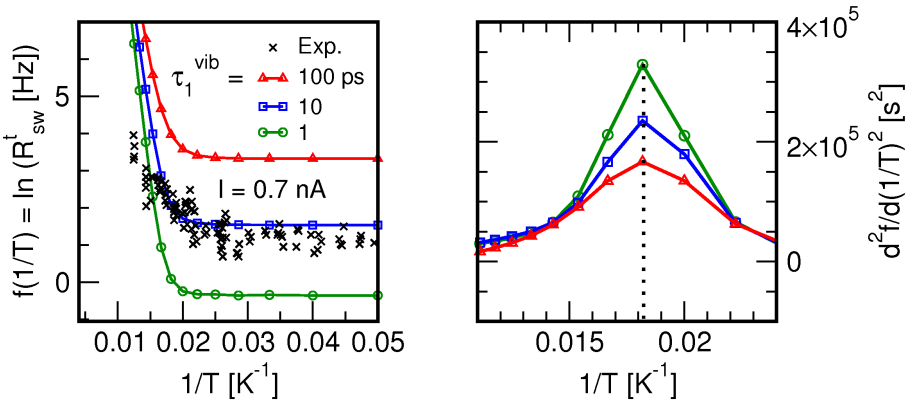

Figure 4.20: Left: Arrhenius plots of temperature and dipole-induced switching of COD@Si(100). Right: Second derivatives of all plots shown in the left, with respect to T^{-1}. Comparison between calculated (solid lines) and STM experimental data (black crosses) [151]. Calculations: Switching rates R^t_{sw} [Hz] for three different vibrational lifetimes τ_1^{vib} of 1, 10 and 100 ps and a current of 0.7 nA. Experiment: Switching rates in [Hz], obtained for measurements of the tunnel current *vs.* time. The tip was centered above a single COD molecule in a constant position. STM current and bias were initially set to 0.7 nA and +1.50 V, respectively. Further details are given in the text.

Comparison to experiment: It was mentioned in the introduction that the observed binary telegraph noise is seen as the result of conformational switching of COD at Si(100) between the two minima [10, 145]. Up until now, the experimentally observed single-electron mechanism and the measured switching yield per electron could be reproduced within the framework of our calculations by including only dipole-induced (and thermal) transitions. The temperature-dependence, as obtained from the simulations, was tested experimentally [151]. The measurements, motivated by the theoretical predictions of T_c, validated the theoretical findings, as will be shown in the following. Fig. 4.20 again shows Arrhenius rate plots for COD@Si(100), considering three different lifetimes τ_1^{vib}. The current is set to 0.7 nA, in order to meet experimental conditions [151]. The experimental data points (black crosses) were recorded within a temperature range of 5 K to 80 K. Experimental difficulties, caused by the temperature increase, such as surface vibrations, desorption of impurities from the surfaces of the STM chamber and temperature-induced sample drifts did not allow for stable measurements above 80 K. For the measured temperature-independent portion, the closest agreement with theory is seen for τ_1^{vib} being in the order of 10 ps, as already discussed in Sec. 4.3.4. Theoretically obtained values for T_c, A and E_A, are summarized in Tab. 4.8. In the STM-experiment a crossover behavior was seen at ≈ 45 K, while the theoretical prediction for $I = 0.7$ nA is at 56 K (see Tab. 4.8). Considering all the approximations of our model, as well as the error coming with the experiment, such precise agreement is a persuasive result of the actual study. An experimental check of the predicted current dependence of T_c is underway to be tested in the same laboratory [2].

As can be seen from the second derivatives in Fig. 4.20, no clear τ_1^{vib}-dependence of T_c is observed at 0.7 nA. A weak dependence of T_c on τ_1^{vib} has to be expected, as seen for

[2]Personal communication: Stefan Fölsch, Paul-Drude-Institut, Berlin, Germany

τ_1^{vib} [ps]	1	10	100
$1/T_c$ [K^{-1}]	0.018	0.018	0.018
T_c [K]	56	56	56
A [Hz]	2.9×10^{11}	3.3×10^{10}	4.0×10^{9}
E_A [meV]	136.9	115.3	94.0

Table 4.8: Cross-over temperatures T_c [K], $1/T_c$ [K^{-1}] and Arrhenius rate law parameters A [Hz] and E_A [meV] for plots of calculated dipole- and temperature-induced switching rates of COD@Si(100), depending on temperature T and vibrational lifetime τ_1^{vib} [ps] as plotted in Fig. 4.20.

example in Fig. 4.18 for an STM current of 10 nA. At 0.7 nA the switching rates were much smaller and the error due to numerical noise too high in order to obtain a better resolution for the second derivative plot.

The Arrhenius parameters, for the simulated rates, are in agreement with the values of former calculations, listed in Tab. 4.6, obtained at $I = 10$ nA. For the experimental data no Arrhenius parameters were obtained. The reason is the restricted temperature range in which the experiment can be performed, i.e., below 80 K, and an increase of the experimental error with increasing temperature.

4.3.6 Resonance-induced switching: Below-threshold regime, $W_{f\leftarrow i}^{res}$

(1) Introduction:

Up until now, the influence of temperature on dipole-induced switching has been tested in detail. In the following, the below-threshold, resonance switching regime will be studied as another or additional possibility of IET-induced switching of COD@Si. The study is performed on the basis of one-dimensional vibrational wave functions of the electronic ground state surface 1S1D model. As stated before (Sec. 4.1), no pronounced voltage dependence was found for the switching rates within a bias voltage range of -2.5 to 2.5 V. This seems to exclude a resonance mechanism, since the resonance-mediated IET-rates typically show a distinct voltage-dependence (see Sec. 2.5.3). However, the lack of experimental evidence of a resonance does not fully exclude the presence of resonance-mediated vibrational excitation and switching. For Xe adsorbed on nickel, for example, surface-tip hopping was obtained at ± 0.8 V, while the responsible $6s$ resonance level is 4 to 5 eV away from the Fermi level [30]. Eigler et al. concluded, that even *far-off-resonances* can be important tunneling channels for electrons from the STM tip [152]. For a typical resonance lifetime $\tau_{res} = \hbar/\Gamma$ of ≈ 1 fs, the corresponding width in energy Γ is about 0.7 eV. The width becomes smaller for longer resonance lifetimes. The energy of tunneling electrons is adjustable via the bias voltage. The bias voltage range is limited in practice in order to preserve the stability of the tip and surface arrangement. Therefore, the experiment might not be able to detect such 'narrow', far-off-resonances outside that range. Other experimental techniques, which could prove resonances outside that energy

	N	A	C
$\left.\frac{dV}{d\phi_s}\right\|_{\phi^N_{s,0}}$ [eV/rad]	0	-0.265	0.021

Table 4.9: $\left.\frac{dV}{d\phi_s}\right|_{\phi^N_{s,0}}$: First derivatives of neutral (N), cation (C) and anion (A) potential surfaces, as obtained via cluster calculations and Koopmans' theorem (see Sec. 4.2), with respect to switching coordinate ϕ_s at the left minimum position of the neutral ground state $\phi^N_{s,0}$.

region, such as for example photoemission spectroscopy, have so far not been applied to the current system .

Another scenario is that of a very *short-lived resonance*, whose density of states profile is very broad. The resonance rates $W^{res}_{f\leftarrow i}$ are proportional to the resonance density of states at the Fermi level of the tip [12, 24]. Therefore also the IET-induced switching would vary only very smoothly with the bias voltage for a broad resonance with a short lifetime (e.g. 0.1 fs). The small changes might not be resolvable in an STM experiment.

The parallel existence of anion and cation resonance, not visible via voltage dependent measurements *and* both causing a similar rate of switching, might be unlikely. However, we would like to perform a study of the possible case of IET-induced, resonant switching of COD@Si for a HOMO-derived cation resonance and a LUMO-derived anion resonance in the following. It was seen for H@Si, that possibly involved 'higher' resonant, electronic state surfaces were mostly of similar shape (see Fig. 3.5). Therefore, it is a reasonable assumption to choose HOMO and LUMO energies in the following.

(2) Model, transition rates and switching mechanism:

The 1 D resonant state potential surfaces $V^{\pm}_{es,0}(\phi_s, \phi_u = 0)$ are based on HOMO and LUMO energies of B3LYP/6-31G(d) cluster calculations of Dokić et al. [143], and Koopmans' theorem, as described in Sec. 4.2.3. The energetic distance ΔE_{res} between the Fermi level of the tip and the molecular adsorbate level can not be easily calculated using our simple cluster approach. The energetic distance enters as a parameter ΔE_{res}, instead. From Tab. 4.1 on page 61 it was already seen that HOMO-based cation and neutral surfaces predict rather similar minima positions and barrier heights. The first derivatives of the potential surfaces with respect to the switching coordinate ϕ_s are calculated at the Franck-Condon point of both resonance surfaces. Their values are plotted in Tab. 4.9 and underline the similarity of neutral and cation surface. For the more different, anion surface a force pointing towards the outer potential boarder is seen, while on the cation surface the direction of the comparatively much smaller force vector is reversed. Therefore, intuitively one would expect a higher switching yield for the anion resonance.

In order to study the below-threshold regime, only the neutral ground state vibrational levels have to be included in the density matrix propagation. The resonance-induced

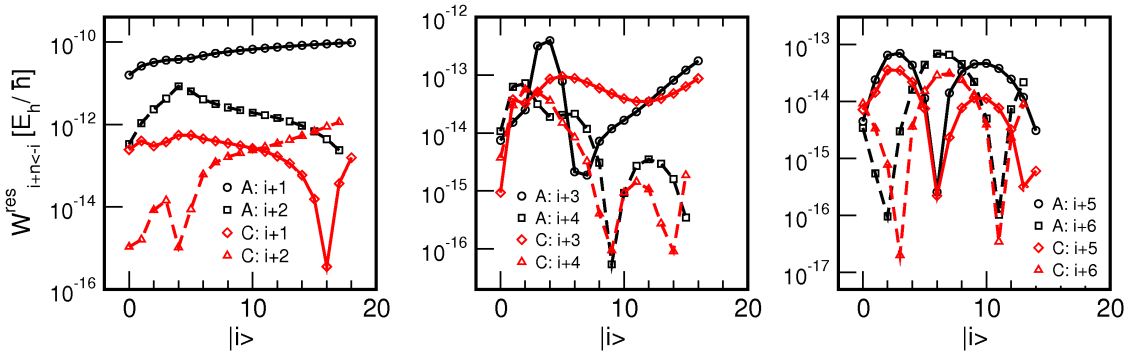

Figure 4.21: Population transfer rates $W^{res}_{i+n\leftarrow i}$ between left-localized states $\tilde{\psi}^L_i$ and $\tilde{\psi}^L_{i+n}$, as obtained via Eq. 2.52 for anion (A) and cation (C) resonance state potentials (see also Sec. 4.2.3). $\tau_{res} = 1\,\text{fs}$, $|\Delta E_{res}| = 1.0\,\text{eV}$, $I = 1\,\text{nA}$.

vibrational excitation and de-excitation events in the ground state are treated by transition rates $W^{res}_{f\leftarrow i}$, obtained via Eq. (2.52) in Sec. 2.5.3. In Eq. (2.52), the following parameters are needed: ground and excited state potential surface, V_{gs} and V_{es}, the energy difference ΔE_{res} between the resonance center and the Fermi level of the STM tip, the tunnel current I and the resonance width $\Gamma = \hbar/\tau_{res}$. A cation state in the sample is created via electrons tunneling from the sample to the STM tip. In the above-threshold regime, the Fermi level of the tip is below the resonance energy here, while the opposite is true in the below-threshold case (see Tab. 2.1). The whole situation is simply reversed for an anion resonance.

Corresponding transition rates $W^{res}_{f\leftarrow i}$, calculated for both resonances, are shown in Fig. 4.21. Here, the resonant transition rates between left-localized wave functions $\tilde{\psi}^L_i$ and $\tilde{\psi}^L_{i+n}$ are plotted. The resonant transition rates between right-localized states are of course identical to those between left-localized states. From the left plot in the figure it is seen that the anion rates exceed the cationic ones by roughly two orders of magnitude for all $i+1$ transitions. Such behavior was already expected from the discussion of the excited state potential surfaces above. Interestingly no linear behavior is seen for the 'harmonic' $i+1$ transitions, which was one of the assumptions of the truncated harmonic oscillator model of Walkup et al. [70] (see also Sec. 1.3). Further, non-harmonic overtone excitations are present for the actual system. Their magnitude results from the anharmonicity of the ground state potential and the non-linearity of the difference potential between ground and excited state. The importance of overtone excitations for the switching will be outlined in the following. The rates decrease, with an increasing order of the overtone transitions, by several orders of magnitude. The differences between an- and cation rates become smaller and their order is alternating. The $i+5$ and $i+6$ transitions, for example, show slightly higher rates for the cation than for the anion, while it was the other way around for $i+1$ and $i+2$ transition rates. We should keep in mind the dominance of cation, resonant overtone transitions for the further discussion.

As for the dipole scattering, the inelastic, resonant tunneling current fraction η^{res} is calculated using Eq. (2.55). Taking the rates from Fig. 4.21 for $|\Delta E_{res}| = 1\,\text{eV}$, $\tau_{res} = 1\,\text{fs}$ and

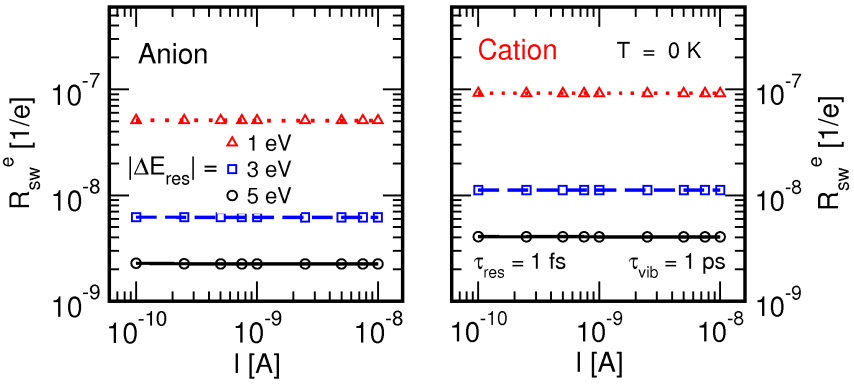

Figure 4.22: Switching rates per electron R^e_{sw} for anion and cation resonance-induced switching, versus STM current I for three different values of $|\Delta E_{res}|$. $\tau_1^{vib} = 1\,\text{ps}$, $T = 0\,\text{K}$, $\tau_{res} I = 1\,\text{fs}$.

$I = 1\,\text{nA}$, $W^{res}_{1\leftarrow 0}$ is about $1.6 \times 10^{-11}\,(\text{E}_h/\hbar)$ and $2.5 \times 10^{-13}\,(\text{E}_h/\hbar)$ for anion and cation, respectively. This would translate into an inelastic resonance tunneling current fractions η^{res} of 1.0×10^{-4} and 1.7×10^{-6}. Values of η^{res} between 1.0×10^{-4} and 4.0×10^{-2} can be found in the literature calculated for similar systems [70, 26]. The estimate for the dipole-induced inelastic tunneling fraction η^{dip} of about 1.9×10^{-5} was given in Sec. 4.3.4. Taking the calculated numbers, the anion-induced switching would be faster than the dipole-induced and both would be much faster than the cation one. However, neither a large difference for switching at positive or negative voltages nor a ladder climbing mechanism were observed by experiment [10].

Now, in the below-threshold model the question arises whether the resonance excitations allow for switching and if a ladder climbing mechanism or a one-electron process is at work. To answer this question the switching rate dependence on the STM current, for anion and cation, is plotted in Fig. 4.22. The most important information is that the switching rate per electron remains constant at all studied currents. Therefore a single-electron overtone excitation is at work. The same was already seen for the dipole component and is therefore also compatible with the experimental data [10, 145]. As expected, the rates decrease as $|\Delta E_{res}|$ increases. All rates lie above the experimentally observed switching rates of $1 \times 10^{-9}\,1/\text{e}$. Quantitative agreement can only be achieved by a reduction of both vibrational and resonance lifetime or an increase of ΔE_{res} above 5 eV, as will be discussed in the following.

The cation rates are comparable to the anion ones, which is compatible with experiment, if one assumes a resonant switching mechanism for COD@Si. To be more precise, the cation switches 1.8 times more rapidly than the anion, for all three values of ΔE_{res}. This is counter-intuitive to the stated similarity between neutral and cation surface and the low $W^{res}_{1\leftarrow 0}$ values for the cation resonance, and has to be explained in the following. Switching is driven by transition rates between the vibrational ground state and doublets $i = 5, 6$, which tunnel on the ps-timescale, as observed for the dipole-mechanism already. The corresponding, cation-derived overtone transition rates are higher than for the anion case, as seen on the right side of Fig. 4.21. The left side of Fig. 4.23 further exemplifies the

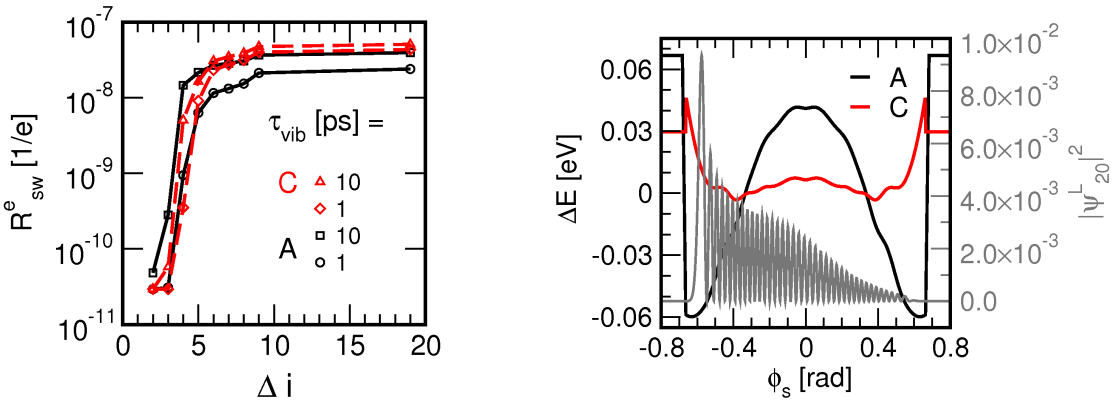

Figure 4.23: Left: Switching rate per electron R^e_{sw} for anion (A) and cation (C) resonance-induced switching, in dependence upon $n_{\max} = |f - i|$, the maximal overtone transition included. $I = 10\,\mathrm{nA}$, $\tau_{res} = 1\,\mathrm{fs}$, $|\Delta E_{res}| = 1.5\,\mathrm{eV}$. Right: Energy differences $\Delta E = V_{es} - V_{gs}$ between resonance (A/C) and neutral (N) potential energy surfaces of COD@Si(100), as shown in fig 4.9. The minima of all three surfaces are set to zero. (The 'kinks' are discussed in the text.) (A) $\Delta E = V_A - V_N$. (C) $\Delta E = V_C - V_N$. The spatial probability distribution for the 20th left localized vibrational state is shown in gray.

findings. Here, the switching rate per electron is plotted vs. the maximal overtone level $n_{\max}$. The cation switches more rapidly than the anion, only if higher overtone transitions ($n_{\max} > 4$) are included. Also, the direct excitation to the tunneling region is more efficient than ladder climbing, despite much higher $i+1$ transition rates for both anion and cation. It might be possible however, that ladder climbing dominates at higher currents $I > 10\,\mathrm{nA}$ and longer vibrational lifetimes. It is further seen that for the switching, only transitions up to $n_{\max} = 9$ are of importance. Fig. 4.23 shows energy differences between ground and resonance state potentials on the right. Additionally the spatial probability distribution of the 20th, left-localized vibrational state ψ^L_{20}, the highest state in the propagation, is plotted for exemplary purposes[3].

$|\psi^L_{20}|^2$ has its global maximum between $\phi_s = -0.5$ and $-0.7\,\mathrm{rad}$. Here the anion difference potential has its minima, while the cationic one is much steeper. It shows that 'higher' states are more 'affected' by the cation surface, than by the anionic one. The comparatively higher, overtone excitation rates for the cation and subsequent switching rates seem to have their origin in the steeper side portion of the corresponding difference potential of the cation resonance.

(3) Parameter dependencies:

In the following, the dependence of the switching rate on several parameters of the below-threshold model are tested. In Fig. 4.24, the switching rate is plotted versus the resonance lifetime. A nearly constant switching rate is seen for resonance lifetimes above 1 fs where the parameter becomes rather unimportant, while below 1 fs the dependence is strong.

[3]The kinks in the borders of the difference potential are artificial, due to numerical inaccuracies, but have no influence on the results.

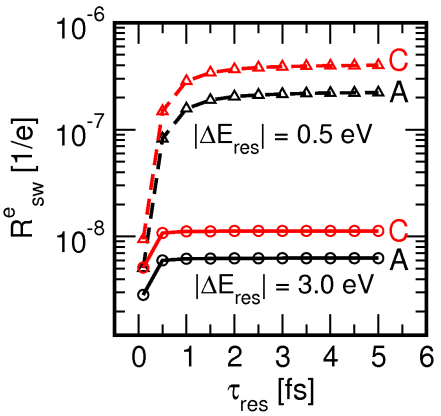

Figure 4.24: R^e_{sw} switching rate per electron, as obtained for anion (A) and cation (C) resonance as a function of the resonance lifetime τ_{res}. $\tau_1^{vib} = 1\,\text{ps}$, $I = 1\,\text{nA}$.

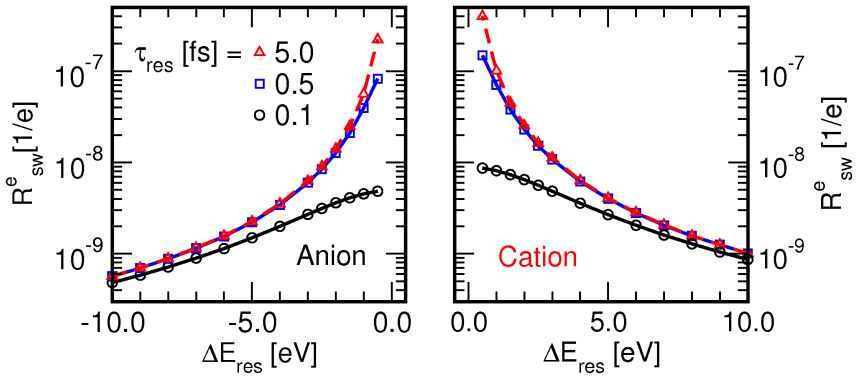

Figure 4.25: Switching rates per electron R^e_{sw} plotted versus the energy gap ΔE_{res} between Fermi level of the STM tip and adsorbate resonance center energy. $\tau_1^{vib} = 1\,\text{ps}$.

The dependence of R^e_{sw} on τ_{res} also decreases for an increasing value of $|\Delta E_{res}|$ as illustrated by Fig. 4.25. Here the switching rate is plotted versus ΔE_{res} for three different resonance lifetimes. It is seen that $|\Delta E_{res}|$ is only of minor influence on the switching rate if $\tau_{res} \leq 0.1\,\text{fs}$, which would refer to the case of a 'broad' resonance with a short lifetime, as mentioned previously. Hence, agreement between experiment (i.e., only weak U-dependence and a switching probability of $\approx 1 \times 10^{-9}$ per electron at positive and negative bias sample) and the below-threshold model is realized, assuming an short-lived resonance. Also for values of $|\Delta E_{res}|$ above 5 eV, the switching rate varies only slightly with $|\Delta E_{res}|$, independent of the resonance lifetime τ_{res}, and has the right order of magnitude. This is the second limit for voltage independent switching in the below-threshold regime, i.e., the far-off-resonance case mentioned before.

Furthermore, the vibrational lifetime dependence is tested. Fig. 4.26 shows the switching rates in dependence upon τ_1^{vib}. The left plot compares anion and cation resonance-mediated switching rates. The cation-induced resonance switching is slightly more rapid than for the anion and both curves show the same behavior up to $\tau_1^{vib} \approx 10\,\text{ps}$. Above that lifetime, the anion-mediated switching rates further increase while those for the cation remain constant until both curves cross and the anion switches more rapidly than the cation. Based on the preliminary discussion, one can argue that the cation shows a greater capacity to induce high-order overtone-transitions into fast tunneling states, compared to the

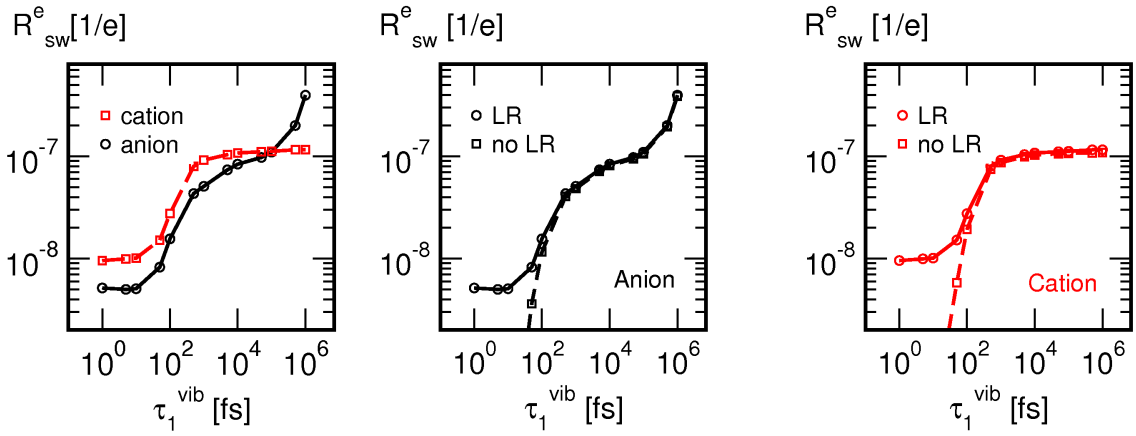

Figure 4.26: Resonance-induced switching rates per electron $R^e_{sw}\,[1/e]$ in dependence on the vibrational lifetime τ_1^{vib}. Left: Cation vs. anion resonance, all transition rates included. Center/Right: All transition rates included (LR). $L \leftrightarrow R$ transitions rates between left and right well population are set to zero (no LR). $\tau_{res} = 1\,\text{fs}$, $I = 1\,\text{nA}$, $|\Delta E_{res}| = 1\,\text{eV}$.

anion. The anion rates on the other hand exceeded the cationic ones for lower overtone transitions. The lower state tunneling is slower and therefore more affected by vibrational relaxation (dissipation) than tunneling in higher states. If the competing vibrational relaxation is weakened, tunneling via lower states gains more importance for the switching. Since the anion resonance populates such lower lying states more efficiently than the cation, its switching yield exceeds the cationic one at higher values of $\tau_1^{vib} > 100\,\text{ps}$.

Another important point is the existence of a purely rate-based switching channel, as illustrated from two plots in the middle and on the right of Fig. 4.26. The $L \leftrightarrow R$-rate-based switching becomes possible, since the states above the barrier are not perfectly localized (see also Fig. 4.10). The contribution of the purely rate-mediated switching is negligible for vibrational lifetimes τ_1^{vib} above 1 ps for both anion- and cation-resonance. Shorter lifetimes are rather unrealistic (as discussed in Sec. 1.3). Below 1 ps, however, tunneling is suppressed and $L \leftrightarrow R$ rates start to dominate switching. The latter finding explains the constant, lifetime-independent, switching rate level below $\tau_1^{vib} = 1\,\text{ps}$.

Finally, a comparison of dipole and resonance-induced switching rates is given in Fig. 4.27. The dipole component plays no role for $\tau_1^{vib} \leq 1\,\text{ps}$ but already makes a difference of $\approx 30\,\%$ at $\tau_1^{vib} = 10\,\text{ps}$. For $\tau_1^{vib} > 100\,\text{ps}$, the dipole-induced switching exceeds the resonance component. Such a long vibrational lifetime is rather improbable for COD@Si(100), because of the strong coupling to the Si-surface phonon-band. The crossing point between purely dipole and purely resonance rates is $|\Delta E_{res}|$-dependent and therefore expected to be shifted towards shorter vibrational lifetimes for an increasing value of $|\Delta E_{res}|$ and vice versa. Additionally, it is seen that the τ_1^{vib} dependence of resonance switching rates decreases with increasing $|\Delta E_{res}|$. It is also seen that the dependence on τ_1^{vib} is much weaker in Fig. 4.27 ($|\Delta E_{res}| = 5\,\text{eV}$) as compared to Fig. 4.26 ($|\Delta E_{res}| = 1\,\text{eV}$).

The temperature dependence as found for the dipole-induced switching would be repro-

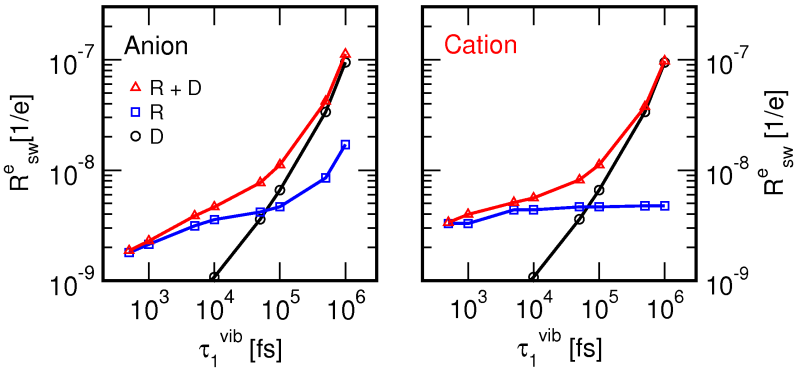

Figure 4.27: Switching rates R^e_{sw}, as resulting from purely dipole (D), purely resonance (R) or dipole and resonance (R+D)-induced switching versus the vibrational lifetime parameter τ_1^{vib}. $\tau_{res} = 1\,\text{fs}$, $|\Delta E_{res}| = 5\,\text{eV}$, $I = 10\,\text{nA}$.

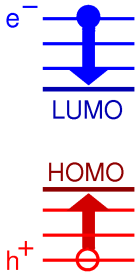

Figure 4.28: Proposed electronic relaxation scheme for STM-injected electrons (e^-) and holes (h^+) in the COD@Si(100) adsorbate system. Occupied electronic levels are shown in red, empty levels in blue.

ducible for the resonance switching model as well, since the underlying switching mechanism is identical. For both, single rate transitions and subsequent tunneling to the neighboring potential well are the dominating processes. The analysis of thermal switching is therefore not repeated explicitly for the resonance mechanism.

4.3.7 Resonance-induced switching: Above-threshold regime

(1) Introduction:

In the current section, the above-threshold regime is studied within a one-dimensional two-surface (2S1D) model. Each single electron now provides enough energy for the system to populate the resonance state. In other words, the Fermi level of the tip is above an unoccupied or below an occupied resonance state, leading to an anion or cation resonance, respectively. Fig. 2.3 shows as an example the situation for a negative ion resonance and a positive sample bias.

Electronic population and depopulation of certain resonant electronic states of the adsorbate-surface system would lead to a voltage dependent switching rate, not observed by the experiment. Therefore, Fig. 4.28 sketches a possible, physical depiction of voltage independent, resonance excitations within the above-threshold regime. The STM either injects holes $h+$ or electrons $e-$ into the occupied (red) or unoccupied (blue) electronic levels of valence- and conduction-bands of the COD@Si(100) system. Taking each electronic level as a possible resonance, the resulting resonance density of states is broad and

rather voltage independent. It is further assumed that the injected electron or hole relaxes very rapidly to the band edges (similar to the short-lived resonance scenario as discussed for the below-threshold regime). In the vicinity of the COD-adsorbate, these are further assumed to be partly composed of the HOMO and LUMO of the COD-adsorbate-surface system. The resonance lifetime of those states at the band gap is presumably longer than for states in the band. As a result, the nuclear dynamics of the COD-adsorbate is dominated by HOMO- and LUMO-based resonances.

(2) Propagation details:

In the following, some details about the algorithm used for the density matrix propagations are given. A second resonance surface is included in the density matrix propagation, as explained in Sec. 2.6. Via the resonance lifetime τ_{res}, a single exponential decay channel for an instantaneously excited wave packet is defined. For the resonance surface, no vibrational relaxation is included, because the electronic lifetime is much shorter than the vibrational lifetime. The one-dimensional potential surfaces and corresponding vibrational eigenstates of anion and cation resonance were already discussed in Secs. 4.2.3 and 4.3.1. The switching barriers are 220 meV for the anion and 185 meV for the cation and therefore rather similar to the neutral state barrier of 179 meV. Tunneling on the ps-timescale is found for the 4th doublet of the cation and for the 5th doublet of the anion state. 30 vibrational states are included for the anion and cation resonance state in the propagations, while 40 states are included for the electronic ground state, as before. The number of states is sufficient to achieve adequate conservation of norm and initial localization for an upward-projected, localized vibrational ground state wave function, by which the initial excitation step is modeled. For example after a consecutive, upward-downward projection a wave packet localization error below 1×10^{-10} and a loss of norm smaller than 5×10^{-10} is obtained.

At this point, it is important to recall the definition of the switching rate per electron R_{sw}^{e} for the two-surface propagations, as given in Eq. (2.75). Since all propagations start on the resonant surface and the electronic excitation probability W_{exc} is neglected, only the switching yield per resonant excitation event $R_{sw}^{e'}$ can be calculated. $R_{sw}^{e'}$ is simply defined as the final electronic ground state population of the right well, if the propagation started in the left well of the resonant surface and vice versa, multiplied by $W_{exc} = I_r/I$, as shown in Eq. 2.75. I_r/I accounts for the fraction of overall, measurable tunneling electrons which travel via the COD-adsorbate resonance. Unfortunately, the ratio I_r/I is unknown for the actual system. Instead, the I_r/I ratio for the resonance-driven intra-dimer switching of H@Si(100) of $\approx 1 \times 10^{-3}$ is taken [32]. But, the 'real' ratio I_r/I of the system might differ from this value. A strict quantitative comparison of theoretical and experimental switching rates per electron is therefore not possible. Nevertheless, it is possible to study the mechanism of a possible resonant switching process, including all parameter dependencies (τ_1^{vib}, τ_{res}). Also the experimentally observed equality of switching at positive and negative sample bias can be examined. Finally, it will be shown that the reproduction

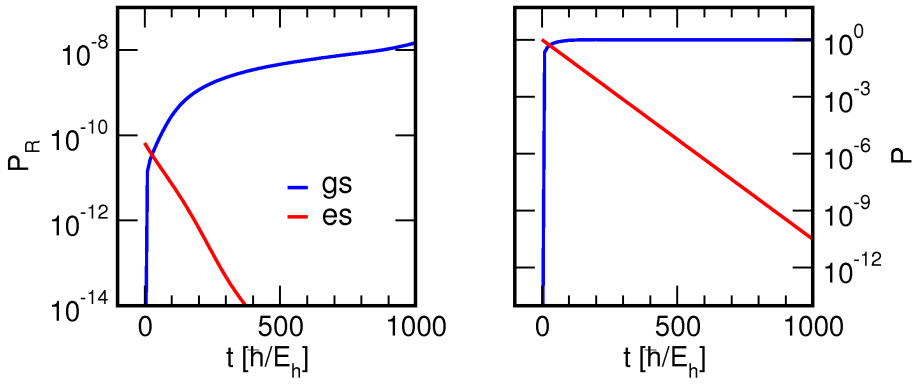

Figure 4.29: Left: Population in the right well (P_R) of the electronic ground state (gs) and the resonance, electronically excited state (es) versus propagation time t. Right: P: Total population for ground state (gs) and excited state (es) surfaces. The propagation started with 100 % population in the left well of the excited state potential. $\tau_{res} = 1$ fs, $\tau_1^{vib} = 1$ ps.

of experimentally observed switching yields is possible for a reasonable set of parameters, with the choice $I_r/I = 1 \times 10^{-3}$.

(3) Switching mechanism:

As an example, we illustrate the above-threshold 2S1D model for the anion resonance in the following. The propagation started with the left-localized vibrational ground state $\tilde{\psi}_0^L$ (see Eq. (2.10)) projected to the anion resonance state with a resonance lifetime set to 1 fs. From the plotted norm in the right graph of Fig. 4.29 it is seen that the resonance population nearly completely decays back to the electronic ground state, within the first 1000 atomic time units or ≈ 25 fs. The left graph in Fig. 4.29 shows the population of the right potential well of electronic ground state and of the resonance as a function of time. It is seen that the population of the right well of the resonant state (originating from the initial localization error) is steadily decreasing. In the same time the population in the right well of the electronic ground state is increasing.

Therefore, no switching takes place on the resonance surface and it can be concluded that the wave packet only gains the kinetic energy there in order to switch in the neutral ground state. Since the same switching mechanism is observed for the cation resonance, it will not be discussed in detail here.

(4) Parameter dependencies:

The parameter dependencies of the 2S1D switching rates are tested in the following. Here, a special focus lies on the comparability between below-and above-threshold regimes, i.e., 1S1D and 2S1D models. While the resonant excitation in the 1S1D model is explicitly modeled by perturbation theory, propagation in the 2S2D model already starts from an electronically excited wave packet. Here, the resonance state provides the kinetic energy

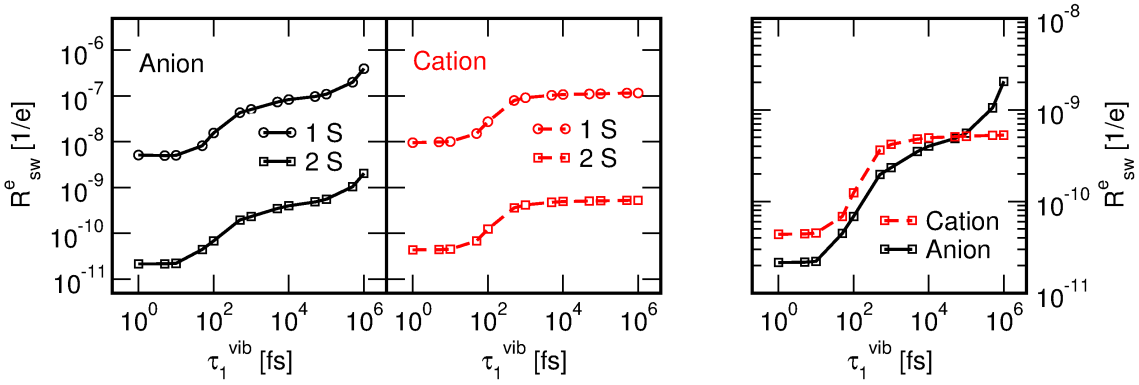

Figure 4.30: Left: Resonance-induced switching rates per electron R^e_{sw} as calculated for one- (1 S) and two-surface (2 S) models with respect to the vibrational lifetime parameter τ_1^{vib}. Right: Comparison of 2 S switching rates as obtained for anion and cation resonance. $\tau_{res} = 1$ fs. Additional 1 S-parameters: $I = 1$ nA, $|\Delta E_{res}| = 1$ eV.

for the wave packet in order to switch in the electronic ground state, after electronic relaxation. Therefore, in both models the switching takes place in the ground state and a qualitative agreement between both models is expected. The dependence of R^e_{sw} on the vibrational lifetime τ_1^{vib} is plotted in Fig. 4.30. Here, the expected qualitative agreement between both models can be observed. It is seen that switching for both models, 1S1D and 2S1D, is driven by the same mechanism, namely the tunneling of vibrationally excited, electronic ground state population. Within the 1S1D model, 'lower' vibrational states are populated more effectively via the anion- than via the cation-resonance, while for 'higher' vibrational states it is the other way around. This manifests itself also in a different behavior of anion and cation resonance regarding the switching rates with respect to τ_1^{vib}. The same qualitative behavior for anion and cation is seen for the 2S1D model, here. It can be concluded that also the same excited vibrational levels of the electronic ground state are populated via anion- and cation-resonances, for both models. An example of qualitative equivalence between both models is shown for the vibrational lifetime dependence in in the right half of Fig. 4.30. Here, the cation resonance induces faster switching than the anion for $\tau_1^{vib} < 5 \times 10^4$ fs, as already discussed for the 1S1D model.

The two plots in the left part of Fig. 4.30 also show that the 1S1D rates are higher than the 2S1D rates, depending of course on the chosen ratio I_r/I. At first, similar switching yields for anion and cation have been found for 2S1D as well as for 1S1D in accordance to the experimental findings. However, for the chosen ratio $I_r/I = 1 \times 10^{-3}$ the 2S1D switching rates are lower by two orders of magnitude than those for 1S1D and correspond, within an order of magnitude, to the experimental switching yield of 1×10^{-9} 1/e, if τ_1^{vib} is in the realistic range of ≈ 1 ps. It was already mentioned that the perturbative rate formula (Eq. (2.52)), used for the 1S1D model, only gives an 'order of magnitude' estimate for the vibrational excitation due to the inelastic tunneling current fraction. Therefore a quantitative agreement of 1S1D and 2S1D models can not be expected. The 1S1D, below-threshold, rate-based model possibly overestimates the density of states for the resonance and therefore the inelastic tunneling current fraction. For $|\Delta E_{res}| = 1$ eV the situation of

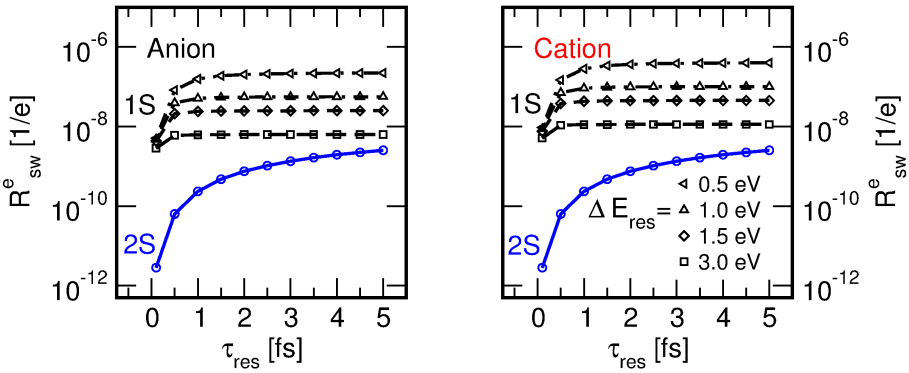

Figure 4.31: Comparison of resonance-induced switching rates per electron R^e_{sw}, calculated for the 1S1D and 2S1D models, with respect to the resonance lifetime τ_{res} for different ΔE_{res}. $\tau_1^{vib} = 1\,\text{ps}$. Additional 1 S-parameter: $I = 1\,\text{nA}$.

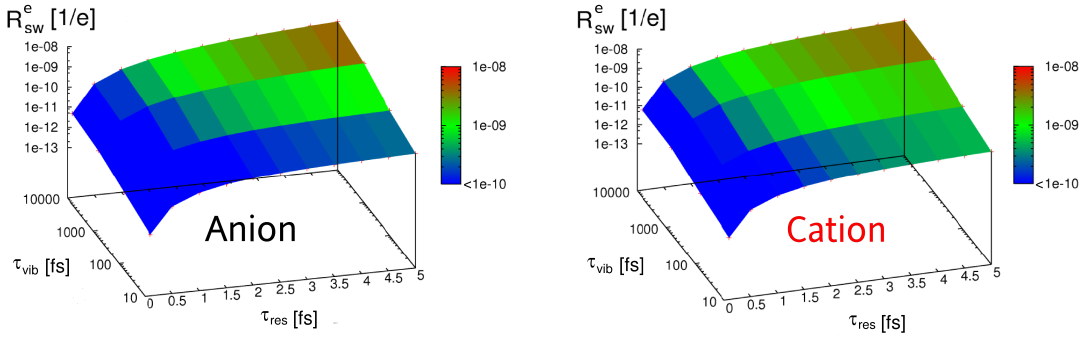

Figure 4.32: Comparison of switching rates per electron R^e_{sw} calculated for anion and cation resonance and the 2S1D model, as functions of vibrational lifetime τ_1^{vib} and resonance lifetime τ_{res}.

a resonance 'close' to the tip Fermi level might also violate the weak perturbation limit of Fermi's Golden Rule.

Fig. 4.31 focuses on the comparability of 1S1D and 2S1D model, regarding the dependence on the resonance lifetime τ_{res}. It is seen immediately that the 2S1D model has a higher sensitivity with respect to τ_{res} than the 1S1D model. In the range between τ_{res} =0.1 to 10 fs, the rates change by four orders of magnitude for the 2S1D model but only by two orders of magnitude for the 1S1D model ($|\Delta E_{res}| = 0.5\,\text{eV}$). Also no constant R^e_{sw} is seen above $\tau_{res} \approx 1\,\text{fs}$ for 2S1D, as it is for 1S1D. The 2S1D model therefore differs from the simpler 1S1D estimate also qualitatively in the description of the τ_{res} dependence. Since the dynamics at the resonance surface are only covered by the 2S1D model, gaining naturally more importance for extended resonance lifetimes, this result was expected.

Taking the factor $I_r/I = 1 \times 10^{-3}$ as realistic for the system, one finds good quantitative agreement between calculated and experimentally obtained switching yields of 1×10^{-9} per electron, for a reasonable set of parameters. The calculated values of R^e_{sw} in 1/e versus parameters τ_{res} and τ_1^{vib} are shown for anion and cation resonance on the left and right side of Fig. 4.32, respectively. The regions plotted in green indicate quantitative agreement between experiment and calculation. Anion and cation-induced switching rates are in a

proper range for vibrational lifetimes between 1 to 10 ps and resonance lifetimes around 2 fs. Another window of good agreement opens up at $\tau_{res} \approx 5.0$ fs and $\tau_1^{vib} \approx 0.5$ ps for the anion and at at $\tau_{res} \approx 3.0$ fs and $\tau_1^{vib} \approx 0.5$ ps for the cation, respectively.

4.3.8 Summary

Finally the main results for the one-dimensional, 1S1D (below-threshold) and 2S1D (above-threshold) scattering models are summarized. For the first model, two contributions, namely dipole and resonance scattering were included. The dipole mechanism accounts for the experimentally obtained, linear current dependence of switching rates R_{sw}^t and the measured switching yield per electron of 1×10^{-9} 1/e. The switching mechanism is based on overtone-transitions as included in extension to the harmonic, linear perturbative rate model of Persson et al. [25]. The voltage-independence is naturally a characteristic of the dipole mechanism. For the dipole model a temperature-dependent crossover between a quantum tunneling and a classical Arrhenius regime was predicted. The calculations motivated further temperature dependent STM measurements, which confirmed the calculated crossover temperature [151].

For resonance scattering, anion and cation resonances were taken into account and based on the LUMO and HOMO orbital levels by applying Koopmans' theorem. The below-threshold regime of resonant switching was examined by extending the harmonic, linear model for the resonance inelastic current fraction of Persson et al. [26], and calculating corresponding vibrational excitation and de-excitation rates. Generally, qualitative agreement with experiment was observed, e.g., a single-electron mechanism and similar switching rates for anion and cation resonance. Quantitative agreement in terms of switching yield and voltage independence could only be achieved for the limiting cases of a far-off-resonance ($|\Delta E_{res}| > 5$ eV) and a broad, short-lived resonance ($\tau_{res} < 0.5$ fs).

Both dipole and resonance-mediated switching in the 1S1D model could therefore rationalize the experimental results. For the dipole-scattering-induced switching a vibrational lifetime τ_1^{vib} of 10 ps was chosen in order to reproduce the experimental switching yield, while it was set to 1 ps for the resonance mechanism.

Taking into account an additional resonance state surface for the density matrix propagation in the 2S1D model, the resonance switching in the above-threshold/ non-perturbative limit was analyzed and compared to the 1S1D results. Again, agreement with experiment was achieved within a reasonable parameter range of vibrational and resonance lifetimes. The qualitative findings for the 1S1D model, such as switching via tunneling in the ground state and vibrational lifetime dependence, could be affirmed.

4.4 Two-dimensional density matrix propagation

So far, the switching of COD was approximated as a one-dimensional, symmetrical and opposite rotation of two $(CH_2)_2$-units of COD@Si(100), along the collective switching

coordinate ϕ_s. We will now study the switching, including a second mode. The second collective switching coordinate ϕ_u as introduced earlier describes an unsymmetrical rotation of both $(CH_2)_2$-units. Its inclusion allows the system to switch along its real transition states (TS) at $\phi_s = 0\,\text{rad}$ and $\phi_u = 0.309\,\text{rad}$, as found for the potential surfaces calculated by Dokić et al. [143] (see Sec. 4.2). The TS is 9 meV lower in energy than the former 1 D transition state (see Sec. 4.2). Additionally, the 2 D dipole function and the 2 D resonance state potentials are utilized in the following. Therefore, the validity of the 1 D approach tested via the results obtained for the 2 D model, for single-surface (1S2D) and two-surface propagations (2S2D). In the following all wave functions (ϕ, φ) are understood as two-dimensional states depending on both coordinates ϕ_s and ϕ_u, independent of their previous definitions.

This section is organized as follows. First, the 2 D state functions for neutral and resonance surfaces are presented as well as technical details about state localization and the density matrix propagation for 2 D states. Afterwards, the Ohmic bath dissipative model, as introduced for one-dimensional vibrational states in Sec. 2.5.2, is extended to two dimensions. In analogy to previous sections, thermal-, dipole- and resonance-induced switching rates are calculated and compared to previous 1 D. In order to account for the contribution of inelastic, resonance scattering, the below- and above-threshold scenarios are tested as well.

4.4.1 Vibrational eigenstates

The Fourier Grid Hamiltonian (FGH) method is used to obtain the 2 D vibrational eigenstates, represented in a spatial grid basis. Accordingly, a product ansatz of two Dirac-like basis functions is chosen, in order to represent 2 D eigenstates $\psi_{m/n}(\phi_s, \phi_u)$, for a two-dimensional (2 D) potential surface $V(\phi_s, \phi_u)$, on a spatial grid with basis functions $\varphi_{i/l}(\phi_u)$ and $\varphi_{j/k}(\phi_s)$.

$$|\psi_m\rangle = \sum_{ij} c_{ij,m} |\varphi_i\rangle|\varphi_j\rangle \qquad \text{and} \qquad |\psi_n\rangle = \sum_{kl} c_{kl,n} |\varphi_k\rangle|\varphi_l\rangle \qquad . \tag{4.14}$$

The resulting 2 D Fourier Grid Hamilton matrix elements H_{ijkl} are defined as,

$$\begin{aligned} H_{ijkl} &= \langle\psi_m|\hat{H}|\psi_n\rangle = \langle\varphi_i|\langle\varphi_j|\hat{T} + V(\phi_s, \phi_u)|\varphi_k\rangle|\varphi_l\rangle \\ &= \langle\varphi_j|\hat{T}_s|\varphi_k\rangle\delta_{il} + \langle\varphi_i|\hat{T}_u|\varphi_l\rangle\delta_{jk} + V(\phi_s, \phi_u)\delta_{jk}\delta_{il} \qquad , \end{aligned} \tag{4.15}$$

if ϕ_s and ϕ_u are uncoupled in $\hat{T} = \hat{T}_s + \hat{T}_u$. Parameters used for the FGH method are listed in Tab. 4.10. The chosen values for potential cutoff energy, grid extension and number of grid points are found to be sufficient in order to resolve more than 1000 states ψ_m or 250 quartets $\psi_p^{A_1,A_2,B_1,B_2}$ on each of the three surfaces. Each state belongs to one of the four irreducible representations (A_1, A_2, B_1, B_2) of the C_{2v} point group. Eigenenergies E_m of 800 unlocalized states obtained for neutral (N), anion (A) and cation (C) state surfaces are plotted in Fig. 4.33. For the sake of comparability, anion and cation state energies in the plot are shifted by -3220 meV and -1590 meV, respectively, corresponding to the gauge

grid boundaries, ϕ_s [rad]:	± 0.8
grid boundaries, ϕ_u [rad]:	± 1.6
number of grid points:	150×150
moment of inertia, I_s [m_e]:	218952.18
moment of inertia, I_u [m_e]:	54738.045
potential cutoff [eV]:	≈ 1.3

Table 4.10: FGH parameters used for the calculation of 2 D vibrational eigenstates of COD on Si(100), utilizing the two-dimensional, neutral, anion and cation state surfaces.

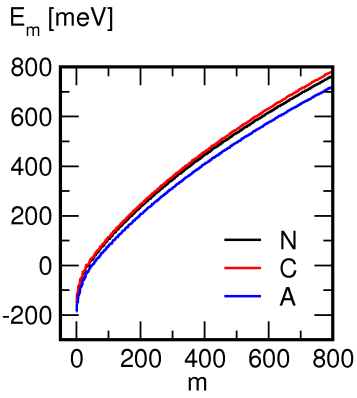

Figure 4.33: Energies E_m of $m = 1 \cdots 800$ unlocalized states as obtained via the Fourier Grid Hamiltonian (FGH) method (see above) for neutral (N), anion (A) and cation (C) potential state surfaces of COD@Si(100) (see Sec. 4.2). For the sake of comparability, anion and cation state energies are shifted by -3220 meV and -1590 meV, respectively ($V_N(\phi_s = \phi_u = 0) = V_A(\phi_s = \phi_u = 0) = V_C(\phi_s = \phi_u = 0) = 0$).

($V_N(\phi_s = \phi_u = 0) = V_A(\phi_s = \phi_u = 0) = V_C(\phi_s = \phi_u = 0) = 0$). The state energies in the left reveal qualitative information about the system. For all three surfaces approximately 40 states with energies below the energy of the potential maximum at $\phi_s = \phi_u = 0$ are found. For all three surfaces an energy range of ≈ 900 meV is covered by the first 750 states, which have been included as a maximum for each surface during all propagations. It is further seen from the plotted energies, that all three surfaces are rather equal in shape. The anion potential differs a bit more from the neutral surface (higher barrier), than the cationic one, as already discussed in the 1 D section on page 78.

4.4.2 Technical details

(1) Vibrational state localization in two dimensions:

By means of the FGH (see Sec. 2.2) N quartets of unlocalized 2 D wave functions $\psi_p^{A_1,A_2,B_1,B_2}(\phi_s, \phi_u)$ are obtained, for the $2\,D$ potential surfaces showing C_{2v} symmetry, which transform like A_1, A_2, B_1 and B_2. They have amplitudes on the left- *and* right-hand side of the potential-centered switching barrier (see Fig. 4.34). Localization to the left or right of the switching barrier, as needed for our dissipative model (see Sec. 2.4.5), is achieved via the following linear combinations for each quartet,

$$\begin{aligned} \tilde{\psi}_{n=2\cdot p}^{L,R} &= \frac{1}{\sqrt{2}}\left(\psi_p^{A_1} \pm \psi_p^{B_1}\right) \qquad \text{and} \\ \tilde{\psi}_{n=2\cdot p+1}^{L,R} &= \frac{1}{\sqrt{2}}\left(\psi_p^{A_2} \pm \psi_p^{B_2}\right) \qquad , \end{aligned} \tag{4.16}$$

resulting in four localized states or two localized state doublets $\tilde{\psi}_n^{L,R}$ ($\forall p = 0, \ldots, N$). Left-localized states have their spatial probability maximum at $\phi_s < 0$, right-localized

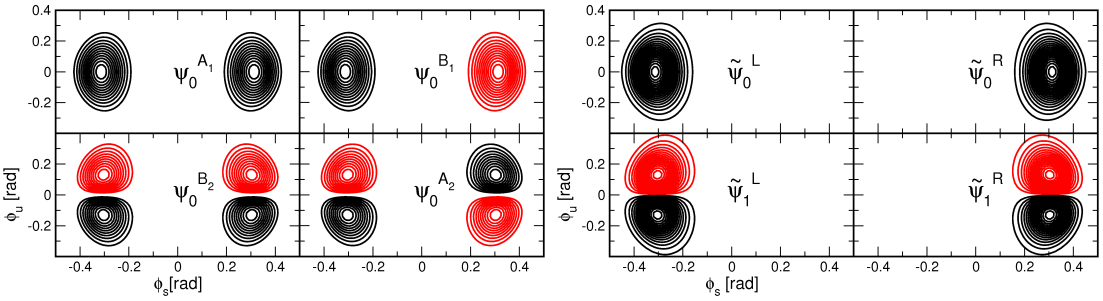

Figure 4.34: Quartet $\psi_0^{A_1,A_2,B_1,B_2}$ of 2 D unlocalized states and doublets $\tilde{\psi}_0^{L,R}$, $\tilde{\psi}_1^{L,R}$ of localized states as obtained for the neutral ground state potential of COD@Si (see Sec. 4.2.1).

states at $\phi_s > 0$. Fig. 4.34 shows the first quartet of unlocalized $\psi_0^{A_1,A_2,B_1,B_2}$ and localized wave functions $\tilde{\psi}_0^{L_1,L_2,R_1,R_2}$, respectively, as an example.

The absolute value of the wave function between the potential center, i.e., the center of the switching barrier and the 'left' grid border, along the switching coordinate ϕ_s is taken as a measure for the corresponding degree of localization to the left, Q_n^L. The corresponding integral for localized state $\tilde{\psi}_n^L$ is given as,

$$Q_n^L = \int_{-\infty}^{0}\int_{-\infty}^{+\infty} \left|\tilde{\psi}_n^L(\phi_s,\phi_u)\right|^2 \quad . \tag{4.17}$$

According to the definition in Eq. (4.16), the relation $Q_n^L = Q_n^R$ holds true as in the case of 1 D localized states (Eq. (2.12)).

The localized state energies are calculated in analogy to Eq. (2.11) as,

$$\begin{aligned} E_{n=2\cdot p}^L = E_{n=2\cdot p}^R &= \frac{1}{2}\left(E_p^{A_1} + E_p^{B_1}\right) \qquad \text{and} \\ E_{n=2\cdot p+1}^L = E_{n=2\cdot p+1}^R &= \frac{1}{2}\left(E_p^{A_2} + E_p^{B_2}\right) \quad . \end{aligned} \tag{4.18}$$

It has to be mentioned that after the FGH diagonalization, the states are ordered with respect to their energy and not with respect to their suitable localization partners. Therefore, an algorithm is used to allocate appropriate partners for localization. The highest localizability can be achieved only for the 'correct' partners, which is the selection criterion used in the localization algorithm. Finally, the localized functions are sorted with respect to their energies $E_n^L = E_n^R$.

For all doublets of localized states $\tilde{\psi}_n^{L,R}$ tunnel splittings ΔE_n are defined as,

$$\Delta E_{n=2\cdot p} = E_p^{A_2} - E_p^{B_2} \qquad \text{and} \qquad \Delta E_{n=2\cdot p+1} = E_p^{A_1} - E_p^{B_1} \quad . \tag{4.19}$$

The corresponding tunneling times are calculated accordingly via,

$$T_n = (\pi\hbar)/\Delta E_n \quad . \tag{4.20}$$

Tunneling times T_n and degrees of localization Q_n^L for 375 localized state doublets are plotted in Fig. 4.33, for neutral (N), anion (A) and cation (C) state surfaces, respectively.

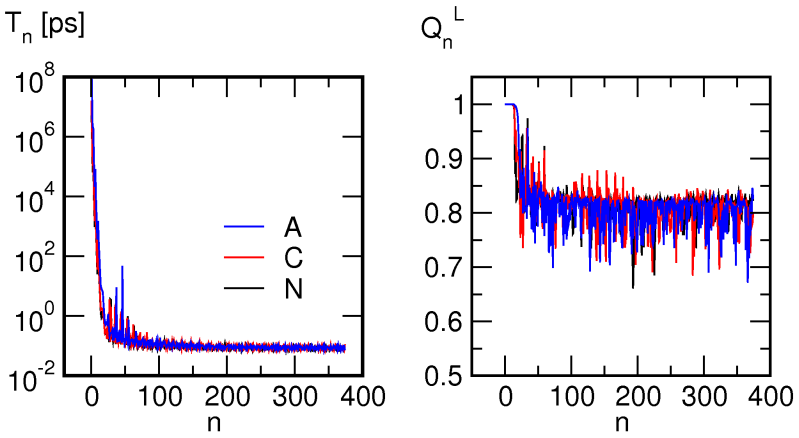

Figure 4.35: Tunneling times T_n in ps and degree of localization Q_n^L as calculated via Eq. (4.20) and Eq. (4.17), respectively, for left-localized states of neutral (N), anion (A) and cation (C) states of COD@Si(100).

The corresponding tunneling times T_n start in the μs-range and decay to ≈ 0.1 ps within the first 20 doublets. The state localizability is better than 80 % up to doublet 20 and oscillates by ± 10 % around that value afterwards. The final behavior of T_n and Q_n^L does not change for localized state doublets up to $n = 375$. The oscillations in both, T_n and Q_n^L, are partly due to the resorting of the localized states according to their energies $E_n^{L,R}$, as mentioned before.

(2) Calculation of switching rates in two dimensions:

As formulated for 1 D in Sec. 2.7, the switching rate per time R_{sw}^t is defined as,

$$R_{sw}^t = -\frac{dP_L(t)}{dt} = \frac{dP_R(t)}{dt} \quad , \tag{4.21}$$

where $P_{L,R}(t)$ are the overall populations of 'left' and 'right' oscillator well, respectively. P_L is obtained via the application of the following projection operator (see Eq. (2.71)),

$$\hat{P}_L(t) = \sum_{k=1}^{K/2} \sum_{l=1}^{L} |\varphi_k\rangle|\varphi_l\rangle\langle\varphi_k|\langle\varphi_l| \quad , \tag{4.22}$$

resulting in the following equation,

$$\left\langle \hat{P}_L(t) \right\rangle = \sum_{n,m} \rho_{nm}(t) \sum_{k=1}^{K/2} \sum_{l=1}^{L} c_{klm} c_{kln} \quad , \tag{4.23}$$

summing over half the grid along the switching coordinate (ϕ_s) and the full grid along the second coordinate (ϕ_u). The probability of right-localization is $P_R(t) = 1 - P_L(t)$

(3) Density matrix propagation in two dimensions:

As for the 1 D propagations of the density matrix (see Sec. 4.3.2), a 4th order Runge-Kutta integrator is used. The time step is set to 50 $\hbar/\mathrm{E}_h$ and 30 $\hbar/\mathrm{E}_h$ for one- and two-surface

calculations, respectively. The propagation time for all single-surface calculations is set to about $3 \times \tau_1^{vib}$. 200 unlocalized states $\psi_p^{A_1,A_2,B_1,B_2}$ or 100 localized doublets $\tilde{\psi}_1^{L,R}$ are included for all 1S2D propagations and 750 unlocalized states or 375 localized doublets on ground state and resonance surface for the 2S2D propagations, respectively.

As explained in section 4.3.2 for the 1 D case, the tunnel splitting for the lowest doublet ΔE_0 is set to zero for all propagations, to avoid tunneling on the μs timescale. In reality, the slow tunneling should be suppressed by environmental noise.

For the 2S2D propagation some additional measures are taken, in order to reduce the propagation time. After the rapid electronic relaxation of the resonance population, the excited state surface is excluded from the propagation. To further reduce the propagation time, the number of off-diagonal elements being considered in the electronic ground state density matrix is adapted dynamically during the propagation. Off-diagonal elements $\rho_{nn\pm1}$, connecting individual states of localized doublet pairs are important for the description of tunneling. Other off-diagonal elements ρ_{mn}, outside the 'first' line of off-diagonal elements in the electronic ground state result from the electronic decay of the resonance state population. Fortunately, these elements decay according to the vibrational relaxation, since here no coherence-creating processes are included. Accordingly, off-diagonal elements are excluded from the propagation below a threshold for their absolute value of 1×10^{-12}. During the relaxation also the number of populated states decrease. Since no rate-based upward processes are included for the 2S2D model, the maximal range of a single rate transition is dynamically adopted to the highest state which has population above 1×10^{-12}.

4.4.3 Ohmic bath dissipative model

For the 1 D calculations, the harmonic, bilinear dissipative model, as introduced in Sec. 4.3.3, was used. This model does not allow for $L \leftrightarrow R$ transitions and the rates scale linearly with the state number i. For 2 D, a clear assignment of quantum numbers along ϕ_s and ϕ_u is not possible for states above the barrier. Therefore, a simple linear scaling law is not applicable for a calculation of 2 D vibrational state lifetimes. Instead, the calculation of state-resolved vibrational relaxation rates is performed via the Ohmic bath model, as introduced for 1 D in Sec. 2.5.2. In the following, the extension to two dimensions is briefly presented.

Initial and final vibrational system states $\psi_{i,f}(\phi_s, \phi_u)$ depend upon two spatial coordinates ϕ_s and ϕ_u, now. Also, the former 1 D bilinear coupling operator of single-phonon excitation form in Eq. (2.35) is adopted to two dimensions,

$$\hat{V}_{sb} = (\lambda_{b,s} \cdot \phi_s + \lambda_{b,u} \cdot \phi_u) \cdot Q_b \qquad , \tag{4.24}$$

where $\lambda_{b,s/u}$ denote the vibration-phonon coupling constants between system modes $(s, u,)$ and bath oscillator $\chi_b(Q_b)$. Since the product of system and bath states is separable (see

Eq. (2.33)), the general dissipative rate Eq. (2.34) can be rewritten as,

$$W^{vib}_{f\leftarrow i} = \frac{2\pi}{\hbar}\sum_{b=1}^{N} |\langle\psi_f|\lambda_{b,s}\cdot\phi_s + \lambda_{b,u}\cdot\phi_u|\phi_i\rangle|^2 \cdot |\langle\chi^1_b|Q_b|\chi^0_b\rangle|^2 \cdot \delta(\hbar\omega_b - \hbar\omega_{if}) \quad , \quad (4.25)$$

where, ω_b and ω_{if} are the frequencies of bath phonons and system vibrations, respectively. Again, a bath at 0 K is assumed and only single phonon transitions are allowed. Therefore, only the ground and first excited bath oscillator states, χ^0_b and χ^1_b, are considered. The Ohmic phonon-bath has an equidistant frequency spacing between the N bath oscillators, $\omega_b = b\cdot\Delta\omega = b\cdot\tilde{\nu}_{cut}\cdot c\cdot h/N$, where c is the speed of light and $\tilde{\nu}_{cut}\cdot c\cdot h$ the cutoff energy. Further, the definition of the coupling constants $\lambda_{b,s/u}$ are chosen as [102],

$$\lambda_{b,s/u} = b\left(\frac{2M_b\, I_{s/u}\,\gamma_{s/u}\,(\Delta\omega_b)^3}{\pi}\right)^{1/2} \quad , \quad (4.26)$$

with the moments of inertia $I_{s/u}$. In Sec. 2.5.2 it was shown, within the harmonic wide-band and continuum limit, that the coupling parameter $\gamma = 1/\tau^{vib}_1$. Further we choose $\gamma_s = \gamma_u = \gamma$ for all 2 D calculations. Assuming a harmonic bath, one can use the analytic solution for the corresponding matrix elements, $\langle\chi^1_b|Q_b|\chi^0_b\rangle = \sqrt{(\hbar/2\,M_b\,\omega_b)}$. Applying the above definition of $\lambda_{b,s/u}$, Eq. (4.25) becomes if Lorentzian broadening is assumed for the $\delta - functions$:,

$$W^{vib}_{f\leftarrow i} = 2\,|\langle\psi_f|\sqrt{I_s}\phi_s + \sqrt{I_u}\phi_u|\psi_i\rangle|^2\cdot\gamma\cdot\Delta\omega_b\cdot\sum_{b=1}^{N}\omega_b\cdot\frac{1}{\pi}\cdot\frac{\gamma_L}{\gamma_L^2 + (\hbar\omega_b - \hbar\omega_{if})^2} \quad . \quad (4.27)$$

The 2 D Ohmic bath rate model includes four parameters, namely the number of bath oscillators N, the cutoff 'energy' $\tilde{\nu}_{cut}$, and the Lorentzian width γ_L. $\tilde{\nu}_{cut}$ is set to 530 cm^{-1} for all calculations (see Sec. 1.3). The two other parameters, n and γ_L, will be considered shortly. γ is chosen such, that for the calculation of $W^{vib}_{0\leftarrow 1}$ via Eq. (4.27) the condition $W^{vib}_{0\leftarrow 1} = 1/\tau^{vib}_1$ is fulfilled. Eq. (4.27) is the working equation for relaxation rates between 2 D vibrational states of COD@Si. Thermal heating and corresponding vibrational upward rates are calculated via the condition of detailed balance, as defined in Eq. (2.40). In Appendix F additional information about the calculation of coupling matrix elements is given.

(1) Parameter testing: One-dimensional model

In the following the 1 D results for the harmonic, bilinear and the Ohmic bath dissipative models (see Sec. 2.5.2) are compared to each another. First, the convergence of the 1 D Ohmic bath parameters is considered. Fig. 4.36 shows three plots for switching rate dependencies on $\tilde{\nu}_{cut}$, γ_L and N. The vibrational dissipation parameter τ^{vib}_1 is set to 1 ps, here. The plots show switching rates R^t_{sw} for the dipole mechanism (in blue) at 10 nA, as an example of IET-induced switching, and the purely temperature-induced switching (in black) at 150 K.

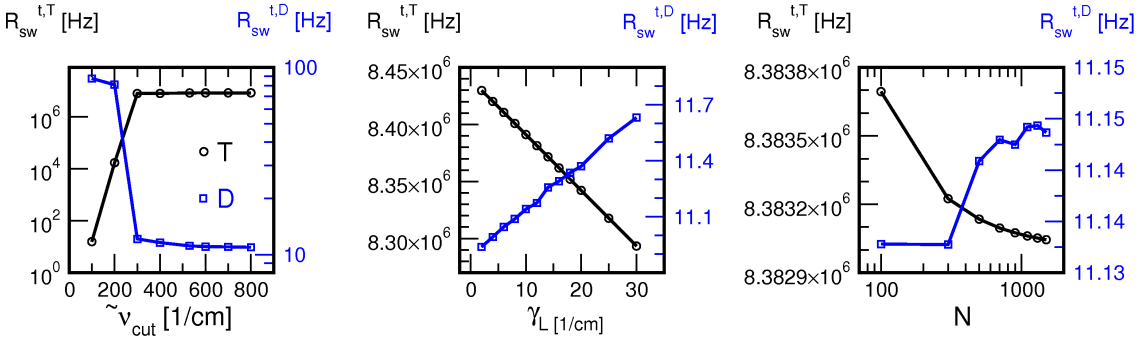

Figure 4.36: Switching rates R_{sw}^{t} [Hz] obtained for 1S1D propagations, using one-dimensional vibrational states depending on Ohmic bath parameters. Default parameters: $\tilde{\nu}_{cut} = 530\,\mathrm{cm}^{-1}$, $\gamma_L = 10\,\mathrm{cm}^{-1}$, $N = 500$. Left: Dependence upon the Ohmic bath cutoff frequency $\tilde{\nu}_{cut}$. Center: Dependence upon the Lorentzian width of single surface-bath oscillators γ_L. Right: Dependence upon the number of bath oscillators N. Black circles: Switching rates $R_{sw}^{t,T}$ [Hz] for temperature-induced switching. $T = 150\,\mathrm{K}$, $\tau_1^{vib} = 1\,\mathrm{ps}$. Blue squares: Switching rates $R_{sw}^{t,D}$ [Hz] for dipole-induced switching. $I = 10\,\mathrm{nA}$, $\tau_1^{vib} = 1\,\mathrm{ps}$, $T = 0\,\mathrm{K}$.

$\tilde{\nu}_{cut}$ [cm^{-1}]	530
γ_L [cm^{-1}]	10
N	500

Table 4.11: Ohmic bath parameters, chosen for 1 D calculations of dissipative population transfer rates, between 1 D vibrational levels of COD@Si(100).

The switching rates are nearly constant beyond $\tilde{\nu}_{cut} = 300\,\mathrm{cm}^{-1}$ for both temperature- and dipole-induced switching. Therefore, using a cutoff at $530\,\mathrm{cm}^{-1}$ is unproblematic, since all important vibrational quanta of the system can be transferred between adsorbate and bath in that frequency range. The switching rates show a weak linear correlation with respect to the energetic width γ_L in a range between 1 to $30\,\mathrm{cm}^{-1}$. The parameter is not of great influence on the switching rates of our COD@Si model and γ_L is set to $10\,\mathrm{cm}^{-1}$ for all our calculations. No large dependency of switching rates on the number of oscillators N is seen either, as shown in the last plot. N has to be large enough to ensure frequency independent damping, which is the definition of the Ohmic bath. A value of $N = 500$ is sufficient in the 1 D case. Table 4.11 again summarizes the Ohmic bath parameters used for all 1 D calculations.

(2) Comparison of Ohmic and harmonic, bilinear bath model:

A comparison of both dissipative models, showing switching rates for dipole-, thermally- and anion resonance-induced switching, is shown in Fig. 4.37. In each graph no major differences are observed for vibrational lifetimes τ_1^{vib} above 10 ps. Therefore, the earlier discussion about the switching process in the one-dimensional, single-surface model is also valid for the dissipative Ohmic bath model.

Contrary to the bilinear, harmonic dissipative model, the Ohmic bath approach allows for overtone and $L \leftrightarrow R$ transition, increasing the switching yield by maximally 30 %. Considering the small changes, as compared to the harmonic, bilinear dissipative model, these

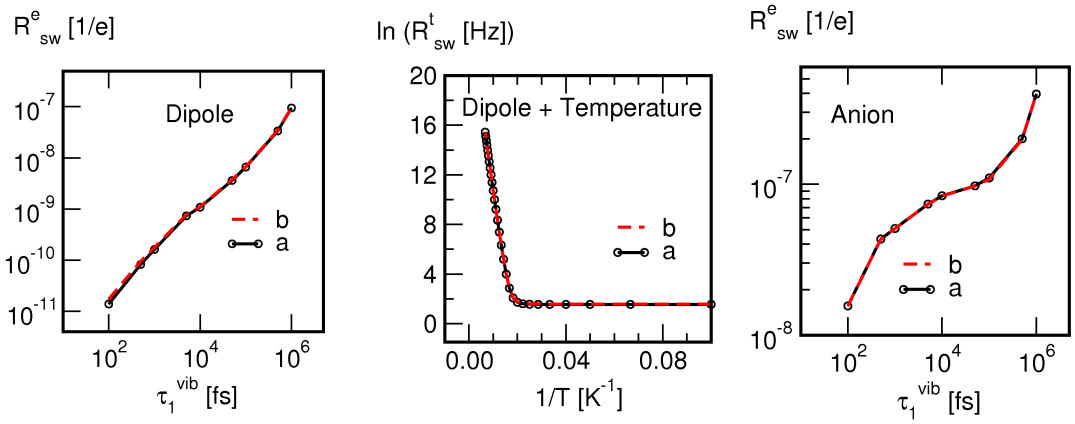

Figure 4.37: Comparison of 1 D switching rates R^e_{sw} [1/e] for (a) harmonic, bilinear and (b) Ohmic bath dissipative models, respectively. Default Ohmic bath parameters: $\tilde{\nu}_{cut} = 530\,\mathrm{cm}^{-1}$, $\gamma_L = 10\,\mathrm{cm}^{-1}$, $N = 500$. Left: Dipole-induced switching rates R^e_{sw} [1/e] versus vibrational lifetime parameter τ_1^{vib} [fs]. $I = 10\,\mathrm{nA}$. Center: Arrhenius plot of dipole and temperature-induced switching rates R^t_{sw} [Hz] versus the inverse temperature $1/T$. $I = 0.7\,\mathrm{nA}$, $\tau_1^{vib} = 10\,\mathrm{ps}$. Right: Anion resonance-induced switching rates R^e_{sw} [1/e] versus the vibrational lifetime τ_1^{vib} [fs]. $I = 1\,\mathrm{nA}$, $\Delta E_{res} = 1\,\mathrm{eV}$.

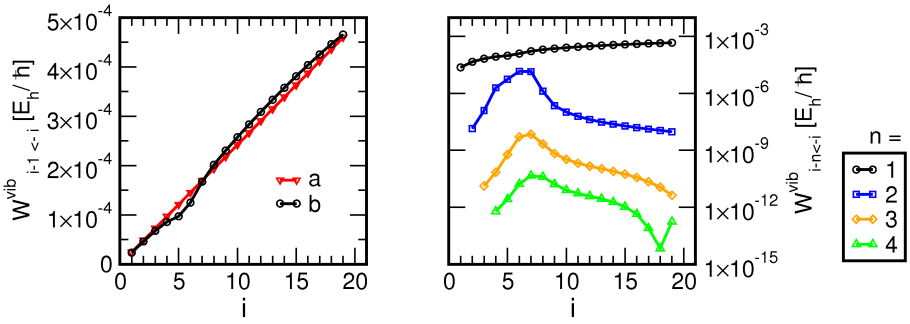

Figure 4.38: 1 D dissipative downward transition rates $W^{vib}_{i-n\leftarrow i}$ [$\mathrm{E}_h/\hbar$] between 1 D, left localized states ψ^L_i, versus doublet number i. Left: $i-1 \leftarrow i$ transition rates for (a) harmonic, bilinear- and (b) Ohmic bath dissipative model, respectively. Right: Transition rates for the Ohmic bath model and variable 'overtone-height' $n = |f - i|$.

are obviously not too important, in the 1 D representation at least. The finding proves the major assumption, made for the harmonic, bilinear model, namely the representation of dissipative processes in the double-well potential via two independent harmonic oscillators (see also Fig. 2.2 in Sec. 2.5.2.). Fig. 4.38 shows the dissipative transition rates $W^{vib}_{i-n\leftarrow i}$ for both models. The $i-1 \leftarrow i$ transition rates evolve linearly with state number i for both dissipative models. The overtone transitions are, except for a few $i-2 \leftarrow i$ transitions rates, several orders of magnitude below the $i-1 \leftarrow i$ transition rates. Therefore, the harmonic, bilinear dissipative model seems to be a reasonable approximation.

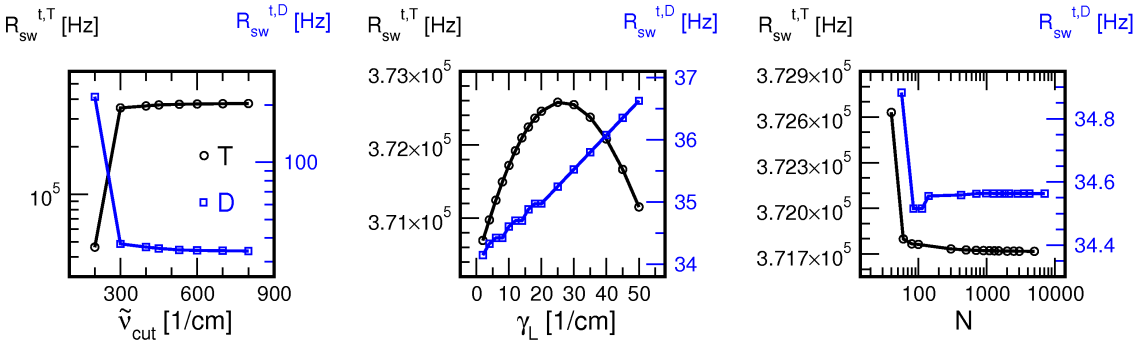

Figure 4.39: Switching rates R_{sw}^{t} [Hz] vs. Ohmic bath parameters using localized, 2 D vibrational states Left: Cutoff frequency $\tilde{\nu}_{cut}$. Center: Lorentzian width of single bath oscillators γ_L. Right: Number of bath oscillators, N. Black circles: Switching rates $R_{sw}^{t,T}$ for temperature-induced switching at $T = 100\,\mathrm{K}$. Blue squares: Switching rates $R_{sw}^{t,D}$ as obtained for the dipole mechanism and $I = 10\,\mathrm{nA}$. $\tau_1^{vib} = 1\,\mathrm{ps}$.

$\tilde{\nu}_{cut}$ [cm^{-1}]	530
γ_L [cm^{-1}]	10
N	1000

Table 4.12: Parameters, as used for the Ohmic bath dissipative model and localized, 2 D vibrational states of COD@Si(100).

(3) Parameter testing: Two-dimensional model:

The Ohmic bath dissipative model is used to calculate dissipative population transfer rates between the 2 D vibrational states of COD on Si(100). First, convergence for all Ohmic bath parameters has to be ensured. The switching rate dependencies on cutoff frequency $\tilde{\nu}_{cut}$, Lorentzian width γ_L and number of bath oscillators N are shown in Fig. 4.39. Switching rates in Hz for temperature- and dipole-IET driven vibrational excitation are plotted in black. It is seen from the left graph of Fig. 4.39 that the switching rates are nearly constant for $\tilde{\nu}_{cut} > 300\,\mathrm{cm}^{-1}$. This finding indicates, as in 1 D, that all 'important' vibrational transitions for the 2 D case are covered within the energy range of $\approx 40\,\mathrm{meV}$. Regarding the γ_L dependence, an inverted parabola is seen for the thermal switching and a somewhat larger dependence for the dipole case, as compared to 1 D. Still, the changes are small and γ_L is set to $10\,\mathrm{cm}^{-1}$, as before. Despite only minor changes in the resulting switching rates, the number of bath oscillators is increased to $N = 1000$ for all 2 D calculations. Table 4.12 summarizes the 2 D Ohmic bath parameters.

4.4.4 Dipole-induced switching

2 D localized states and the 2 D dipole surface, as shown in 4.2.4, are used in the perturbative rate equation (2.49) to obtain dipole-induced population transfer rates $W_{f\leftarrow i}^{dip}$.

Eq. (2.49) is also used to obtain the inelastic, dipole tunneling current fraction η^{dip}. The first non-negligible transition rate is found to connect the vibrational ground state and the third doublet of localized, 2 D vibrational states. For a current of $I = 1\,\mathrm{nA}$, the resulting value for $\eta_{2\leftarrow 0}^{dip}$ is 2.1×10^{-5} which is close to the value of 1.9×10^{-5} obtained for the $1 \leftarrow 0$ transition in 1 D (see Sec. 4.3.4).

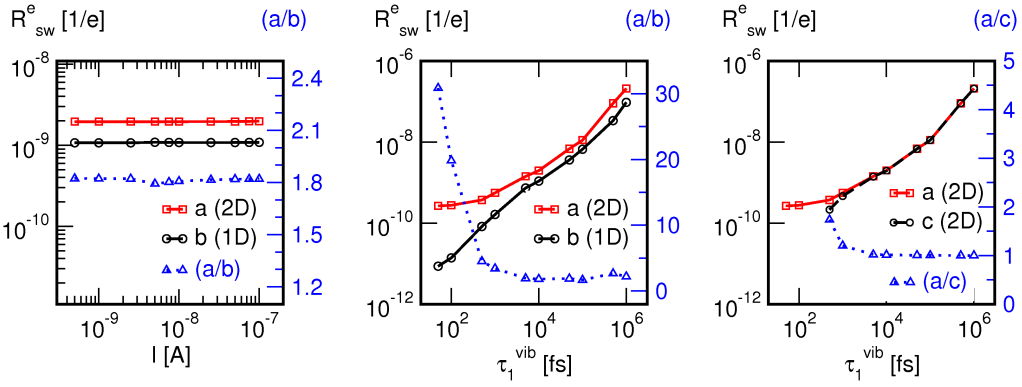

Figure 4.40: Dependence of purely dipole-induced switching rates per electron R^e_{sw}. Left/Center: STM current (I) dependence and vibrational lifetime (τ_1^{vib}) dependence: Rates calculated for 1S2D model (a) and 1S1D model (b), respectively. The ratio (a/b) is plotted in blue. Right: Vibrational lifetime (τ_1^{vib}) dependence: Rates calculated for the 1S2D model, including (a) and excluding $L \leftrightarrow R$ transition rates (c). The ratio (a/c) is plotted in blue.

In order to study the switching mechanism and to compare 1S1D and 1S2D results, Fig. 4.40 shows the dependence of dipole-induced switching rates per electron R^e_{sw}, upon the STM current and the vibrational lifetime. A constant switching yield per electron is observed for 1S2D, as well as an increase of R^e_{sw} by a factor of ≈ 1.8, relative to the 1S1D results. The single-electron switching mechanism is preserved and the increase is in the expected range, due to different dipole-surface fits for 1 D and 2 D as already discussed previously (see Sec. 4.3.4). Since all population is initially in the vibrational ground states $\tilde{\psi}_0^L$ or $\tilde{\psi}_0^R$, direct transitions to states in the ps-tunneling regime dominate the switching process, as already found for the 1S1D model. The transition rates between vibrational ground state and the first state above the barrier are somewhat larger for 2 D as compared to 1 D. This is taken as the main reason for the observed increase for the switching rates for 2 D. Besides the increase in the dipole rates, another reason for faster switching in 2 D lies in the 9 meV lowered switching barrier for the 2 D potential energy surface.

In the middle graph in Fig. 4.40, the vibrational lifetime dependencies of 1S1D and 1S2D dipole-induced switching rates are shown. The ratio between both rates is plotted in blue and reveals qualitative agreement for $\tau_1^{vib} > 5$ ps, where a constant ratio of ≈ 1.8 is seen. For smaller values of τ_1^{vib}, the purely $L \leftrightarrow R$ rate-induced switching dominates, as can be seen from the right graph of Fig. 4.40. Again the 1S2D switching rates are plotted versus the vibrational lifetime τ_1^{vib}, (a) including and (c) neglecting $L \leftrightarrow R$ transition rates. Below $\tau_1^{vib} = 0.5$ ps only $L \leftrightarrow R$ rate dominated switching is seen, since switching rates are virtually zero for curve b. Switching via the $L \leftrightarrow R$ rates seems to be more important for the 1S2D model than for 1S1D. A possible reason is the decreased localizability Q of 2 D vibrational states (see Fig. 4.33) compared to 1 D vibrational states. In 2 D, some states show Q-values of only 70 % whereas Q is always above 80 % for 1 D vibrational states. An additional contribution comes from $L \leftrightarrow R$ dissipative rates in the 2 D model.

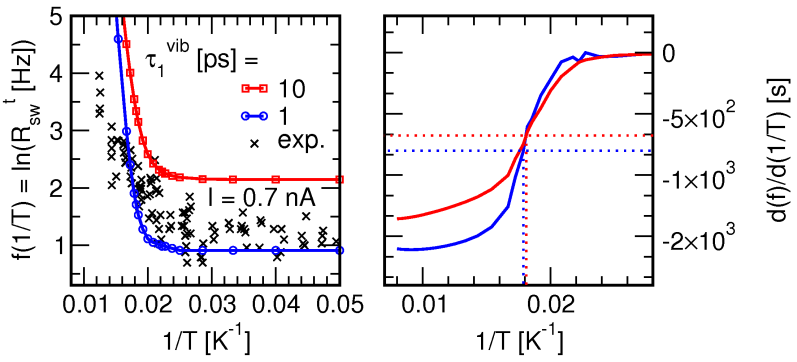

Figure 4.41: Left: Arrhenius plots of dipole- and temperature-induced switching for COD@Si(100) in the 2 D neutral electronic ground state. Comparison between calculated switching rates (solid lines) and STM-experimental data (black crosses) [151]. *Calculations:* Switching rates R_{sw}^{t} [Hz] for $\tau_1^{vib} = 1$ ps and 10 ps at a current of 0.7 nA. *Experiment:* Please refer to the caption of Fig. 4.20 for further details. Right: First derivative of switching rates R_{sw}^{t} with respect to the inverse temperature.

τ_1^{vib}[ps]	1	10
$1/T_c$ [K^{-1}]	≈ 0.018	≈ 0.018
T_c [K]	≈ 56	≈ 56
A [Hz]	2.41×10^{12}	9.62×10^{10}
E_A [meV]	134.9	111.0

Table 4.13: Crossover temperatures T_c [K], $1/T_c$ [K^{-1}] and Arrhenius rate law parameters A [Hz] and E_A [meV] for dipole-induced switching rates obtained for the 1S2D model and different vibrational lifetimes τ_1^{vib}.

4.4.5 Combined temperature- and dipole-induced switching

Next, combined dipole- and temperature-induced switching in the electronic ground state is examined and compared to 1 D results and the experiment. The left side of Fig. 4.41 shows Arrhenius plots for two different vibrational lifetimes τ_1^{vib}. The current is set to 0.7 nA in order to meet experimental conditions [151]. The crossover temperatures T_c and Arrhenius parameters obtained from Fig. 4.41 are summarized in Tab. 4.13. Unfortunately, the calculated data points show small oscillations. Therefore, only the first derivatives could be evaluated here. The comparison to the corresponding 1S1D data, listed in Tab. 4.8 on page 77, shows perfect agreement for the value of T_c. The Arrhenius prefactors A are slightly higher for 1S2D, which is due to the higher rates of purely dipole-induced switching here. The activation energy is lowered by ≈ 3 meV, as compared to the 1S1D data. The decrease is slightly smaller than expected, since the 2 D TS is 9 meV lower in energy than for the 1 D potential.

4.4.6 Resonance-induced switching: Below-threshold regime

Next, the analysis of resonance-induced switching in the *below-threshold limit* is performed for the 1S2D model, in analogy to the 1S1D procedure (see Sec. 4.3.6). The HOMO- and LUMO-based resonance state surfaces for anion and cation of COD@Si(100) are plotted in Fig. 4.7 on page 61. The 2 D switching barriers are lowered relative to 1 D by 9 meV, 25 meV and 12 meV for neutral, anion and cation surfaces, respectively, as listed

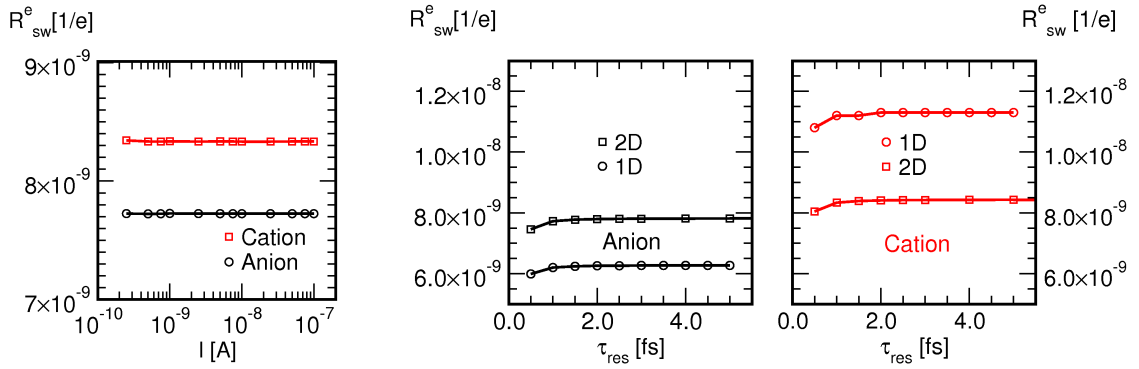

Figure 4.42: Switching rates per electron R^e_{sw} for below-threshold resonance switching via anion and cation electronic states. $|\Delta E_{res}| = 3\,\mathrm{eV}$, $\tau_1^{vib} = 1\,\mathrm{ps}$. Left: Switching rates vs. STM current $I\,[A]$. $\tau_{res} = 1\,\mathrm{fs}$. Right: Switching rates vs. resonance lifetime τ_{res}. 1S1D results (1D) are shown for comparison. $I = 1\,\mathrm{nA}$.

in Tab. 4.1.

As previously, the perturbative rate equation (2.52) is used to calculate resonance-induced transfer rates. The resulting resonance transition rates $W^{res}_{f\leftarrow i}$ are determined by the difference-potential between resonance and neutral ground state surfaces, $(V_{es}(\phi_s,\phi_u) - V_{gs}(\phi_s,\phi_u))$. Further the resonance lifetime τ_{res} and the spacing between resonance center and Fermi level ΔE_{res} enter as model parameters. Before checking the parameter dependencies of the resonance switching rates, the 1S2D inelastic resonance tunneling current fraction η_{res} is calculated via Eq. (2.55). The first, non-negligible transition rate is seen between the vibrational ground state and the third doublet of localized 2 D vibrational states. The rate $W^{res}_{2\leftarrow 0}$ is $\approx 1.3\times10^{-11}\,(\mathrm{E}_h/\hbar)$ for the anion- and $\approx 1.4\times10^{-13}\,(\mathrm{E}_h/\hbar)$ for the cation-resonance with $\tau_{res} = 1\,\mathrm{fs}$, $|\Delta E_{res}| = 1\,\mathrm{eV}$ and $I = 1\,\mathrm{nA}$. The resulting values for η_{res} are about 8.6×10^{-5} and 9.3×10^{-7} for anion- and cation-surfaces, respectively. The large difference between both, of about two orders of magnitude, was already observed for 1S1D. A comparison to values for η_{res} as calculated for the 1S1D model on page 80, shows a decrease by $\approx 20\,\%$ and $\approx 80\,\%$ for anion- and cation-induced switching and 1S2D, respectively.

The dependence upon the STM current, plotted in the left graph of Fig. 4.42, reveals the same single-electron switching mechanism as for 1S1D. The 1S2D ratio of about 1.08, between switching yield of cation and anion is smaller than the ratio of about 1.8, obtained for 1S1D. Here, it was already seen that the ratio does not depend on $|\Delta E_{res}|$, which is set to 3 eV here. Also τ_{res}, set to 1 fs here, does not affect the rate, as one can seen from two plots on the right side of Fig. 4.42. 1S2D and 1S1D results are plotted in comparison, showing that the anion yield is higher and that the cation yield is lower in 1S2D than in 1S1D (for $\tau^1_{vib} > 1\,\mathrm{ps}$). For $\tau_1^{vib} = 1\,\mathrm{ps}$, the ratios between 1S1D- and 1S2D-switching rates are 0.8 and 1.4 for anion and cation, respectively. These changes further improve the agreement to the experimentally observed equivalence of switching yields per electron at positive and negative bias voltages [10]. The ratio between cation- and anion-induced switching, given as a blue dotted line in the left plot of Fig. 4.43, is almost constant.

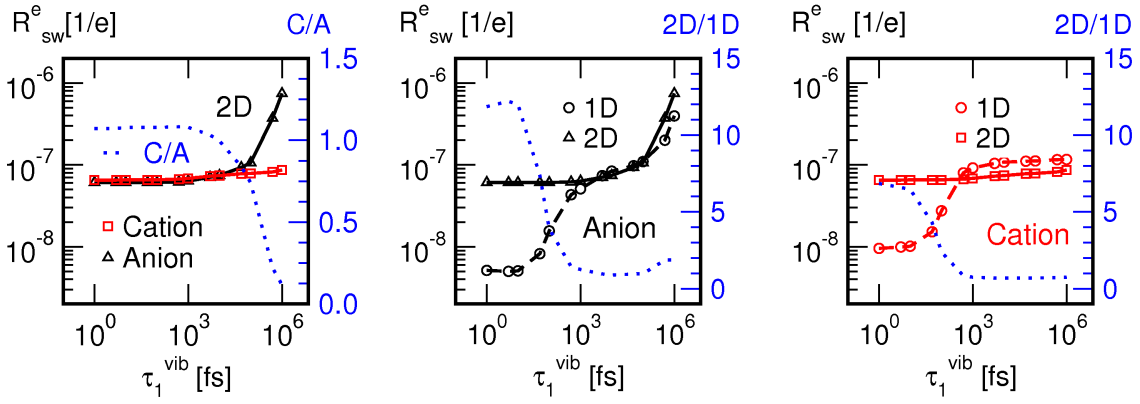

Figure 4.43: Below-threshold, resonance-induced switching rates per electron R^e_{sw} in dependence of the vibrational lifetime τ_1^{vib}. Parameters: $\tau_{res} = 1\,\text{fs}$, $I = 1\,\text{nA}$, $|\Delta E_{res}| = 1\,\text{eV}$. Left: Cation and anion resonance-induced switching in 2 D. Middle/Right: Anion and cation resonance-induced switching in 1 D and 2 D. The ratio between 2 D- and 1 D-switching rates is plotted in blue.

A new finding for the 1S2D model is the constant rate of resonance-induced switching for $\tau_1^{vib} < 1\,\text{ps}$, as compared to the 1S1D results. A comparison of resonance-induced switching rates versus the parameter $\tau_1^{vib} = 1\,\text{ps}$ is shown in the center and on the right hand of Fig. 4.43.

Further it is seen, that the anion switches more rapidly compared to the cation in conjunction with an increasing vibrational lifetime. The same picture was already seen for the 1S1D model and is also here caused by the fact that doublets with a long tunneling time T_n states (states of lower energy) are less efficiently populated via the cation surface compared to the anionic one. Therefore switching via the anion resonance is more sensitive to the the parameter τ_1^{vib}. A detailed explanation, taking transition rates and tunneling times into account, was already given in Sec. 4.3.6.

In the following the qualitative difference between 1S1D and 1S2D models, found for the 'below 1 ps regime' is discussed. For this purpose, the 1S2D switching rates are calculated and plotted in dependence upon the vibrational lifetime in Fig. 4.44. The calculations include (a) and exclude (b) $L \leftrightarrow R$ transition rates between both potential wells. It turns out that the $L \leftrightarrow R$-rate driven switching becomes much more important for 1S2D, as compared to 1S1D, since it entirely dominates the switching below $\tau_1^{vib} = 1\,\text{ps}$. For 1S1D, the $L \leftrightarrow R$-dominating regime was found for vibrational lifetimes below 0.1 ps. As already discussed for the 1S2D dipole results, the increased importance of $L \leftrightarrow R$ transition rates is assumed to originate from the lower degree of localization for the 2 D states and from the inclusion of $L \leftrightarrow R$ transitions via the Ohmic bath dissipative model. Nevertheless, within the reasonable vibrational lifetime range above 1 ps the switching rates changes by a factor of two at most. This is an acceptable range for an order of magnitude estimate of resonance-induced switching in the below-threshold regime.

Fig. 4.45 depicts the dependence of resonance-induced switching rates upon the parameter ΔE_{res} . The qualitative picture, shown here, resembles the behavior as already seen for

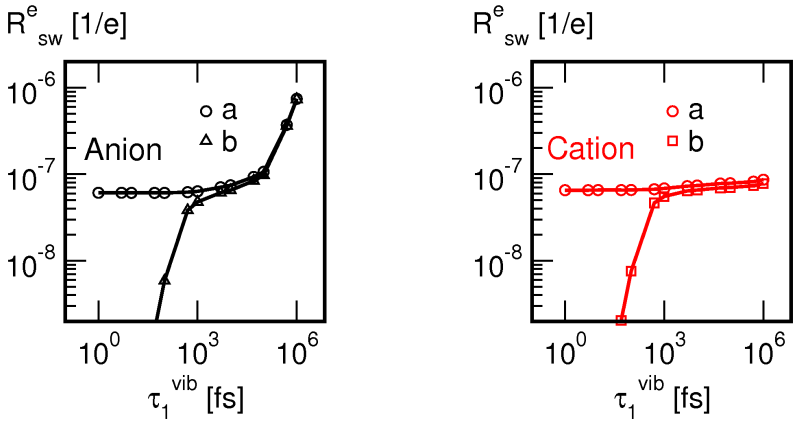

Figure 4.44: Switching rates per electron R^e_{sw}, for anion resonance- (left) and cation resonance-induced switching (right), depending on the vibrational lifetime parameter τ_1^{vib}. (b) All transition rates are included, (a) all $L \leftrightarrow R$-transition rates are set to zero. $\tau_{res} = 1\,\text{fs}$, $I = 1\,\text{nA}$, $|\Delta E_{res}| = 1\,\text{eV}$.

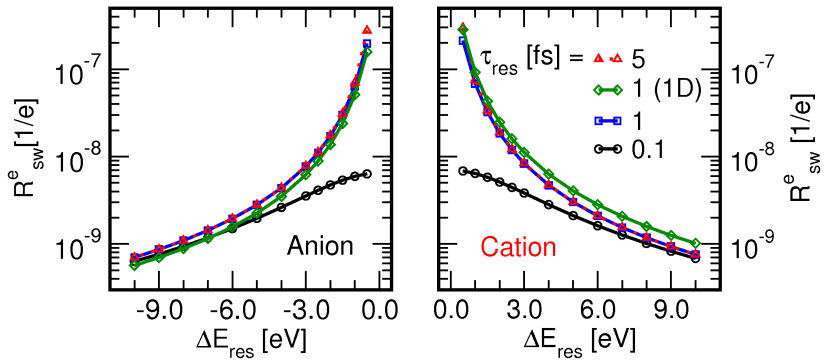

Figure 4.45: Anion- and cation-resonance-induced switching rates per electron R^e_{sw} [1/e], depending upon the energetic spacing between resonance and the Fermi level of the tip ΔE_{res} for three different resonance lifetimes τ_{res}. 1S1D results are shown for comparison as green, solid lines. $\tau_1^{vib} = 1\,\text{ps}$.

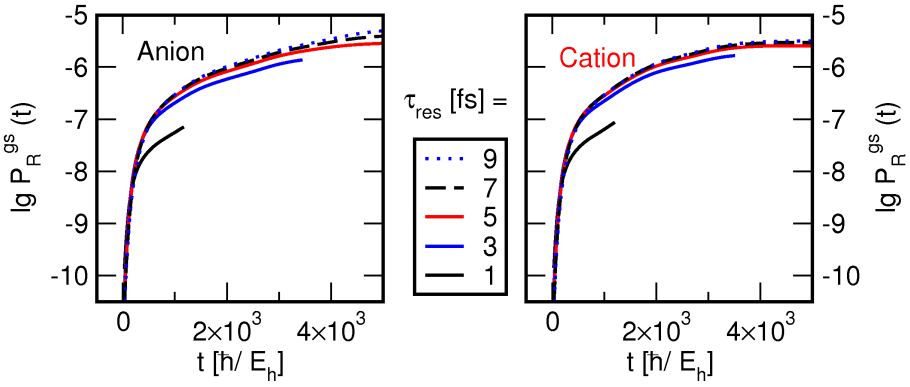

Figure 4.46: 2S2D ground state population $P_R^{gs}(t)$ in the first 100 fs of the propagation for various resonance lifetimes τ_{res}. All population was initially located in $\tilde{\psi}_0^{L,g}$ of the electronic ground state and upward projected to the resonance surface before the start of each propagation. $\tau_1^{vib} = 1\,\text{ps}$.

the 1S1D model. The 1S1D results for $\tau_{res} = 1\,\text{fs}$ are shown in green for comparison. A slight increase and decrease for anion and cation, respectively, are seen again. If one considers the voltage independence observed in the experiment, the previously discussed possibilities for the below-threshold regime are conceivable within certain limits for both 1S1D and 1S2D models.

4.4.7 Resonance-induced switching: Above-threshold regime

Finally, the 2S2D, above-threshold calculations for resonance switching are compared to the 1S2D results. Technical details of those two-surface propagations were already discussed in Sec. 4.4.2. As stated there, each propagation is split into two parts. In the first part, including two surfaces, the upward projected, localized ground state population quickly decays back to the ground state. In the second part, only the neutral surface is propagated further. The switching yield is determined after all population relaxed to non-switching, i.e., non-tunneling vibrational states in the electronic ground state. Convergence in the switching yield per electron is observed, including 750 vibrational wave functions for the electronic ground state and also for the resonant surface, respectively.

Only two parameters enter the 2S2D simulation of resonance-induced switching, namely the vibrational lifetime in the electronic ground state τ_1^{vib} and the resonance lifetime τ_{res}. The following part focuses on the mechanistic discussion of resonance switching in the 2S2D model. Therefore, a set of propagations will be looked at starting with an upward projection of state $\tilde{\psi}_0^{L,g}$ carrying all electronic ground state population, initially.

Fig. 4.46 depicts the switched population in the right potential well of the electronic ground state and the resonance state for both anion and cation resonances, respectively.

The localization error, coming with the upward projection of the entirely left-well localized ground state population of $\tilde{\psi}_0^L$, is below $\approx 1 \times 10^{-10}$. The error is far below the final switching yield and therefore taken as insignificant. So far, the switching mechanism for the 2S1D approach was stated to be dominated by tunneling in the electronic ground state.

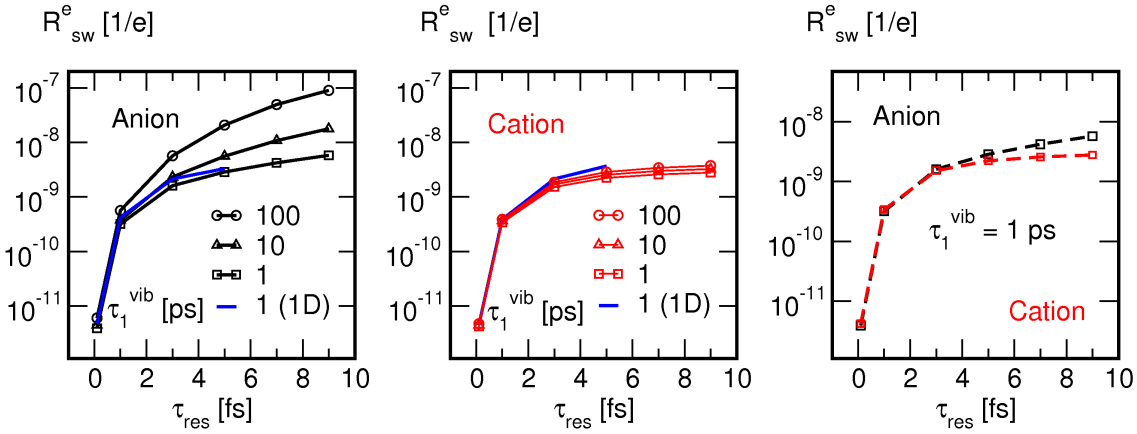

Figure 4.47: Switching rates per electron R^e_{sw} [1/e] for the 2S2D model of above-threshold, resonance switching. Rates are plotted in dependence upon the resonance lifetime τ_{res} for various vibrational lifetimes τ_1^{vib}.

The same picture is seen for the 2S2D model, despite explicitly including the possibility for switching in the resonant state. For all tested resonance lifetimes $\tau_{res} = 1 \ldots 9\,\text{fs}$, the amount of population, switching already in the resonance state, stays below $1 \times 10^{-8}\,1/\text{e}$. Resonant state lifetimes above 9 fs are considered unlikely for the system and were therefore not tested.

Instead, Fig. 4.46 shows that the switching takes place in the neutral ground state. It is seen that within the first few fs of each propagation, the major part of the switching population is already trapped in the right well of the ground state potential. Oscillations due to back- and forth tunneling of the excited wave packet are not observed, since they are damped by vibrational dissipation ($\tau_1^{vib} = 1\,\text{ps}$).

Fig. 4.47 shows the dependence of the switching rate upon the resonance lifetime for different vibrational lifetimes. The qualitative shape of the plots was already seen for 2S1D and therefore 2S1D rates are added as blue lines for comparison. All rates in the first and second graph are scaled by 1×10^{-3}, accounting for the ratio I_r/I or excitation probability (see Sec. 4.3.7). Under this assumption, the switching rates for anion and cation are reasonably close to the experimental value of $\approx 1 \times 10^{-9}$ [1/e] [10]. Generally, each curve has two regimes. A zone of 'strong' τ_{res} dependence up to 2.5 fs and a zone of weaker dependence above. While for the first one, switching via anion and cation resonance is similarly rapid, the switching rates diverge for anion and cation in the latter zone, as can be seen in the right graph of Fig. 4.46. Here it is found, that the switching yield for the cation stays nearly constant above $\tau_{res} = 2.5\,\text{fs}$, while the yield for the anion further increases. The difference becomes larger with increasing values of τ_{res} and τ_1^{vib}. Within the 2S2D model, combinations of 'large' values for both, e.g. $\tau_{res} > 5\,\text{fs}$ and $\tau_1^{vib} > 10\,\text{ps}$ therefore, do not fit to the experimentally observed insensitivity of the switching yield on the sign of the bias voltage. The dependence of the anion resonant switching rates upon τ_{res} decreases with an increasing dissipative strength for the neutral ground state.

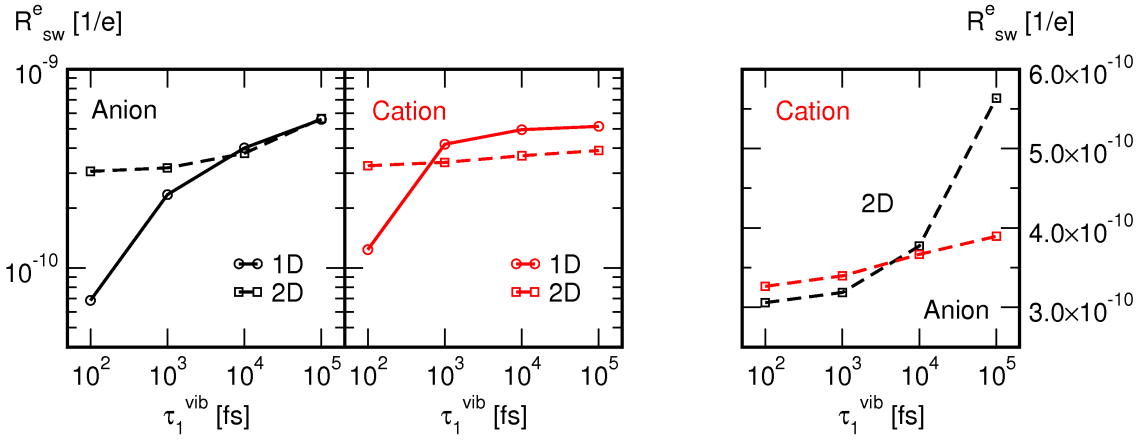

Figure 4.48: Switching rates per electron R^e_{sw} [1/e] for the 2S1D and 2S2D models of above threshold, resonance switching. Rates are plotted in dependence upon the vibrational lifetime τ_1^{vib}. $\tau_{res} = 1$ fs. Left: Comparison of 1 D and 2 D switching rates per electron, with respect to the vibrational lifetime τ_1^{vib}. Right: Comparison of anion- and cation-resonance-induced switching rates obtained in 2 D. Rates are not scaled.

Obviously, a longer lifetime on the excited anion surface allows for higher vibrational excitation in the ground state, which is not seen for the cation resonance.

Fig. 4.48 shows the vibrational lifetime dependence of the 2S2D resonance switching. Here the focus is on the comparability of 2S1D and 2S2D results. As already seen from the one surface calculations in Fig. 4.43, qualitative agreement is achieved only above $\tau_1^{vib} \approx 1$ ps. Within the 1S2D model $L \leftrightarrow R$ rate-induced switching was dominating for smaller vibrational lifetimes (see Fig. 4.44). In the 2S2D model no IET rates are present. Now, the same constant switching yield per electron is seen below $\tau_1^{vib} < 1$ ps, as already observed for the 1S2D. The latter finding shows that switching is dominated by $L \leftrightarrow R$ transition rates, below $\tau_1^{vib} < 1$ ps, originating from the Ohmic bath dissipative model applied on non-perfectly localized vibrational states. The latter can be taken as an artifact which is not further considered in the discussion since the $L \leftrightarrow R$ transition rates are not dominating the switching process for physically realistic vibrational lifetimes $\tau_1^{vib} \geq 1$ ps.

In the right graph it is further seen that the anion switching yield per tunneling electron exceeds the cation yield for $\tau_1^{vib} > 1$ ps, which is also in agreement to the already discussed 2S1D and 1S2D models.

4.4.8 Summary

The last section included the extension to a two dimensional representation of the bi-conformational switching of COD@Si(100). Preliminarily, the one-dimensional switching Hamiltonian used earlier only allowed for a symmetric rotation of both COD-$(CH)_2$ groups. The second dimension includes the possibility of an independent rotation of both groups. As a consequence, the switching barrier is slightly lowered, following the 'real' transition

state of the potential. Using the same toolbox as before, the 2 D switching dynamics was tested using one- and two-surface calculations. But, in 2 D the dissipative rates were calculated via the 'Ohmic bath' model, allowing for the calculation of dissipative rates between all states, instead of a simple linear scaling law and harmonic selection rules. Nevertheless, the former 1S1D and 2S1D results, using the bilinear, harmonic dissipative model were confirmed for the 1 D models via the Ohmic approach. Further, most other findings, obtained in 1 D, were confirmed by the 2 D models. Those findings included the single-electron mechanism, equivalent switching rates via anion and cation resonance states, and the crossover temperature between IET- and temperature-driven switching regimes. As the only major difference, an increased contribution of switching via direct $L \leftrightarrow R$ transition rates was seen for vibrational lifetimes below 1 ps, coming mainly with the Ohmic bath dissipative model being applied on non-perfectly localizable states.

Chapter 5

Conclusion

The aim of this thesis is the quantum dynamical study of two examples of scanning tunneling microscope (STM)-controllable, Si(100)(2×1) surface-mounted switches of atomic and molecular scale.

The STM and the atomic force microscope (AFM) are powerful experimental techniques that, in a revolutionary way, have opened the possibility for the examination and manipulation of preliminary hidden landscapes, composed out of three-dimensional molecular and atomic surface structures [7, 8].

The Si(100)(2×1) surface and semiconductor surfaces in general are an experimentally challenging, but very flexible and interesting object for examinations via the STM. They offer well defined chemisorption sites and a moderate coupling to the adsorbate, preserving the flexibility for intermolecular structure rearrangements of a switching molecule, for example. Additionally, silicon is a standard substrate of the current electronic industry and as such an interesting basis for future surface-mounted switches. Beside that, the understanding of fundamental processes, like vibrational and electronic excitation and de-excitation of surface-adsorbates, was the main motivation for this theoretical study. For the provision with recent experimental results and the ability to simulate and interpret them theoretically, the collaborative research centre Sfb 658 "Elementary processes in molecular switches at surfaces" is greatly acknowledged in whose framework this thesis was created.

The actual work focuses on STM-induced changes in chemisorbed adsorbates on the Si(100)(2×1) surface, studied by the means of quantum dynamical simulations. Therefore, a general model for binary switching on a 1 D and 2 D double well potential energy surface (PES) is established, as introduced in the following. The double well structure represents the two stable switching states on the potential energy landscape of the surface-adsorbate. Initially, for each dynamical simulation the adsorbate is set to an electronically and vibrationally relaxed state, i.e., a state of low energy. As a consequence the switch is 'trapped' or localized in one of the two switching positions or PES minima. Therefore, the adsorbate was characterized by a group of localized vibrational states, which separately describe the so called 'left' and 'right' potential well of the PES. The distribution

of the adsorbate population among the localized vibrational states represents its amount of vibrational energy.

Within the STM experiment energy is transfered between the electrons, tunneling between the STM-tip and the surface, and the adsorbate in a process of inelastic electron tunneling (IET). The adsorbate might become vibrationally excited and eventually passes the barrier between both wells of the PES and might switch to the opposite switching state. Also the transfer of vibrational energy between the surface and the adsorbate has to be considered. A thermally 'cool' surface for example will absorb vibrational energy in a dissipative relaxation process from a vibrationally excited adsorbate.

In order to be able to describe this processes an entity called 'density matrix' is used, which contains all information about the system, e.g., the population of individual vibrational and localized states or mixtures of those states. The temporal dynamics are provided by the propagation of the density matrix in time via an according set of equations of motion (EQM). The latter are based on the open-system density matrix theory in Lindblad form. Via this formalism it is possible to separate system and bath in order to restrict the complexity of the overall problem, i.e., the number of vibrational and electronic states, to a feasible number. Both, the tunneling electrons and the surface are subsumed in a so called 'bath' entity, while the switching adsorbate is treated as the 'system'. While the system is treated in detail, the influence of the bath is subsumed in transition rates between individual system states.

First order perturbation theory is used to evaluate those transition rates between vibrational levels of the system part. In order to account for interactions with the surface phonons, two different dissipative models are used, namely the bilinear, harmonic and the Ohmic bath model. The first one considers the system states as harmonic which results in a linear scaling law between state number or energy and dissipative transition rate. The Ohmic bath model considers anharmonicities of the state functions and some information about the bath, e.g. the bath phonon density of states. Additionally, the influence of the silicon surface could be systematically tested via both models, using partly unknown parameters in both dissipative models, covering the coupling strength between adsorbate and surface as well as the surface temperature.

IET-induced vibrational transitions in the system are due to the dipole- and the resonance-mechanism. The tunneling electron charge can inelastically couple to the permanent dipole moment of the adsorbate. For the resonance mechanism a temporal population (anion resonance) or depopulation (cation resonance) of adsorbate electronic levels causes vibrational transitions. If the bias voltage of the STM and therefore the energy of tunneling electrons (or holes) is below the resonance energy, resonant excitation can still take place in the below-threshold regime. Those events are rare and their influence can be described by first order perturbation theory again. For the above-threshold regime the probability for a temporal population of an ionic resonant state is much higher, and a second electronic state surface has to be incorporated into the density matrix propagation.

Therefore, only a single surface approach is used to study the influence of dipole scat-

tering and resonance scattering in the below-threshold regime. For this, the harmonic approximations of Persson et al. [25, 24] and Walkup et al. [70] are utilized and extended towards a non-harmonic treatment of dipole function, resonance state potential and vibrational states. The extension permits the inclusion of overtone-contributions arising from anharmonicities, which turned out to play an important role for the switching process and were not considered before. Further, a second electronic surface was included to study the resonance-induced switching in the above-threshold regime.

Static properties of the adsorbate, e.g., potentials and dipole function and potentials, are obtained from quantum chemistry and used within the established quantum dynamical models as described above. The first example considers the switching of single H-atoms between two dangling-bond chemisorption sites on a Si-dimer of the Si(100) surface [9]. The second system examines the conformational switching of single 1,5-cyclooctadiene molecules chemisorbed on the Si(100) surface [10].

For H@Si(100) a hole-resonance based, single-electron mechanism was found experimentally for the above-threshold, low-current regime. For the below-threshold, high-current regime, considered here, a multi-electron switching mechanism based on vibrational ladder-climbing and subsequent tunneling was established for a 1 D switching model, i.e., H-Si stretching and bending mode are subsumed to a single lateral switching coordinate. Unfortunately, there are no experimental data available for the high-current regime in the moment, while the above-threshold, low-current regime was already a subject of a comprehensive theoretical study by Abe et al. [79]. Further, a model potential for the cation resonance state is derived via Koopmans' theorem. The theorem allows the calculation of ionic state energies based on ab initio calculations for a neutral cluster model of H@Si(100). Also, the influence of surface temperature and the field strength provided by the STM-tip is tested and is found to be in good accordance with experimental and other theoretical data. It is found that the correct quantum chemical description of the switching barrier in the neutral state is difficult using standard density functional theory. The barrier is located at the site of a conical intersection, showing multi-reference character. Also an enhanced description of the resonance state surface as well as simultaneous treatment of H-Si stretching- and bending model would be an interesting project for the future.

In the second part of the thesis, the bi-conformational, STM-induced switching of COD@Si(100) is studied, using and extending the theoretical model utilized for H@Si(100). No distinct resonance was seen by experiment and equal switching rates were observed at positive and negative bias voltages. Despite this findings, model PES for anionic and cationic resonant states are derived via Koopmans' theorem in order to simulate resonant excitation processes.

The results for the study of dipole- and resonance-induced switching permit the reproduction of major experimental finding like the single-electron switching mechanism, the equality of switching rates for anion- and cation-resonances and the absence of voltage dependence in the switching rates. Further, resonance-induced switching was studied in the below- and above-threshold regime (see above). For the below-threshold regime, the

experimentally observed voltage independence can be explained by two different physical scenarios. The first would be a very broad and flat resonance, .i.e., the probability for a resonant excitation is equally low for a wide range of tunneling electron or hole energies. For the second, the resonance center stays far above the energy range of tunneling holes or electrons within the experimentally feasible range. For the above-threshold resonance excitation a different physical picture is suggested for the explanation of the voltage-independence. Here, electrons or holes are injected into the conducting- or valence bands of the semiconductor surface. Since the band consist of a continuum of states which are coupled amongst each other, the electron or hole quickly relaxes via non-adiabatic coupling events into the LUMO- or HOMO-orbital of the surface-adsorbate entity. The electronic lifetime of an electron injected into the LUMO or a hole injected in the HOMO is much longer as compared to electronic states in the band, inducing nuclear dynamics in the system. However, the question regarding the likelihood of the depicted below- and above-threshold switching models can not be satisfactorily answered within the current thesis and remains a very interesting question for the future.

Also for the dipole mechanism, a linear dependence of the switching rates upon the tunneling current was seen within our actual model. Both resonance- and dipole-mediated switching in the below-threshold regime were found to be based on overtone-transitions towards rapidly tunneling vibrational states. The latter finding was based on the perturbative model as developed for H@Si(100), mentioned previously. Also here, a final decision about the dominating mechanism, i.e., dipole or resonance, is not possible until now, since in principle both mechanisms would be compatible to experimental findings. An estimate of the vibrational lifetime of COD or the current fraction, passing a resonance, would help to finally decide about the quality of the models used.

For the study of temperature dependence of the switching process the actual model predicts a crossover temperature between IET- and thermal switching regimes of $\approx 50\,K$, which was confirmed by subsequent STM measurements at variable temperatures, carried out by a cooperating experimental group [151]. The 2 D models, using an alternative Ohmic bath formalism to calculate vibrational relaxation rates, confirmed the results obtained in 1 D.

For an future application, e.g., in a storage device, the conformational switching barrier for COD@Si(100) has to be increased in order to allow for an increased stability of the switching states at elevated temperatures. Also the insertion of photo-sensitive substituents might allow for a photo-induced switching process as well as for an optical test of the switching states. Also here, a theoretical study should precede and accompany those future experiments.

Appendix A

Symmetry-adapted basis set

This section deals with the calculation of vibrational eigenfunctions (ψ_n) for a symmetric potential ($V\{q_i\}$) using a spatial grid basis and the FGH (Fourier Grid Hamiltonian) method [92] (see also Sec. 2.2). All eigenfunctions reflect the symmetry of the corresponding potential. Unfortunately, due to numerically limitations, the diagonalization of the Hamilton matrix reveals unsymmetrical eigenfunctions for symmetric potentials, in the case of small tunnel splittings. One can avoid the problem by using symmetry-adapted basis functions, as will be explained for the case of a one-dimensional potential $V(q)$, of C_s symmetry, i.e., $V(q) = V(-q)$. The delta functions $\varphi_i^{\pm} = \delta(q \pm (i + 1/2)\Delta q)$, are used to represent ψ_n in the basis of a spatial grid,

$$\psi_n(q) = \sum_{i=1}^{N/2} c_{i,n}^{+}\varphi_i^{+} + c_{i,n}^{-}\varphi_i^{-} \qquad . \tag{A.1}$$

Here, N is the number of grid points. The $\varphi_i^{\pm}$ are transformed into the symmetry-adapted basis functions, $\varphi_i^{'}$ and $\varphi_i^{''}$,

$$\varphi_i^{'} = \frac{1}{\sqrt{2}}(\varphi_i^{+} + \varphi_i^{-}) \qquad ; \qquad \varphi_i^{''} = \frac{1}{\sqrt{2}}(\varphi_i^{+} - \varphi_i^{-}) \qquad . \tag{A.2}$$

The functions $\varphi_i^{'}$ and $\varphi_i^{''}$ constitute a basis for the symmetric ($A^{'}$) and antisymmetric ($A^{''}$) irreducible representations of the C_s point group. Under influence of the mirror operator ($\hat{\sigma}$) they transform like,

$$\hat{\sigma}\varphi_i^{'} = \varphi_i^{'} \qquad ; \qquad \hat{\sigma}\varphi_i^{''} = -\varphi_i^{''} \qquad . \tag{A.3}$$

$\underline{\underline{H}}$ is block-diagonal in the basis $\{\varphi_k^{'}, \varphi_k^{''}\}$, with blocks $\underline{\underline{H}}^{'}$ and $\underline{\underline{H}}^{''}$,

$$H_{i,j}^{'} = \langle\varphi_i^{'}|\hat{H}|\varphi_j^{'}\rangle = \frac{1}{2}\left(H_{i,j} + H_{-i,-j} + H_{-i,j} + H_{i,-j}\right) = (H_{i,j} + H_{-i,j}) \qquad . \tag{A.4}$$

For symmetry reasons $H_{ij} = H_{-i,-j}$.

$$H_{ij}^{''} = \langle\varphi_i^{''}|\hat{H}|\varphi_j^{''}\rangle = (H_{i,j} - H_{-i,j}) \qquad . \tag{A.5}$$

After solving the eigenvalue problem for both sub-matrices,

$$\underline{\underline{H}}^{'}\underline{C}_n^{'} = E_n^{'}\underline{C}_n^{'} \qquad ; \qquad \underline{\underline{H}}^{''}\underline{C}_n^{''} = E_n^{''}\underline{C}_n^{''} \tag{A.6}$$

via diagonalization, the resulting eigenfunctions ($\psi_n^{'}$ and $\psi_n^{''}$) are expressed in the non symmetry-adapted grid basis, using Eq. (A.1) and (A.2).

$$\psi_n^+(q) = \sum_{i=1}^{N/2} \frac{c_{in}^{'}}{\sqrt{2}}(\varphi_i^+ + \varphi_i^-) \qquad \psi_n^-(q) = \sum_{i=1}^{N/2} \frac{c_{in}^{''}}{\sqrt{2}}(\varphi_i^+ - \varphi_i^-) \qquad . \tag{A.7}$$

The resulting functions of even and odd parity, $\psi_n^+(q)$ and $\psi_n^-(q)$, are now symmetric and antisymmetric with respect to the potential center, reflecting both irreducible representations of the C_s point group. Also for higher dimensionalities an analog procedure can be performed. In the case of potential, belonging to the C_{2v} point group, four different Hamilton matrices are set up to evaluate symmetry-adapted eigenfunctions, according to the four irreducible representations, A_1, A_2, B_1 and B_2.

Appendix B

4th order Runge-Kutta integrator

The Runge-Kutta integrator of 4th order [153] represents a four step algorithm for the approximate numerical solution of ordinary differential equations. Here, the integrator is used to solve the Liouville-von Neumann equation, i.e., the time evolution of the reduced density matrix. The discretization error is reduced to 5th order, using a clever combination of different difference quotients, where $h = t_{n+1} - t_n = \Delta t$ is the distance between two discrete points on the time axis with corresponding function values y_n and y_{n+1}. To calculate the time derivative,

$$f(t_n, y_n) = \frac{dy}{dt}\Big|_{y_n, t_n} \quad , \tag{B.1}$$

the following algorithm steps are passed,

$$\begin{aligned}
1.) \quad & k_1 = hf(t_n, y_n) \\
2.) \quad & k_2 = hf(t_n + \frac{h}{2}, y_n + \frac{k_1}{2}) \\
3.) \quad & k_3 = hf(t_n + \frac{h}{2}, y_n + \frac{k_2}{2}) \\
4.) \quad & k_4 = hf(t_n + h, y_n + k_3) \\
5.) \quad & y_{n+1} = y_n + \frac{k_1}{6} + \frac{k_2}{3} + \frac{k_3}{3} + \frac{k_4}{6} \quad .
\end{aligned} \tag{B.2}$$

Appendix C

Normal mode analysis of COD@Si potential surfaces

In the following a normal mode analysis is presented for the two-dimensional (ϕ_s, ϕ_u) potential surfaces for COD@Si. For details of the underlying Hamiltonian and surface calculations refer to Sec. 4.2. In order to obtain eigenvectors $\vec{c}_{1,2}$ and normal mode frequencies $\omega_{1,2} = \sqrt{\Lambda_{1,2}}$ at stationary potential points, the Hessian matrix $\underline{\underline{H}}$. has to be diagonalized. The Hessian matrix as shown here,

$$\underline{\underline{H}} = \begin{pmatrix} \frac{k_{ss}}{I_{ss}} & \frac{k_{su}}{\sqrt{I_s}\sqrt{I_u}} \\ \frac{k_{us}}{\sqrt{I_s}\sqrt{I_u}} & \frac{k_{uu}}{I_{uu}} \end{pmatrix} \quad , \tag{C.1}$$

includes mixed derivatives, k_{su}, of second order for the potential energy with respect to the collective coordinates ϕ_s and ϕ_u. They are calculated as,

$$k_{su} = \frac{\partial^2 V}{\partial \phi_s \partial \phi_u} \quad . \tag{C.2}$$

The results obtained for TS, Ma and Mi points of the transformed are shown as black numbers in Tab. C.1. The quantum chemically obtained frequencies, calculated via B3LYP/6-31G(d) along dihedral angles ϕ_l and ϕ_r on the neutral surface by Dokić [143], are shown in red (Sec. 4.2). The B3LYP/6-31G(d) calculated frequencies for the global minimum are not shown, since the high number of quantum chemically obtained low frequency modes around 200 to 300 cm^{-1} does not allow for a clear assignment. It is seen that the transformed potential reproduces the expected imaginary frequencies at TS- and Ma-positions. The deviation of $\approx 100\,\mathrm{cm}^{-1}$ or $\approx 12\,\mathrm{meV}$, as compared to the calculated frequencies, is within the expected range, as explained in the following. While the quantum chemically calculated frequencies are based on the "exact" potential energies (see Dokić et al. [143]), the normal mode analysis, as shown above, is based on a transformed and interpolated (cubic splines) potential surface (Sec. 4.2). The second order derivatives of the Hessian matrix are very sensitive to the resulting differences between both surfaces, resulting in the observed differences.

	Mi		TS		Ma	
N	242	288	$i199$ [$i108$]	160	$i261$ [$i152$]	$i127$ [$i86$]
A	285	314	-201	170	$i246$	$i124$
C	239	272	-185	154	$i244$	$i94$

Table C.1: Normal mode analysis at minimum (Mi), transition state (TS) and maximum (Ma) positions on the 2 D potential surfaces, of COD on Si(100), shown in Fig. 4.6 and 4.7 (see Sec. 4.2). Black: Wave numbers $\tilde{\nu}$ in cm^{-1} of normal mode frequencies at neutral (N), anion (A) and cation (C) potential surfaces. Numbers on the left hand of each column refer to mode vectors along ϕ_s, numbers on the right side refer to modes along ϕ_u. Red/ square brackets: Imaginary frequencies obtained by calculations for the COD@$Si_{15}H_{16}$ cluster, performed at the B3LYP/6-31G(d) level of theory by Dokić et al. [143] (Further details are given in Sec. 4.2.1.)

Furthermore, the normal mode vectors are found to be perfectly parallel to the collective coordinate system axes, confirming their separability ($k_{su} \approx 0$), as assumed for the utilized Hamiltonian in Eq. (4.8). Furthermore, a comparison of frequencies along ϕ_s and ϕ_u shows that all three potentials are steeper along ϕ_s than along ϕ_u. It is further seen in Tab. 4.1, that the anionic resonance potential differs more from the neutral surface than does the cationic one.

Appendix D

Dipole function of COD@Si(100)

The dipole component $\mu_z(\phi_s, \phi_u)$, perpendicular to the silicon(100) surface, was evaluated as described in Sec. 4.2.4 on page 62. The resulting two-dimensional surface, depending on two rotational angles ϕ_s and ϕ_g (see Sec. 4.2.2), was fitted using the following functional form,

$$\begin{aligned}\mu_z(\phi_s,\phi_u) = {} & A_0 + A_1 \cdot e^{-(\phi_s/A_2)^2} \cdot e^{-(\phi_u/A_3)^2} \\ & + A_4 \cdot e^{-(\phi_s/A_5)^2} \cdot e^{-(\phi_u/A_6)^2} \\ & + A_7 \cdot \left[e^{-((A_8\phi_u - A_9\phi_s)/A_{10})^2} + e^{-((A_8\phi_u + A_9\phi_s)/A_{10})^2} \right] \\ & + A_{11} \cdot \tanh(A_{12}\phi_u - A_{13}\phi_s) \cdot \tanh(A_{12}\phi_u + A_{13}\phi_s) \\ & + A_{14} \cdot e^{-(\phi_u/A_{15})^2} \cdot \cos(A_{16}\phi_u) \cdot f(\phi_s,\phi_u) \qquad \text{and}\end{aligned} \tag{D.1}$$

$$f(\phi_s,\phi_u) = \sin(A_{17}(\phi_s - A_{18})) \cdot e^{-((\phi_s - A_{19})/A_{20})^2} - \sin(A_{17}(\phi_s + A_{18})) \cdot e^{-((\phi_s + A_{19})/A_{20})^2} \quad . \tag{D.2}$$

The fit parameters obtained are listed in Tab. D.1. The squared sum over residuals between fitted and original data points was below $0.0007\,\mathrm{ea_0}$ compared to the overall amplitude for the dipole function of about $0.058\,\mathrm{ea_0}$.

Parameter	Value	unit	Parameter	Value	unit
A_0	1.41395	ea_0	A_{11}	0.0137324	ea_0
A_1	-0.417009	ea_0	A_{12}	1.09754	rad^{-1}
A_2	0.267643	rad	A_{13}	2.20431	rad^{-1}
A_3	0.426138	rad	A_{14}	3.62481	ea_0
A_4	0.436053	ea_0	A_{15}	0.47060	rad
A_5	0.255634	rad	A_{16}	1.88681	rad^{-1}
A_6	0.427714	rad	A_{17}	2.26405	rad^{-1}
A_7	0.0151565	ea_0	A_{18}	0.896692	rad
A_8	0.0180749		A_{19}	1.64901	rad
A_9	0.0376762		A_{20}	0.374054	rad
A_{10}	0.0130293	rad			

Table D.1: Fit parameter for the two-dimensional dipole function ($\mu_z(\phi_s, \phi_u)$) of COD on Si(100). The fit function is written in equations (D.1) and (D.1).

Appendix E

1 D resonant vibrational eigenstates of COD@Si(100)

Here, data about vibrational eigenstates obtained for 1 D and 2 D excited state surfaces of COD are shown. First the data about anion and cation 1 D eigenstates are given in tables E.1 and E.2, respectively. Here eigenenergies E_n^+ for doublet wavefunctions n of even parity (+), tunnel splittings ΔE_n and tunneling times t_n are listed.

Doublet (n)	E_n^+ (meV)	ΔE_n (meV)	t_n (ps)
0	0	1.3×10^{-9}	1.6×10^{9}
1	38	2.7×10^{-7}	7.6×10^{6}
2	76	2.6×10^{-5}	7.9×10^{4}
3	112	1.4×10^{-3}	1.5×10^{3}
4	146	4.5×10^{-2}	47
5	176	0.88	2.3
6	200	7.1	0.295
7	223	15	0.14
8	255	18	0.12
9	292	20	0.11
10	333	21	9.7×10^{-2}
⋮	⋮	⋮	⋮
19	796	29	7.1×10^{-2}

Table E.1: Eigenstate data obtained for the 1 D, anionic resonant state potential of COD on Si(100). Given are eigenenergies E_n^+ for wavefunctions of even parity (+), tunnel splittings ΔE_n and tunneling times t_n.

Doublet (n)	E_n^+ (meV)	ΔE_n (meV)	t_n (ps)
0	0	4.3×10^{-8}	4.8×10^{7}
1	36	6.1×10^{-6}	3.4×10^{5}
2	72	4.4×10^{-4}	4.7×10^{3}
3	105	1.8×10^{-2}	1.2×10^{2}
4	137	0.43	4.8
5	162	4.8	0.43
6	184	13	0.15
7	213	17	0.12
8	249	19	0.11
9	288	21	10×10^{-2}
10	330	22	9.3×10^{-2}
⋮	⋮	⋮	⋮
19	810	30	6.9×10^{-2}

Table E.2: Eigenstate data obtained for the 1 D, cation resonant state potential of COD on Si(100). Given are eigenenergies E_n^+ for wavefunctions of even parity (+), tunnel splittings ΔE_n and tunneling times t_n.

Appendix F

Ohmic bath, 2 D dissipative model

The coupling matrix elements between initial and final system states $\psi_{i/f}(\phi_u, \phi_s)$ in rate Eq. (4.27) of the 2 D, Ohmic bath vibrational relaxation model are calculated as,

$$|\langle\psi_f|\sqrt{I_s}\phi_s + \sqrt{I_u}\phi_u|\psi_i\rangle|^2 \approx I_s\,|\langle\psi_f|\phi_s|\psi_i\rangle|^2 + I_u\,|\langle\psi_f|\phi_u|\psi_i\rangle|^2 \approx I_s\,V_{fi,s}^2 + I_u\,V_{fi,u}^2 \quad , \tag{F.1}$$

neglecting the $2\sqrt{I_s\,I_u}\,V_{fi,s}\,V_{fi,u}$ term. This simplification of Eq. (4.27) introduces only small errors[1], as can be explained by the separable, harmonic limit of $\psi_{i/f}$,

$$\psi_k(\phi_s, \phi_u) \approx \alpha_{k,s}(\phi_s) \cdot \beta_{k,u}(\phi_u) \quad , \tag{F.2}$$

where $\alpha_{k,s}(\phi_s)$ and $\beta_{k,u}(\phi_u)$ are harmonic state functions. In this harmonic, separable limit the coupling matrix element $V_{fi,s/u}$ can be approximated as,

$$V_{fi,s/u} \approx \langle\alpha_{f,s}\cdot\beta_{f,u}|\phi_{s/u}|\alpha_{i,s}\cdot\beta_{i,u}\rangle \approx \sqrt{i_{s/u}}\cdot\sqrt{\frac{\hbar}{2\,I_{s/u}\cdot\omega_{s/u}}}\cdot\delta_{i_{s/u},(f_{s/u}+1)}\cdot\delta_{i_{u/s},f_{u/s}} \quad . \tag{F.3}$$

The matrix elements $V_{fi,s/u}$ can only be non-zero, if $f_{s/u} = i_{s/u} + 1$ and $f_{u/s} = i_{u/s}$. In other words, there can't be a relaxation in both modes ϕ_s and ϕ_u at the same time. Therefore, the approximation in Eq. (F.1) holds for the harmonic, separable limit since,

$$2\sqrt{I_s\,I_u}\,V_{fi,s}\,V_{fi,u} \approx \hbar\cdot\sqrt{i_s\,i_u}\cdot\sqrt{\frac{1}{\omega_s\,\omega_u}}\cdot\delta_{i_s,(f_s+1)}\cdot\delta_{i_u,f_u}\cdot\delta_{i_u,(f_u+1)}\cdot\delta_{i_s,f_s} \approx 0 \quad . \tag{F.4}$$

[1] For the 1000 lowest 2 D vibrational states of the electronic COD ground state potential (see Sec. 4.4.1) the corresponding relaxation rate error is less than $1.5\times10^{-20}\,(\hbar/\mathrm{E}_h)^{-1}$.

Bibliography

[1] K. Zenichowski, T. Klamroth, and P. Saalfrank, Appl. Phys. A **93**, 319 (2008).

[2] C. Nacci, S. Fölsch, K. Zenichowski, J. Dokiĉ, T. Klamroth, and P. Saalfrank, Nano Lett. **9**, 2996 (2009).

[3] K. Zenichowski, J. Dokiĉ, T. Klamroth, and P. Saalfrank, J. Chem. Phys. **136**, 094705 (2012).

[4] K. Zenichowski, T. Klamroth, and P. Saalfrank, J. Phys.: Condens. Matter **24** (2012), accepted.

[5] M. Schulz, Nature **399** (1999).

[6] R. P. Feynman, Engineering and Science (1960).

[7] G. Binnig, H. Rohrer, C. Gerber, and E. Weibel, Appl. Phys. Lett. **40**, 178 (1982).

[8] G. Binnig, C. F. Quate, and C. Gerber, Phys. Rev. Lett. **56**, 930 (1986).

[9] F. Grey, C. Thirstrup, and H. Busch, Large clusters of atoms and molecules, chapter Manipulation of atoms and clusters by STM, pp. 463–473, Kluwer Academic Publishers (1996).

[10] C. Nacci, J. Lagoute, X. Liu, and S. Fölsch, Phys. Rev. B **77**, 121405(R) (2008).

[11] W. A. Hofer, A. F. S., and A. L. Shluger, Rev. Mod. Phys. **75**, 1287 (2003).

[12] J. Tersoff and D. R. Hamann, Phys. Rev. B **31**, 805 (1985).

[13] R. M. Feenstra and J. A. Stroscio, Scanning Tunneling Microscopy, chapter Methods of Tunneling Spectroscopy, Academic, San Diego (1993).

[14] B. A. Janta-Polczynski, J. I. Cerdá, G. Éthier-Majcher, K. Piyakis, and A. Rochefort, J. Appl. Phys. **104**, 023702 (2008).

[15] E. J. Heller, M. F. Crommie, C. P. Lutz, and D. M. Eigler, Nature **369**, 464 (1994).

[16] H. C. Manoharan, C. P. Lutz, and D. M. Eigler, Nature **403**, 512 (2000).

[17] J. L. Pitters and R. A. Wolkow, Nano Letters **6**, 390 (2006).

[18] N. P. Guisinger, M. E. Greene, R. Basu, A. S. Baluch, and M. C. Hersam, Nano Lett. **4**, 55 (2004).

[19] N. P. Guisinger, N. L. Yoder, and M. C. Hersam, Proceedings of the National Academy of Sciences of the United States of America **102**, 8838 (2005).

[20] B. C. Stipe, M. A. Rezaei, and W. Ho, Science **280** (1998).

[21] W. Ho, Acc. Chem. Res. **31**, 567 (1998).

[22] W. Ho, J. Chem. Phys. **117**, 11033 (2002).

[23] H. Gawronski, M. Mehlhorn, and K. Morgenstern, Science **319**, 930 (2008).

[24] B. N. J. Persson, Phys. Scr. **38**, 282 (1988).

[25] B. N. J. Persson and J. Demuth, Solid State Comm. **57**, 769 (1986).

[26] B. N. J. Persson and A. Baratoff, Phys. Rev. Lett. **59**, 339 (1987).

[27] P. Saalfrank, Chem. Rev. **106**, 4116 (2006).

[28] B. C. Stipe, M. A. Rezaei, W. Ho, S. Gao, M. Persson, and B. I. Lundqvist, Phys. Rev. Lett. **78**, 4410 (1997).

[29] T. C. Shen, C. Wang, G. Abeln, J. Tucker, J. Lyding, P. Avouris, and R. Walkup, Science **268**, 1590 (1995).

[30] D. M. Eigler, C. P. Lutz, and W. E. Rudge, Nature **352**, 600 (1991).

[31] B. N. J. Persson and P. Avouris, Surf. Science **390**, 45 (1997).

[32] K. Stokbro, U. Quaade, R. Lin, C. Thirstrup, and F. Grey, Faraday Discuss. **117**, 231 (2000).

[33] S. W. Hla, J. Vac. Sci. Technol. B **23**, 1351 (2005).

[34] P. Avouris, Acc. Chem. Res. **28**, 95 (1995).

[35] D. M. Eigler and E. K. Schweizer, Nature **344**, 524 (1990).

[36] I. Lyo and P. Avouris, Science **253**, 173 (1991).

[37] L. Bartels, G. Meyer, and K. H. Rieder, Phys. Rev. Lett. **79**, 697 (1997).

[38] G. Dujardin, A. Mayne, O. Robert, F. Rose, C. Joachim, and H. Tang, Phys. Rev. Lett. **80**, 3085 (1998).

[39] T. Komeda, Y. Kim, M. Kawai, B. N. J. Persson, and H. Ueba, Science **295**, 2055 (2002).

[40] A. J. Heinrich, J. A. Gupta, C. P. Lutz, and D. M. Eigler, Science **306**, 466 (2004).

[41] H. J. Lee and W. Ho, Science **286**, 1719 (1999).

[42] J. I. Pascual, N. Lorente, Z. Song, H. Conrad, and H. P. Rust, Nature **423**, 525 (2003).

[43] S. Katano, Y. Kim, M. Hori, M. Trenary, and M. Kawai1, Science **316**, 1883 (2007).

[44] M. T. Cuberes, R. R. Schlittler, and J. K. Gimzewski, Appl. Phys. Lett. **69**, 3016 (1996).

[45] V. Iancu and S. W. Hla, PNAS **103**, 13718 (2006).

[46] T. Kumagai, M. Kaizu, H. Okuyama, S. Hatta, T. Aruga, I. Hamada, and Y. Morikawa, Phys. Rev. B **79**, 035423 (2009).

[47] M. Martin, M. Lastapis, D. Riedel, G. Dujardin, M. Mamatkulov, L. Stauffer, and P. Sonnet, Physical Review Letters **97**, 216103 (2006).

[48] J. A. Stroscio and R. J. Celotta, Science **306**, 242 (2004).

[49] B. S. Swartzentruber, A. P. Smith, and H. Jónsson, Phys. Rev. Lett. **77**, 2518 (1996).

[50] N. Henningsen, R. Rurali, K. J. Franke, I. F. Torrente, and J. Pascual, Appl. Phys. A **93**, 241 (2008).

[51] J. W. Lyding, T. C. Shen, J. S. Hubacek, J. R. Tucker, and G. C. Abeln, Appl. Phys. Lett. **64**, 2010 (1994).

[52] V. Balzani, A. Credi, and M. Venturi, ChemPhysChem **9**, 202 (2008).

[53] J. M. Tour, ed., Molecular Electronics, World Scientific, Singapore (2003), and references therein.

[54] A. Jalabert, A. Amara, and F. Clermidy, eds., Molecular Electronics: Materials, Devices and Applications, Springer Science+Business Media B.V. (2008).

[55] M. F. Crommie, C. P. Lutz, and D. M. Eigler, Science **262**, 218 (1993).

[56] G. M. Clayton and S. Devasia, Nanotechnology **16**, 809 (2005).

[57] F. Moresco and A. Gourdon, PNAS **102**, 8809 (2005).

[58] H. J. Mamin and D. Rugar, Appl. Phys. Lett. **61**, 1003 (1992).

[59] A. Pantazi, IBM J. RES. & DEV. **52** (2008).

[60] Y. M. Lin, J. C. Tsang, M. Freitag, and P. Avouris, Nanotechnology **18**, 295202 (2007).

[61] D. J. Chadi, Phys. Rev. Lett. **59**, 1691 (1987).

[62] R. J. Hamers, P. Avouris, and F. Bozso, Phys. Rev. Lett. **59**, 2071 (1987).

[63] R. M. Tromp, R. J. Hamers, and J. E. Demuth, Phys. Rev. Lett. **55**, 1303 (1985).

[64] C. Hobbs and L. Kantorovich, Nanotechnology **15**, S1 (2004).

[65] T. Tabata, T. Aruga, and Y. Murata, Surf. Science **179**, L64 (1987).

[66] R. J. Hamers, R. M. Tromp, and J. E. Demuth, Phys. Rev. B **34**, 5343 (1986).

[67] J. Yoshinobu, Prog. Surf. Sci. **77**, 37 (2004).

[68] M. Weinelt, M. Kutschera, T. Fauster, and M. Rohlfing, Phys. Rev. Lett. **92**, 126801 (2004), el. Zustaende der Si(100) Oberflaeche.

[69] M. Kutschera, Elektronendynamik auf Halbleiteroberflächen und in dünnen Metallfilmen, Ph.D. thesis, Erlangen-Nürnberg, Univ. (2001).

[70] R. E. Walkup, D. M. Newns, and P. Avouris, Phys. Rev. B **48**, 1858 (1993).

[71] R. E. Walkup, D. M. Newns, and P. Avouris, J. Electron. Spectros. Relat. Phenom. **64/65**, 523 (1993).

[72] S. Gao, P. M., and B. I. Lundqvist, Solid State Commun. **84**, 271 (1992).

[73] G. Boendgen and P. Saalfrank, J. Phys. Chem. B **102**, 8029 (1998).

[74] J. W. Gadzuk and C. W. Clark, J. Chem. Phys. **91**, 3174 (1989).

[75] J. W. Gadzuk, Surf. Science **342**, 345 (1995).

[76] P. Avouris, R. E. Walkup, A. R. Rossi, H. C. Akpati, P. Nordlander, T. C. Shen, G. C. Abeln, and J. W. Lyding, Surf. Science **363**, 368 (1996).

[77] P. Avouris, R. E. Walkup, A. R. Rossi, T. C. Shen, G. C. Abeln, J. R. Tucker, and J. W. Lyding, Chem. Phys. Lett. **257**, 148 (1996).

[78] V. May and O. Kühn, Charge and Energy Transfer Dynamics in Molecular Systems, WILEY-VCH Verlag GmbH, Weinheim (2004).

[79] A. Abe, K. Yamashita, and P. Saalfrank, Phys. Rev. B **67**, 235411 (2003).

[80] G. Lindblad, Commun. Math. Phys. **48**, 119 (1976).

[81] S. Sakong, P. Kratzer, X. Han, K. Laß, O. Weingart, and E. Hasselbrink, J. Chem. Phys. **129**, 174702 (2008).

[82] P. Guyot-Sionnest, P. Dumas, Y. J. Chabal, and G. S. Higashi, Phys. Rev. Lett. **64**, 2156 (1990).

[83] I. Andrianov and P. Saalfrank, J. Chem. Phys. **124**, 034710 (2006).

[84] H. M. Tütūncū, S. J. Jenkins, and G. P. Srivastava, Surf. Sci. **402-404**, 42 (1998).

[85] P. Guyot-Sionnest, L. P., and E. Miller, J. Chem. Phys. **102**, 4269 (1995).

[86] K. Laß, X. Han, and E. Hasselbrink, J. Chem. Phys. **123**, 051102 (2005).

[87] H. D. Meyer, U. Manthe, and L. S. Cederbaum, Chem. Phys. Lett. **165**, 73 (1990).

[88] I. Andrianov and P. Saalfrank, Chem. Phys. Lett. **433**, 91 (2006).

[89] R. B. Gerber, V. Buch, and M. A. Ratner, J. Chem. Phys. **77**, 3022 (1982).

[90] G. K. Paramonv, I. Andrianov, and P. Saalfrank, J. Phys. Chem. C **111**, 5432 (2007).

[91] J. Reinhold, Quantentheorie der Moleküle, Teubner Verlag (2006).

[92] C. C. Marston and G. G. Balint-Kurti, J. Chem. Phys. **91**, 3571 (1989).

[93] V. Kokoouline, O. Dulieu, R. Kosloff, and F. Masnou-Seeuws, J. Chem. Phys. **110**, 9865 (1999).

[94] P. Saalfrank, Open-System Density Matrix Theory: Numerics & Chemical Applications (2008), lecture notes.

[95] G. K. Paramonov and P. Saalfrank, J. of Chem. Phys. **110**, 6500 (1999).

[96] B. Jackson, J. Chem. Phys. **108**, 1131 (1998).

[97] K. Finger and P. Saalfrank, Chem. Phys. Lett. **268**, 291 (1997).

[98] K. Blum, Density Matrix Theory and Applications, Plenum Press, New York (1996).

[99] D. Kohen, C. C. Marston, and D. J. Tannor, J. Chem. Phys. **107**, 5236 (1997).

[100] R. Alicki and K. Lendi, eds., Quantum Dynamical Semigroups and Applications, Springer (1987).

[101] M. Nest and H. D. Meyer, J. Chem. Phys. **119**, 24 (2003).

[102] U. Weiss, Quantum Dissipative Systems, World Scientific (1992).

[103] H. Ueba, T. Mii, N. Lorente, and B. N. J. Persson, J. Chem. Phys. **123**, 084707 (2005), inelastic electron tunneling fraction.

[104] P. Saalfrank, Chem. Phys. **211**, 265 (1996).

[105] K. Mølmer, Y. Castin, and J. Dalibard, J. Opt. Soc. Am. B **10**, 524 (1993).

[106] W. Koch and M. C. Holthausen, A Chemist's Guide to Density Functional Theory, Wiley-VCH, 2nd edition (2001).

[107] C. Cramer, Essentials of Computational Chemistry, Wiley (2002).

[108] A. Becke, J. Chem. Phys. **98**, 5648 (1993).

[109] C. Lee, W. Yang, and R. G. Parr, Physical Review B **37**, 785 (1988).

[110] R. Ditchfield, W. J. Hehre, and J. A. Pople, J. Chem. Phys. **54**, 724 (1971).

[111] K. Burke, J. P. Perdew, and Y. Wang, Electronic Density Functional Theory: Recent Progress and New Directions, Plenum Press (1998).

[112] M. J. e. a. Frisch, Gaussian, Inc., Wallingford, CT, 2004.

[113] T. Koopmans, Physica **1**, 105 (1933).

[114] A. Szabo and N. S. Ostlund, Modern Quantum Chemistry: Introduction to Advanced Electronic Structure Theory, Dover Publications, Inc. (1889).

[115] A. Z. Szarka, L. A. Curtiss, and J. R. Miller, Chem. Phys. **246**, 147 (1999).

[116] J. P. Perdew and M. Levy, Phys. Rev. B **56**, 16021 (1997).

[117] C. G. Zhan, J. A. Nichols, and D. A. Dixon, Journal of Physical Chemistry A **107**, 4184 (2003).

[118] L. D. Betowski, M. Enlow, L. Riddick, and D. H. Aue, J. Phys. Chem. A **110**, 12927 (2006).

[119] K. Stokbro, C. Thirstrup, M. Sakurai, U. Quaade, B. Yu-Kuang Hu, F. Perez-Murano, and F. Grey, Phys. Rev. Lett. **80**, 2618 (1998).

[120] Z. Liu, L. C. Feldman, N. H. Tolk, and P. I. Zhang, Z. Cohen, Science **312**, 1024 (2006).

[121] U. J. Quaade, K. Stokbro, and F. Grey, Nanotechnology **12**, 265 (2001).

[122] U. J. Quaade, K. Stokbro, C. Thirstrup, and F. Grey, Surf. Sci. **415**, L1037 (1998).

[123] U. Höfer, L. Leping, and T. F. Heinz, Phys. Rev. B **45**, 9485 (1992).

[124] O. V. Gritsenko and E. J. Baerends, J. Chem. Phys. **117**, 9154 (2002).

[125] C. Thirstrup, M. Sakurai, T. Nakayama, and K. Stokbro, Surf. Science **424**, L329 (1999).

[126] M. McEllistream, M. Allgeier, and J. J. Boland, Science **279**, 545 (1998).

[127] P. Hänggi, P. Talkner, and M. Borkovec, Rev. Mod. Phys. **62**, 251 (1990).

[128] L. J. Whitman, J. A. Stroscio, R. A. Dragoset, and R. J. Celota, Science **251**, 1206 (1991).

[129] B. N. J. Persson and P. Avouris, Chem. Phys. Lett. **242**, 483 (1995).

[130] J. M. Buriak, Chemical Reviews **102**, 1271 (2002).

[131] R. Wolkow, Annu. Rev. Phys. Chem. **50**, 413 (1999).

[132] M. Lastapis, M. Martin, D. Riedel, L. Hellner, G. Comtet, and G. Dujardin, Science **308**, 1000 (2005).

[133] D. Riedel, M. Cranney, M. Martin, R. Guillory, G. Dujardin, M. Dubois, and P. Sonnet, J. Am. Chem. Soc. **131**, 5414 (2009).

[134] S. N. Patitsas, G. P. Lopinski, O. Hul'ko, D. J. Moffatt, and R. A. Wolkow, Surf. Science **457**, L425 (2000).

[135] S. Alavi, R. Rousseau, and T. Seideman, J. Chem. Phys. **113**, 4412 (2000).

[136] S. Alavi, R. Rousseau, G. P. Lopinski, R. A. Wolkow, and T. Seideman, Faraday Discuss. **117**, 213 (2000).

[137] J. S. Hovis, H. Liu, and R. J. Hamers, Surf. Sci. **402**, 1 (1998).

[138] Y. Yamashita, K. Hamaguchi, S. Machida, K. Mukai, J. Yoshinobu, S. Tanaka, and M. Kamada, Appl. Surf. Sci. **169**, 172 (2001).

[139] R. B. Woodward and R. Hoffmann, JACS **87**, 395 (1965).

[140] R. J. Hamers, S. K. Coulter, M. D. Ellison, J. S. Hovis, D. F. Padowitz, M. P. Schwartz, C. M. Greenlief, and J. N. Russell, Acc. Chem. Res. **33**, 617 (2000).

[141] J. S. Hovis and R. J. Hamers, Journal of Physical Chemistry B **101**, 9581 (1997).

[142] F. Jolly, F. Bournel, F. Rochet, G. Dufour, F. Sirotti, and A. Taleb, Phys. Rev. B **60**, 2930 (1999).

[143] J. Dokiˇc, Quantum Mechanical Study of Molecular Switches: Electronic Structure, Kinetics and Dynamical Aspects, Ph.D. thesis, University of Potsdam (2009).

[144] J.-H. Cho, D.-H. Oh, and L. Kleinman, Phys. Rev. B **64**, 241306(R) (2001).

[145] C. Nacci, J. Lagoute, X. Liu, and S. Fölsch, Appl. Phys. A **93**, 313 (2008).

[146] Numerical Recipes: The Art of Scientific Computing, Cambridge University Press (2007).

[147] U. Höfer, Appl. Phys. A **63**, 533 (1996).

[148] J. Kua, L. J. Lauhon, W. Ho, and W. A. Goddard III, J. Chem. Phys. **115**, 5620 (2001).

[149] F. Ronci, S. Colonna, and A. Cricenti, Phys. Rev. Lett. **99** (2007).

[150] T. R. Mattsson and G. Wahnström, Phys. Rev. B **56**, 14944 (1997).

[151] C. Nacci, S. Fölsch, K. Zenichowski, J. Dokić, T. Klamroth, and P. Saalfrank, Nano Lett. **9**, 2996 (2009).

[152] D. M. Eigler, P. S. Weiss, and E. K. Schweizer, Phys. Rev. Lett. **66**, 1189 (1991).

[153] E. Hairer, S. P. Norsett, and G. Wanner, Solving Ordinary Differential Equations. I: Nonstiff Problems., Springer-Verlag (1987).

Danksagung

Diese Doktorarbeit entstand aus meiner Begeisterung für die Welt der Quantenchemie und der durch sie weitergehenden Beschreibung chemischer Prozesse sowie einem Wunsch dem "Innersten" des Ganzen, als Station einer Lebensreise, etwas näher zu kommen.

Dabei waren die sehr gut strukturierten und Freude am Verstehen bereitenden Vorlesungen meines Doktorvaters, Prof. Peter Saalfrank, ganz wesentlich für die Entscheidung mich in Diplom- und Doktorarbeit weiter mit dem Themengebiet zu befassen. Während dieser Zeit wurde ich geduldig und konzentriert durch meinen Doktorvater sowie durch PD Dr. Tillmann Klamroth und PD Dr. Mathias Nest an die Quantendynamik herangeführt und sehr gut betreut. Insgesamt haben mein Doktorvater und Herrn PD Dr. Klamroth die Arbeit durch ihre kritische Begleitung in fachlichen Fragen wesentlich voran gebracht.

Für eine kollegiale und angenehme Arbeitsatmosphäre möchte ich neben allen anderen Mitgliedern der Arbeitsgruppe insbesondere Frau Dr. Jadranka Dokič und Dr. Jean Christophe Tremblay danken.

Sicher wäre die Arbeit noch nicht vollbracht, wenn meine Frau mir, in Bezug auf unsere Kinder, nicht stetig, neben der "normalen" universitären Arbeitszeit, weitere Fenster für die Beendigung der These frei gehalten hätte. Ähnliches gilt auch für Dr. Toralf Beitz und Prof. Martin Roth, welche weitere Arbeiten während meiner anschließenden Tätigkeiten ermöglichten.

Durch das abenteuerliche Unterfangen die These in Englisch zu verfassen hat mich unter anderen Herr Mahmud Lund mittels Korrektur lesens des Manuskripts begleitet.

Zum Abschluss danke ich an erster Stelle meinen Eltern, meiner Frau und allen anderen, die mich stetig an die Abgabe der Arbeit erinnerten, wo ich es doch viel interessanter finde immer wieder etwas Neues zu beginnen.

Erklärung

Hiermit versichere ich, dass ich die vorliegende Arbeit mit den angegebenen Hilfsmitteln selbständig angefertigt habe.

Potsdam, im Mai 2012